Design of Chitosan-Based Carriers for Biomedical Engineering Applications

UGUR BOZUYUK

KOC UNIVERSITY

SEPTEMBER 2018

Design of Chitosan-Based Carriers for Biomedical Engineering Applications

by

UGUR BOZUYUK

A Thesis Submitted to the Graduate School of Science and Engineering in Partial Fullfilment of the Requirements for the Degree of Master of Science in Chemical & Biological Engineering

Koc University

Koc University

Graduate School of Science and Engineering

This is to certify that I have examined this copy of a master's thesis by

Ugur Bozuyuk

and have found that it is complete and satisfactory
in all respects, and that any and all revisions required
by the final examining committee have been made.

Committee Members:

_____

Assoc. Prof. Dr. Seda Kizilel

_____

Dr. Erkan Senses

_____

Prof. Dr. Kutlu Ulgen

Date: _____

ABSTRACT

Chitosan-based materials have gained enourmous attention due to unique properties of chitosan such as biodegrability, biocompatibility and cationic nature. Especially, chitosan-based drug/gene delivery systems became a promising alternative for the treatment of various diseases. This thesis includes studies about nanoparticle and microrobotic-based chitosan carriers. In the first part of the thesis, the main aim is to synthesize colloidally stable ionically crosslinked chitosan nanoparticles. Ionically-crosslinked chitosan nanoparticles have gained considerable attention due to their cationic nature and sub-100 nm size. However, low solubility of chitosan in neutral media restricts its potential clinical translation. PEGylation is a simple solution to increase solubility of chitosan and chitosan nanoparticles in neutral media. Yet, effect of PEG chain length and chitosan/PEG ratio on particle size and zeta potential of nanoparticles are not known. This chapter of the thesis presents a systematic analysis of the effect of PEG chain length and chitosan/PEG ratio on size and zeta potential of nanoparticles. PEGylated chitosan polymers were prepared before the nanoparticle synthesis with different PEG chain lengths and chitosan/PEG ratios. Effect of PEG chain length (2, 5 and 10 kDa), chitosan/PEG ratio (25 mg chitosan to 4, 12 and 20 μmoles of PEG) and pH (within 6.0-7.4) on nanoparticles were investigated. Having obtained the experimental size and zeta potential values, artficial neural networks were created to predict size and zeta potential values of different groups. Artificial neural networks is a modelling tool used in nanomedicine to optimize and predict inherent properties of the system. Inherent properties of a nanoparticle system such as size and zeta potential can be estimated based on previous experiment results. Namely, nanoparticles with desired properties can be synthesized using an ANN. We were able to estimate the size and zeta potential of nanoparticles under different experimental conditions. After that, we performed cell attachment experiments with different nanoparticle groups. Nanoparticle groups having higher zeta potentials had better adhesion ability to HEK293-T cells, which was estimated through ANN model prior to experiments. Overall, this chapter presents the PEGylation of chitosan, synthesis of PEGylated chitosan nanoparticles and the use of ANN model as a tool to predict important properties such as size and zeta potential. In the second part of

the thesis, plasmid DNA loaded and tumor homing peptide (CREKA) modified stable chitosan nanoparticle carriers were synthesized for gene delivery applications. Peptide modification and DNA loading was confirmed with certain assays and these nanoparticles will be used for cancer therapy applications in the future. In the third part of the thesis, we propose a magnetically-actuated chitosan-based microrobotic system that can release the chemotherapeutic drug using external light stimulus. We fabricated the chitosan-based microswimmers by two-photon direct laser writing (TDLW) technique using of a photosensitive derivative of chitosan in the form of a magnetic polymer nanocomposite. Amino groups on the microswimmers were modified with doxorubicin using a photocleavable linker. Controlled moving ability of the microswimmers was shown under rotating magnetic field. 60% of doxorubicin was released from the microswimmers in 5 minutes with light stimulus at 365 nm wavelength and 30 mW laser output power. Enzymatic degradation of the microswimmers was shown in 204 hours. This part of the thesis presents the combination of light-triggered drug delivery with magnetically-powered microswimmer mobility. Overall, it was shown that chitosan-based carriers can be fabricated in various forms for different applications. Our results suggested that chitosan-based materials are promising for biomedical applications.

ÖZET

Kitosan bazlı malzemeler, kitosanın biyoçözünürlük, biyouyumluluk ve katyonik yapısından dolayı büyük bir ilgi kazanmıştır. Özellikle, kitosan bazlı ilaç/gen salım sistemleri çeşitli hastalıkların tedavisi için umut verici bir alternatif haline gelmiştir. Bu yüksek lisans tezi kitosan bazlı nanoparçacık ve mikrorobotik ilaç taşıyıcıları hakkında çalışmalar içermektedir. Bu tezin ilk kısmındaki amaç, iyonik olarak çarpraz bağlanmış stabil kitosan nanoparçacıkları sentezlemektir. İyonik olarak çarpraz bağlanmış kitosan nanoparçacıkları katyonik yapıları ve 100 nanometre altında sentezlenebilmeleri sebebi ile özellikle nanotıp alanında büyük potansiyele sahiptir. Fakat, kitosanın nötral ortamdaki düşük çözünürlüğü kitosan nanoparçacıkların klinik aşamaya geçememesindeki en büyük engeldir. Kitosanın polietilen glikol (PEG) ile kimyasal modifikasyonu, kitosanın nötr ortamdaki çözünürlüğünü arttırmak için bilinen bir yöntemdir, fakat PEG zincir uzunluğu ve kitosan/PEG oranının kitosan nanoparçacıklarının boyut ve zeta potansiyelleri üzerindeki etkileri bilinmemektedir. Bu bölüm, PEG zincir uzunluğu ve kitosan/PEG oranının nanopartiküllerin boyut ve zeta potansiyeline etkisinin sistematik bir analizini sunmaktadır. PEGlenmiş kitosan polimerleri nanoparçacık sentezinden önce farklı PEG zincir uzunlukları ve kitosan/PEG oranlarında hazırlanmıştır. PEG zincir uzunluğu (2, 5 ve 10 kDa), kitosan/PEG oranı (25 mg kitosan başına 4, 12 ve 20 µmol) ve pH (6.0-7.4) parametrelerinin kitosan nanoparçacıkları üzerine etkileri araştırılmıştır. Deneysel parçacık boyutu ve zeta potansiyeli verileri elde edikten sonra, başka parçacık gruplarının boyut ve zeta potansiyellerini tahmin edebilmek amacıyla yapay sinir ağları kurulmuştur. Yapay sinir ağları, nanotıpta sistemin içsel özelliklerini varolan deney sonuçlarına göre tahmin edebilmeye yarayan bir modelleme yöntemidir. Örneğin, nanoparçacıkların, boyut ve zeta potansiyelleri geçmiş deneysel gözlemlere dayanarak farklı gruplar için tahmin edilebilir. Bu çalışmada yapay sinir ağı modelini kullanılarak deneyi yapılmamış nanoparçacıkların boyut ve zeta potansiyelleri tahmin edilmiştir. Zeta potansiyelleri yüksek nanoparçacıklar HEK293-T hücre hattıyla daha fazla etkileşime geçmiştir ve bu etkileşim yapay sinir ağı modeliyle önceden tahmin edilmiştir. Genel olarak, bu bölüm kitosanın PEG ile reaksiyonunu, PEGlenmiş kitosan nanopartiküllerin sentezini kapsamlı bir şekilde

sunmaktadır. Ek olarak yapay sinir ağı modeli ile tasarlanmış nanoparçacıkların elde edilebileceğini ve hücre ile etkileşimlerinin bu model ile tahmin edilebileceği gösterilmiştir. Tezin ikinci bölümünde plazmid DNA yüklü ve tümöre seçici peptit ile modifiye edilmiş kitosan nanoparçacıkları sentezlenmiştir. Peptit modifikasyonu ve DNA yüklenmesi birtakım tahliller ile onaylanmıştır. Bu parçacıklar gelecekte gen aktarım ve kanser terapisi alanlarında kullanılacaklardır. Tezin üçüncü kısmında ise, magnetik uyarımla harekete geçebilen ve ışık ile uyarımlı bir şekilde kemoterapi ilacı salımı yapabilen kitosan bazlı bir mikrorobotik sistemi geliştirilmiştir. Mikrorobotlar kitosan kullanılarak iki-foton lazer yazım tekniği ile magnetik polimer nanokompoziti şeklinde üretilmiştir. Mikroyüzücülerin üzerinde bulunan amino grupları, ışık ile kırılabilen bir molekül aracılığıyla doksorubisin ile modifiye edilmiştir. Mikrorobotların kontrollü hareket kabiliyeti döner manyetik alan altında gösterilmiştir. 365 nm dalgaboyunda, ışık tetiklemesi ile doksorubisinin %65'i 5 dakika içerisinde salınmıştır. Ek olarak, kitosan mikroyüzücülerin enzimatik çözünürlüğü 204 saat içerisinde gösterilmiştir. Tezin bu bölümü ışıkla tetiklemeli ilaç salımı ve manyetik mikrorobotik hareket kabiliyetinin bir kombinasyonunu sunmaktadır. Genel olarak bu tezde, kitosan bazlı malzemelerin çeşitli formlarda üretilebildiği gösterilmiştir. Elde ettiğimiz sonuçlar, kitosan bazlı bu malzemelerin çeşitli biyomedikal uygulamalar için umut verici olduğunu göstermiştir.

ACKNOWLEDGEMENTS

I would like to express my sincere gratitude to my advisor Prof. Seda Kizilel for her patience, motivation, and immense knowledge. I always felt her scientific and psychological support during my MSc and always knew that she would do the best thing for me. She always attached importance to my ideas and I became an independent researcher thanks to her. This was really important for me, because I believe that I gained huge confidence thanks to her approach. Besides her scientific side, I will take her ambition and work discipline as example in my life. Being a master student of her was the best choice in my life, and this played important role on my career decision. I hope I will be a researcher like you in the future.

I would like to acknowledge Prof. Metin Sitti for allowing me to access his laboratories and his sincere advices about our project. I also would like to thank to Nihal Olcay Dogan, Oncay Yasa, Hakan Ceylan and Ceren Yasa for their help to my studies.

Special thanks to Dr. Erkan Senses and Prof. Dr. Kutlu Ulgen for serving as my committee members and evaluation of my thesis.

I also would like to thank Birgul Akolpoglu for her support. She has always been with me whenever I need. I really appreciate everything what you have done for me. I know we will have a good future together.

To my wonderful family, my mother and father I will be grateful forever for your love. I can’t thank you enough for your endless support and your love.

This thesis is dedicated to my uncle who will be with me forever. You would be proud of me.

TABLE OF CONTENTS

ABSTRACT ..... **IV**

CHAPTER 1: INTRODUCTION **1**

CHAPTER 2: LITERATURE REVIEW **3**

2.1. CHITOSAN 3
2.1.1. Applications of Chitosan 4
2.1.1.1. Tissue Engineering 4
2.1.1.2. Water Treatment 4
2.1.1.3. Drug Delivery Systems 5
2.1.2. Biocompatibility of Chitosan Carriers 7
2.2. NANOPARTICLE-BASED DRUG DELIVERY 8
2.3. MICROROBOTIC DRUG DELIVERY 10

CHAPTER 3: PEGYLATION OF CHITOSAN NANOPARTICLES: AN ARTIFICIAL NEURAL NETWORK STUDY **12**

3.1. INTRODUCTION 12
3.2. EXPERIMENTAL 14
3.2.1. Materials 14
3.2.2. Preparation of PEGylated Chitosan 14
3.2.3. Synthesis of PEGylated Chitosan Nanoparticles 15
3.2.4. Characterization of CS-PEG NPs 15
3.2.5. ANN Study 16
3.2.6. Cell Culture, Cell Attachment and Cell Staining Experiments 16
3.2.7. Statistical Analysis 17
3.3. RESULTS AND DISCUSSION 17
3.3.1. Synthesis of PEGylated Chitosan 18
3.3.2. Synthesis of PEGylated Chitosan Nanoparticles 21
3.3.3. ANN Model 29
3.3.4. Cell Attachment Experiments 32
3.4. CONCLUSIONS 34

CHAPTER 4: SYNTHESIS OF PEGYLATED CHITOSAN NANOPARTICLES AS A GENE DELIVERY VEHICLE **35**

4.1. INTRODUCTION 35
4.2. EXPERIMENTAL 36
4.2.1. Materials 36
4.2.2. Synthesis of Chitosan-PEG-CREKA Conjugate 36
4.2.2.1. TNBS and Ellman's Assay 36
4.2.2.2. Peptide Quantification with Pierce™ BCA Protein Assay Kit 37
4.2.2.3. FT-IR Analysis 37
4.2.3. Synthesis of DNA loaded CREKA Modified Chitosan Nanoparticles 37
4.2.3.1. Encapsulation Efficiency 38
4.3. RESULTS AND DISCUSSION 38
4.3.1. Synthesis of Chitosan-PEG-CREKA Conjugate 38

4.3.1.1. TNBS and Ellman's Assay 39
4.3.1.2. Peptide Quantification with Pierce™ BCA Protein Assay Kit....39
4.3.1.3. FT-IR Analysis....40
4.3.2. Synthesis of CREKA Modified Chitosan Nanoparticles....41
4.4. CONCLUSIONS AND FUTURE WORK....43

CHAPTER 5: LIGHT-TRIGGERED DRUG RELEASE FROM 3D-PRINTED MAGNETIC CHITOSAN MICROSWIMMERS 44

5.1. INTRODUCTION....44
5.2. EXPERIMENTAL 45
5.2.1. Materials 45
5.2.2. Synthesis of Methacrylamide Chitosan 45
5.2.3. Degree of Methacrylation Characterization....46
5.2.4. 3D Printing of the Microswimmers 46
5.2.5. Enzymatic Degradation of Microswimmers 47
5.2.6. Photocleavable Linker and Drug Binding on Microswimmers 47
5.2.7. Light-Triggered Drug Release from the Microswimmers 47
5.3. RESULTS AND DISCUSSION 48
5.3.1. Synthesis of Methacrylamide Chitosan 48
5.3.2. 3D Printing of the Microswimmers 49
5.3.3. Magnetic Actuation and Control of the Microswimmers 50
5.3.4. Enzymatic Degradation of Microswimmers 52
5.3.5. Photocleavable Linker and Drug Binding to the Microswimmers 54
5.3.6. Light-Triggered Drug Release from the Microswimmers 56
5.4. CONCLUSIONS....59

CHAPTER 6: CONCLUSIONS AND FUTURE WORK 60

BIBLIOGRAPHY 61

APPENDIX A - RAW DYNAMIC LIGHT SCATTERING DATA....A-1
APPENDIX B - MATLAB CODE USED FOR ANN B-1
APPENDIX C – ARTIFICIAL NEURAL NETWORK OPTIMIZATION C-1

LIST OF FIGURES

Figure 2.1. Production of chitosan 3

Figure 2.2. Synthesis of PEGylated chitosan nanoparticles.....7

Figure 2.3. Schematic representation of EPR effect, nanoparticles do not accumulate in healthy tissues. They accumulate more in tumor tissues unlike small therapeutic molecules. 9

Figure 3.1. Key steps of the study.....18

Figure 3.2. Demonstration of hindrance effects due to longer PEG chains. Longer PEG chains hinder available amino group containing chitosan monomers which results in lower conjugation efficiency. 20

Figure 3.3. FTIR spectra of chitosan, mPEG-SVA and PEGylated chitosan (5 kDa – 20 μmole group).....21

Figure 3.4. Three-dimensional surface plots of size and zeta potential of nanoparticles with respect to different independent variables. Plots were sketched using Table 2 and Table 3. A) Size and zeta potentials of nanoparticles for different PEG chain lengths. B) Zeta potentials of different PEGylated nanoparticles at different pH values. Note: $p<0.005$ for size and zeta potential values separately. 24

Figure 3.5. Schematic presentation of hindrance effects. Higher PEG chains mask a greater number of protonated amino groups on the surface of nanoparticles. 25

Figure 3.6. FE-SEM images of 5 kDa PEG – 20 μmole nanoparticles.....26

Figure 3.7. FE-SEM image of 10 kDa PEG – 20 μmole nanoparticles 27

Figure 3.8. STEM images of a 2 kDa PEG – 20 μmole nanoparticles 28

Figure 3.9. Optimization of ANNs. MSE and R^2 values of test data for the different backpropagation methods. A) ANN optimization for size. L. M. with 1 layer was selected. B) ANN optimization for zeta potential, G. D. L. R. with 4 layers was selected. 29

Figure 3.10. Cell attachment experiments in different pH values. Glass surfaces were coated with nanoparticles from 2 kDa - 12 μmole group. A) FDA staining of living cells. There are a greater number of cells on coated surfaces in pH 6.5. B) Quantification of number of attached cells on glass slides. pH 6.5 group has much greater number of cells compared to pH 7.4. For both groups, uncoated slides have a smaller number of cells..32

Figure 3.11. Cell attachment experiments with 2, 5 &10 kDa – 12 μmole groups in pH 6.5. A) FDA staining of attached cells. 2 kDa group has the highest number of attached

cells according to its zeta potential. B) Quantification of number of attached cells. C) Zeta potential versus number of attached cells. Effect of negative control was subtracted from each group. Number of attached cells was estimated from the fitted line 33

Figure 4.1. Synthesis of chitosan-PEG-CREKA conjugate 38

Figure 4.2. Calibration curve for Ellman's assay.....39

Figure 4.3. BCA standard calibration curve 40

Figure 4.4. FT-IR spectrum of chitosan-PEG-CREKA 40

Figure 4.5. Size distribution of DNA loaded CS-PEG-CREKA NPs 41

Figure 4.6. Zeta potential of DNA loaded CS-PEG-CREKA NPs 42

Figure 4.7. Size distribution of PEGylated chitosan nanoparticles.....42

Figure 4.8. Zeta potential of DNA loaded PEGylated chitosan nanoparticles.....43

Figure 5.1. TNBS assay results. Unmodified chitosan gives the highest amino group absorbance at 345 nm. Amino groups absorbance decreases since amino groups are consumed after reaction 48

Figure 5.2. Overview of the synthesis and fabrication processes. A) Synthesis of the photocrosslinkable methacrylamide chitosan from natural chitosan. B) 3D printing of the microswimmers using two-photon direct laser writing technique. C) Optical microscopy image of 3D printed 3x3 array of the microswimmers. D) Energy-dispersive x-ray spectroscopy elemental mapping shows the presence of iron atoms (red color) in the microswimmers. 49

Figure 5.3. Actuation and steering of the microswimmers using a rotating magnetic field. A) Forward velocity of the microswimmers as a function of magnetic excitation frequency demonstrates a step-out frequency of 4.5 Hz. B) Controlled swimming trajectory snapshots (red lines) of the microswimmers under a 10 mT rotating magnetic field at 4.5 Hz. 51

Figure 5.4. Controlled swimming trajectory of the microswimmers at 5 Hz under a 10 mT rotating magnetic field. 51

Figure 5.5. Enzymatic degradation of the microswimmers using lysozyme. A) Optical microscopy images of the microswimmers treated with 15 μg·mL-1 lysozyme, i. t = 0 h and ii. t = 204 h reveal a surface corrosion-based degradation mechanism. B) Changes in length of the microswimmers in time with different lysozyme concentrations. C) Changes in diameter of the microswimmers in time with different lysozyme concentrations. 53

Figure 5.6. Drug binding on microswimmers. A) Schematic shows the reaction pathway to obtain DOX-modified microswimmers. Amino groups on the microswimmers react with NHS group of *o*-nitrobenzyl photocleavable linker molecules. Then, azide-modified DOX reacts with alkyne ends of the microswimmers. B) Microswimmers without the o-nitrobenzyl linker modification were directly treated with the drug molecules (azide-DOX). C) Microswimmers with the *o*-nitrobenzyl linker modification were treated with the drug molecules (azide-DOX). Images were captured with the same fluorescence intensity and exposure time and represent the controlled integration of azide-DOX onto the microswimmers. 55

Figure 5.7. Photobleaching tests for the drug molecules prior to controlled release experiments. A) 470 nm wavelength light excitation for 30 min to negative group (microswimmers without the *o*-nitrobenzyl linker modification) B) 3 mW 365 nm wavelength light exposure for 30 min to negative group. C) 30 mW 365 nm wavelength light exposure for 30 min to negative group**.** 56

Figure 5.8. Light-triggered drug release from the microswimmers. A) DOX release from the microswimmers exposed to 30 mW light intensity for 30 min. Decrease in the fluorescence intensity indicates the cleavage of DOX from the microswimmers and its release. B) Cumulative DOX release from the microswimmers for 3 mW and 30 mW light intensity. C) Smart dosing of DOX from the microswimmers. 365 nm wavelength light is on in the red regions. Roughly, 15% of DOX was released per minute from the microswimmers. 58

Figure 5.9. Controlled and localized drug release from chitosan-based microswimmers. A) UV exposure was focused onto the microswimmers found in left column. Drug molecules were controlled released upon UV exposure while the other group, found in right column, still had the integrated drug molecules. B) Precise drug release from half of the microswimmers body. Scale bars are 20 microns**.** 59

LIST OF TABLES

Table 3.1. Degree of PEGylation of different polymer groups 19

Table 3.2. Size of nanoparticles with different conditions.....22

Table 3.3. Zeta potential of nanoparticles with different conditions 22

Table 3.4. Data set used to train the ANN. Observed and predicted size & zeta potential values for training data.....30

Table 3.5. ANN training parameters 31

Table 3.6. Observed and predicted size & zeta potential values for the test data set.....31

ABBREVIATIONS

PEG	Polyethylene glycol
ANN	Artificial neural networks
TRAIL	TNF-related apoptosis-inducing ligand
TPP	Tripolyphosphate
NHS	N-Hydroxysuccinimide
TNBS	2,4,6-Trinitrobenzene Sulfonic Acid
US-FDA	The Food and Drug Administration
EPR	Enhanced permeability and retention
TDLW	Two-photon direct laser writing
SPIONs	Superparamagnetic iron oxide nanoparticles
DMSO	Dimethyl sulfoxide
FDA	Fluorescein diacetate
CS-PEG	PEGylated chitosan
CS-PEG NPs	PEGylated chitosan nanoparticles
DLS	Dynamic light scattering
FE-SEM	Field emission scanning electron microscopy
STEM	Scanning transmission electron microscopy
MSE	Mean squarred error
R^2	Correlation coefficient
L. M.	Levenberg-Marquardt
B.R.	Bayesian regularization
G. D. L. R.	Gradient descent with adaptive learning rate
MAL	Maleimide
CS-PEG-CREKA	Chitosan-PEG-CREKA conjugate
ChMA	Methacrylamide chitosan
DOX	Doxorubicin
MA	Methacrylic anhydride
LAP	Phenyl-2,4,6-trimethylbenzoylphosphinate
EDS	Energy-dispersive x-ray spectroscopy

CHAPTER 1

Introduction

Biomaterials have been widely used throughout the history for different applications. One of the most popular applications of biomaterials is designing drug/gene delivery vehicles that can cure certain disesases. In this era, great number of studies have focused on designing biomaterials for the treatment of different cancer types. There are countless studies that used different type of biomaterials in different forms such as nanoparticle, hydrogel etc. for the treatment of cancer, however, few of them were successful. Biomaterial selection is one of the most important parameters when designing such systems. Abundancy, biodegradability and biocompatibility, and functionality of the selected material are crucial. One such example is chitosan, it is a chitin derivative which is the second most abundant natural polymer in the world.[1] It has unique properties such as biodegradability and biocompatibility, and considered as mucoadhesive material due to its cationic nature.[2]

One of the most popular approach for treatment of cancer is nanoparticle-based drug delivery. In this approach, therapeutics agents are entrapped into nanocarriers in order to increase solubility of these agents.[3-4] Nanoparticle-based drug delivery systems also protect therapeutic agents from harsh body environments, and also provides controlled release of drugs.[5] On the other hand, microrobotic drug delivery systems have gained significant attention since microrobotic carriers can be targeted into specific tissues. Chitosan can be a used as base material for both approach, and offers attractive properties due to its functional, biodegradable and biocompatible nature.

This thesis is about the design of different chitosan-based carriers. Chitosan-based nanoparticles and microrobots were designed and studied in detail. Before the experimental study, chitosan polymer was introduced in the beginning of Chapter 2. Then, current status about nanoparticle- and microrobotic-based drug delivery systems were presented. Chapter 3 is about the synthesis of collodially stable chitosan nanoparticles: Chitosan polymer was chemically conjugated with polyethylene glycol (PEG) before the

nanoparticle synthesis to get colloidally stable nanoparticles and fundamental parameters such as PEG chain length and chitosan/PEG ratio were investigated in detail. Furthermore, artificial neural network (ANN) was created with the experimentally obtained size and zeta potential values. Also, nanoparticles with different adhesive properties were synthesized with the help of ANN model. Chapter 4 is about the synthesis of TNF-related apoptosis-inducing ligand (TRAIL) encoded plasmid DNA loaded and CREKA modified (a tumor homing peptide) PEGylated chitosan nanoparticles. These nanoparticles will be used for gene delivery applications for the treatment of various cancer types as future work. Chapter 5 is about a chitosan-based microrobotic system which also has light-triggered cancer drug release modality. According to our knowledge, this unique system is promising to address challenges associated with delivery of therapeutics for the treatment of various diseases.

CHAPTER 2

Literature Review

2.1. Chitosan

Chitosan is a pseudonatural polymer which is made from chitin by deacetylation process. Chitin is the second most abundant natural polymer in the world and the main source of chitin is exoskeleton of shrimp and crabs.[1, 6] Generally, shrimp shells are used to obtain chitosan since shrimp shells are easier to handle.[6-7] Several purification processes are performed to obtain chitosan from chitin. Demineralization, deproteinization and decolororization processes are done before chitin deacetylation reaction.[7] Chemical deacetylation process is used to make chitosan, namely, acetyl groups of chitin is converted into amino groups in the presence of sodium hydroxide (NaOH) at relatively high temperatures. When number of amino groups are more than number of acetyl groups, this new polymer is called chitosan (Fig. 2.1).[1]

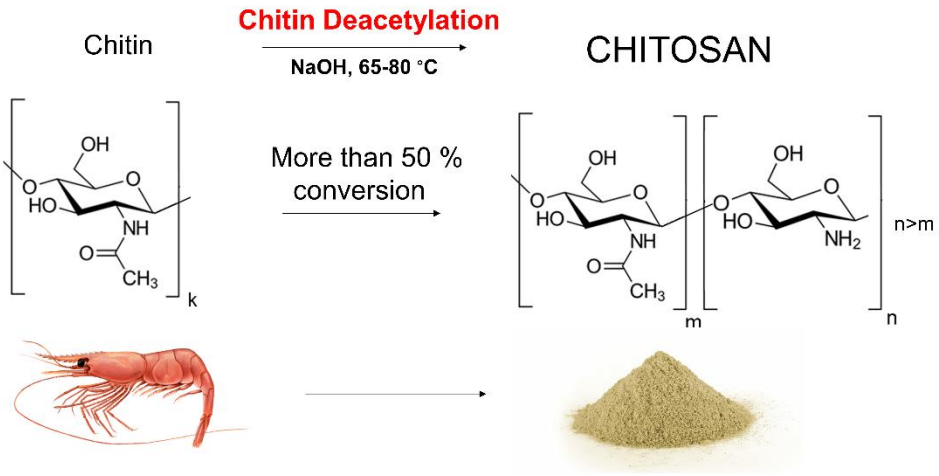

Figure 2.1. Production of chitosan

In general, chitosan is a cationic, biodegradable, biocompatible, non-toxic linear polymer. Chitosan is an semi-crystalline polymer with respect to its degree of deacetylation, it is highly crystalline with degree of deacetylation is equal to 0 or 100%. In middle degree of deacetylation values, crystallinity also decreases which results in the increase in biodegradation rate.[8] Other than these properties, chitosan shows antitumor[9],

antimicrobial[10] and antioxidant[11] activities. Due to these characteristics, chitosan becomes a significant candidate for several biomedical engineering applications.[12] It has applications in several areas such as wound-healing[13], scaffold and tissue engineering[14], drug delivery[15] etc. Due to its unique properties and abundant nature, number of studies about chitosan and its derivatives are in increasing trend.[6]

2.1.1. Applications of Chitosan

2.1.1.1. Tissue Engineering

Tissue engineering refers to use of cells and engineering materials to improve or replace biological functions of real tissues or organs. Chitosan derivatives have been widely studied in tissue engineering applications.[8] Mainly, chitosan derivatives were used as supporting material in artificial tissues due to its physiochemical properties.[16] They provide exceptional physical properties to tissue composites such as high surface area, porosity and tensile strength.[6, 17] In addition to these, they can be fabricated in different forms such as fibers, beads, gels etc.[6] Chitosan-based/supported materials are mainly used in tissue engineering applications as wound healing materials. Many studies has shown that chitosan has certain advantages in wound healing applications, it accelerates tissue regeneration, stimulates the fibroblast synthesis and has homeostasis ability.[16, 18-21] Chitosan supported materials are also promising in cartilage tissue engineering since it supports chondrogenesis that leads to improved neocartilage formation.[16] Chitosan also has application area in bone, liver, nerve tissue engineering and number of studies about chitosan based materials are increasing.[16]

2.1.1.2. Water Treatment

Chitosan is considered to be a efficient for adsorption of pollutants in water treatment applications. Since it has amino and hydroxyl groups, it is able to interact different type of pollutants.[6] Also, chitosan can be further modified for adsorption of different pollutants through its functional amino groups.[22] Especially, chitosan behaves like chelating agent for toxic heavy metal ions, and different chitosan derivatives has been shown to be selective to the specific metal ions.[23] Also, toxic organic molecules such as phenolic compounds, herbicides, pesticides can be adsorbed into chitosan.[24] Even though

the adsorption mechanism is not clearly known, chitosan and chitosan derivatives are good candidates for water treatment applications. The main limitation of chitosan in industrial level water treatment applications is its low solubility in aqueous media.[25] However, chitosan will become a significant candidate in real life water treatment applications with the development of water soluble chitosan derivatives.

2.1.1.3. Drug Delivery Systems

Drug delivery studies about chitosan has started early of 1990s, it has gained more attention in years since it is the only biodegradable and biocompatible cationic polymer.[26] Chitosan is suitable certain delivery routes due to its cationic nature; biocompatibility and biodegradability of chitosan also increases therapeutic efficiency of the drug delivery system. Chitosan carriers can be fabricated in different forms such as tablets, microparticles, micelles, hydrogels, nanoparticles, and these can be either injectable or implantable for different routes.[6]

The attractive properties of chitosan-based drug delivery systems are as follows: (i) Controlled release of anionic or neutral drugs can be achieved[26-27]. (ii) Chitosan-based drug delivery systems show mucoadhesive properties due to cationic nature of chitosan. Since mucus layer exhibit anionic characteristic, chitosan easily interact with mucus layer and residence time of the chitosan carriers dramatically increase. This increases bioavailability and therapeutic efficiency of the system.[15] (iii) They are suitiable for gene delivery systems due to cationic nature of chitosan. They protect nucleic acids from harsh environments and many studies has shown that chitosan carriers are promising for gene delivery applications.[28] (iv) Chitosan-based delivery systems show highly pH dependent behavior. For hydrogels, they show in situ gelling properties which is favorable for drug delivery.[29] Also, chitosan micro- and nanocarriers have more positive charge in lower pH values which is favorable for cancer related applications. (v) Chitosan carriers has permeation enhancing effect due to interaction between cationic chitosan and negatively charged cell membrane.[30]

Chitosan-based drug delivery systems are more suitable for ocular, nasal, buccal delivery routes where higher residence time of carrier is needed.[26] For example, chitosan-

based hydrogels and nanoparticles has significant potential on ocular drug delivery systems due to mucoadhesivity, enhanced retention ability and non-toxic nature of chitosan.[26] Also, many stuides has shown that chitosan carriers had much better ability for nasal uptake of various molecules.[31]

Ionically Crosslinked Chitosan Nanoparticles

Among other platforms, ionically crosslinked chitosan nanoparticles has gained considerable attention due to simplicity of the synthesis process. It does not require organic solvents and harsh experimental conditions, nanoparticles with sub 100 nm size can easily be synthesized with vortex mixer at room temperature. Also, this synthesis method does not require any toxic crosslinker and experiments are highly reproducible.[32-33] In this method, positively charged chitosan chains electrostaticly interacts with negatively charged crosslinker (tripolyphosphate or TPP) under vigorous stirring. Interaction between positively charged chitosan and negatively charged TPP molecules results in electrostatic complexes within an hour.[34]

Even though ionically crosslinked chitosan nanoparticles are easy to fabricate, they suffer from stability issues related to low solubility of chitosan. PEGylation of chitosan appeared to be a solution to obtain collodially stable nanoparticles in different pH values. There are different reaction pathways to obtain PEGylated chitosan. First one is hydroxyl group substitution. In hydroxyl group substitution, amino groups of chitosan and net charge of chitosan are retained. However, this method includes complex reactions which makes the synthesis process harder than its counterparts.[35] On the other hand, amino group substitution is lot easier, and amino-NHS coupling seems to be the easiest option. N-Hydroxysuccinimide (NHS) -Amino coupling can be done at one step, and reaction can be performed in room temperature with a simple mixer. Also, characterization is relatively easier, degree of PEGylation can be determined with 2,4,6-Trinitrobenzene Sulfonic Acid (TNBS) assay or H-NMR.[35] PEGylated chitosan nanoparticles can be syntesized from PEGylated chitosan via ionic crosslinking. These new nanoparticles have solubility in wide range of pH, thus have more realistic

biomedical engineering application. Synthesis of PEGylated chitosan nanoparticles is illustrated in Figure 2.2.

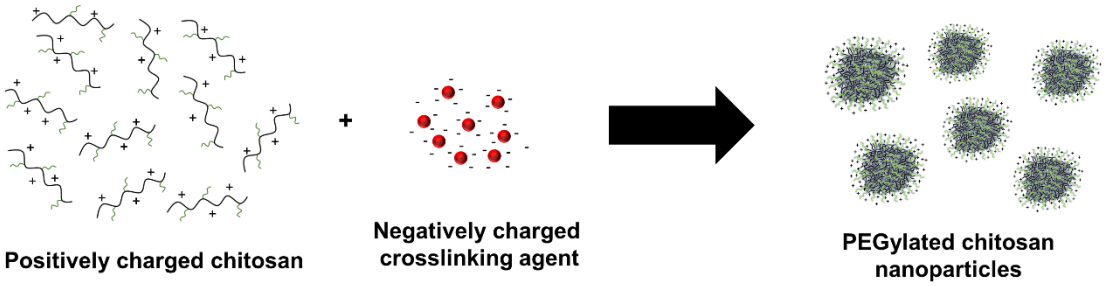

Figure 2.2. Synthesis of PEGylated chitosan nanoparticles

Recently, it was shown that PEGylated chitosan nanoparticles have long circulation time *in vivo*.[36] Thus, PEGylated chitosan nanoparticle systems have become a promising candidate for intravenious administration of drugs besides ocular and intranasal administration of drugs.

2.1.2. Biocompatibility of Chitosan Carriers

Chitosan is approved by The Food and Drug Administration (US-FDA) and European Union.[37] Based on the results from animal models where chitosan nano- and microcarriers were administered, no or minimal toxicity was reported.[38] On the other hand, PEG with different molecular weights have been frequently used as drug carriers due to their biocompatibility, minimal toxicity and good water solubility behavior.[39] Furthermore, PEG is used in numerous studies to improve the biocompatibility of polymers such as chitosan and polylactic acid.[39] In recognition of all these appealing characteristics, chitosan/poly(ethylene glycol) based carriers have been reported as safe, promising biomaterials for biomedical and pharmaceutical applications. In one of these studies, Garg et al. designed a vector to reduce the higher toxicity of gemcitabine which is an anticancer agent.[40] In this study, they compared the biocompatibility of gemcitabine-loaded chitosan-PEG nanoparticles and free gemcitabine *in vivo*. They examined the serum levels of urea/creatinine as an indicator of renal function and ALT/AST/ALP as markers of liver function. The study revealed that gemcitabine loaded gemcitabine-loaded

chitosan-PEG nanoparticles showed minimal alteration in kidney and liver function parameters unlike naked gemcitabine. They also observed enhanced therapeutic effect with gemcitabine-loaded chitosan-PEG nanoparticles compared to that injection with naked gemcitabine *in vivo*. In an another study by Hirpara et al., it was shown that circulation time of rosuvastatin calcium was dramatically increased with PEGylated chitosan nanoparticles *in vivo.*[36] In an another study, Jiang et al. demonstrated that PEGylated chitosan nanoparticles *in vivo* had much less liver toxicity compared to bare chitosan and polyethylene imine.[41]

2.2. Nanoparticle-Based Drug Delivery

Invention of nanotechnology revolutionized many research fields such as medicine, robotics and materials science. Several types of nanomaterials have been developed using the merits of nanotechnology for biomedical related applications. These nanomaterials were used in different fields such as cancer therapy and diagnostics, tissue engineering. Some of the nanomaterial based drugs were commercialized and saved countless people's life.[42]

In today's world, studies about nanocarriers are mostly about cancer therapy applications. Cancer is a severe health problem which causes deaths of millions of people worldwide. The main reason behind the high number of deaths is inefficienct delivery of chemotherapeutics into tumor sites, chemotherapeutics also go to healthy tissues and kill healthy cells.[5] This creates severe toxicity and even causes death of the patient. It is desirable to design chemotherapeutic carriers that goes to only tumor tissues and kill cancerous cells with higher efficiency. At that point, nanoparticle-based drug delivery systems has sparked growing interest due to their unique abilities. Nanoparticle-based drug delivery platforms offer these advantages given below:

- Solubility of chemotherapeutics can be improved, and higher doses of drugs can be used.
- Therapeutic materials (such as drug, gene etc.) are protected from harsh human body environment. Thus, higher levels of drugs can be used, and this decreases side effects.

- Therapeutics agents can be targeted into tumors using functional nanocarriers, so systemic side effects decreases.
- Chemotherapeutic agents can be released with controllable and sustainable manner by tuning inherent properties of nanocarriers.
- On-demand release can be achieved using different stimuli with functional materials, and this eventually increase therapeutic efficiency of the system.[5]

Besides all these desirable characteristics, it was also explored that nanoparticles are accumulated more in tumor tissues other than normal tissues, while naked chemotherapeutics are not that selective. This phenomenon is called as enhanced permeability and retention (EPR) effect[43] and researchers explored that tumor tissues can be passively targeted using nanoparticles.[5] Schematic representation of EPR effect is shown in Figure 2.3.

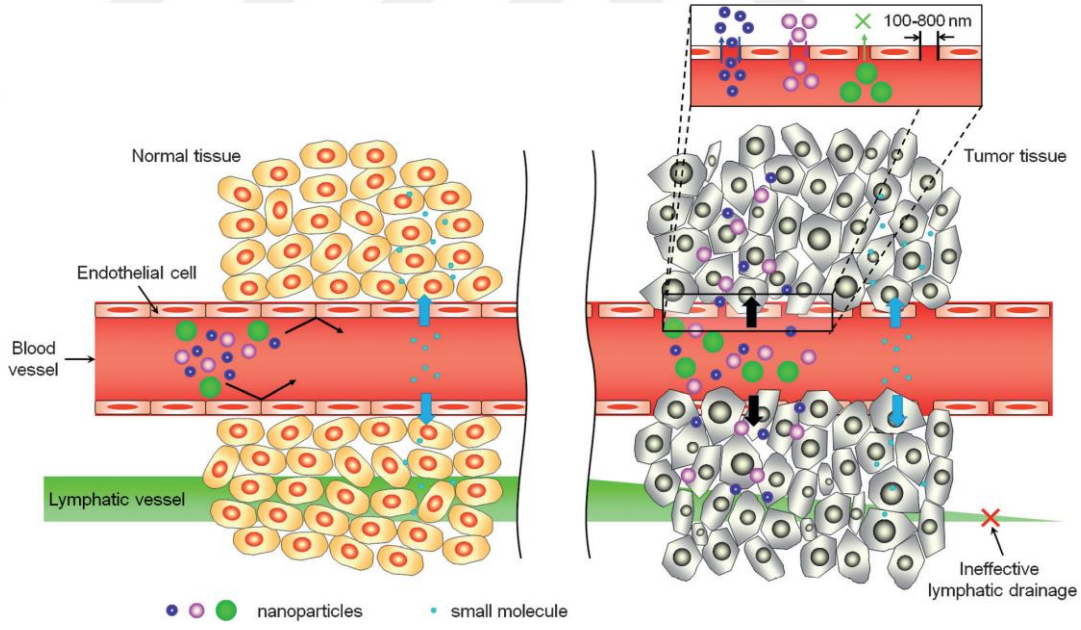

Figure 2.3. Schematic representation of EPR effect, nanoparticles do not accumulate in healthy tissues. They accumulate more in tumor tissues unlike small therapeutic molecules.[5]

In general, nanoparticle-based drug delivery systems offer many attractive properties compared to conventional chemotherapy. Many of nanoparticle based chemotherapeutics were commercialized and used for treatment of several cancer types

and even other diseases.[42] Currently, there is no commercialized chitosan-based drug delivery system, but number of studies are in increasing trend. With the unique properties of chitosan, superior nanoparticle-based drug delivery systems can be commercialized in the future.

2.3. Microrobotic Drug Delivery

Untethered microrobot have gained enourmous attention in biomedical engineering field, since they could access complex regions of human body.[44-45] They could carry and delivery therapeutic agents with high spatiotemporal accuracy, even more, their wireless actuation and controlled steerability could minimize systemic toxicity. As mentioned in previous section, the main problem of the chemotherapy is the biodistribution of chemotherapeutics which also kill healthy cells. The main idea behind microrobotic approach is to transport drug carriers to the diseased site, killing desired cells only.[46] This approach would eventually concentrate the chemotherapeutics on diseased site, and decrease systemic side effect caused by conventional treatment systems. Microrobotic drug delivery is relatively new approach to scientific world and number of studies are currently limited.

There are three main approaches for wireless actuation of microrobots. The first approach is acoustic radiation force; it has certain advantages such as biocompatibility. However, *in vivo* applications can be complex since it requires complex instruments.[47] On the other hand, light induced microrobots become promising alternative, but they are limited to 2D motion. In other words, they cannot be used in *in vivo* applications.[47] Among all these methods, magnetic actuation seems to be the most promising approach. Magnetic microrobots can be actuated in 2D and 3D, controllability of microrobots is high and this enables *in vivo* use of magnetic microrobots.[48]

The design of microrobot is an important aspect, particularly, helical magnetic microswimmers have gained attention in drug delivery applications due to their effectiveness of magnetic torque over magnetic gradient pulling for microscale actuation.[49] Helical microswimmers were previously designed in millimeter scale using a small magnet on the head of a bent cupper wire.[50-51] After this, self-scrolling and glancing

angle deposition techniques were used to fabricate helical magnetic swimmers at micron scale.[52-53] Two-photon direct laser writing (TDLW) technique realized three-dimensional (3D) fabrication of complex polymeric microstructures, and provided to embed superparamagnetic iron oxide nanoparticles (SPIONs) into the microswimmers.[54-58] Thus far, different photosensitive materials have been used with TDLW technique to fabricate helical microswimmers for biomedical engineering applications.[59] In one of the first studies, liposome loaded helical microswimmers were used to perform single cell drug delivery *in vitro*. In this work, drug molecules were successfully delivered to cells.[60] As a next step, single cell transfection was successfully done *in vitro* using plasmid DNA loaded helical microswimmers. In the same study, a single cell was transfected via cell-microswimmer interaction.[61] In another study, helical microswimmers were driven in the peritoneal cavity of a mice. The results has shown that it was possible to drive the microswimmers *in vivo* in the direction of rotating magnetic field.[62] Although there are a significant studies about helical magnetic microswimmers, they need to be improved in terms of physiologically-relevant biodegradation and controlled drug release capabilities, which are crucial for their realistic medical applications.

CHAPTER 3

PEGylation of Chitosan Nanoparticles: An Artificial Neural Network Study

3.1. Introduction

Nanoparticle-based drugs are promising for the treatment of various diseases.[63-67] The main goal of the nanomedicine is to develop nanoparticle-based therapeutics that can overcome the biological barriers. Nanoparticles with optimal surface charge and size improve the therapeutic efficiency of the system, and have gained growing attention for treatment of various diseases.[5]

Bioadhesive polymers can aggressively interact with cells. This increases the mean residence time of the drug and therapeutic efficiency of the system. Chitosan is a bioadhesive polymer which has a wide range of applications from agriculture to biopharmaceutics.[1] Chitosan is biocompatible [36-38, 41] and biodegradable[68] polymer, and is a suitable candidate for mucoadhesive drug and gene delivery systems due to its cationic nature.[26] However, its low solubility at physiological pH limits its biomedical applications.[69] PEGylation is a well-known solution to overcome this problem. Yet, the influences of fundamental parameters such as PEG chain length and chitosan/PEG ratio on the size and zeta potential of chitosan nanoparticles are unknown. Different strategies have been developed for conjugation of PEG to chitosan in previous studies. Amino group substitution of chitosan through n-succinimidyl ester (NHS) derivative of PEG seems to be a good option since it does not require complex reaction pathways or equipments.[35]

Chitosan nanoparticles can be synthesized by using different methods such as emulsificiation solvent diffusion method[70], reverse micellar method[71], microemulsion method[72], ionotropic gelation.[73-74] Ionotropic gelation is the most convenient by far, the reaction can be performed at room temperature with only a magnetic stirrer.[75] In ionotropic gelation, interaction between positively charged chitosan chains and negatively charged polyanion tripolyphosphate (TPP) results in the formation of chitosan nanoparticles in acidic medium.[74] But, chitosan nanoparticles aggregate at neutral pH and hence cannot be used biomedical applications. PEGylation of chitosan chains before nanoparticle formation contribute to the water solubility and stability of nanoparticles. To

the best of our knowledge, the influence of PEG chain length and chitosan/PEG ratio on the inherent properties of ionically-crosslinked and PEGylated chitosan nanoparticles has not been studied before. Also, most of the previous studies in the literature about chitosan nanoparticles reported the size and zeta potential values of nanoparticles after nanoparticle formation, where the pH value of medium is between 4.0-5.5.[76-77] Chitosan nanoparticles behave differently at different pH due to their electrostatic nature and have different size and zeta potential values in different media.[78]

ANN is a computational method to model and analyze non-linear and complex systems.[79] The aim of ANN model is to investigate the effect of independent parameters on systems, and predict inherent properties of nano-systems such as stability, size, encapsulation efficiency, etc.[79-86] With this approach, nanoparticles with required properties can be synthesized based on previous experimental results. Since optimizing the experimental conditions would not be feasible to synthesize nanoparticles with desired size and zeta potential values, we use ANN as an approach to predict desirable chitosan nanoparticle properties without extensive experiments.

In this chapter, we precisely investigated the impact of PEG chain length, chitosan/PEG ratio and pH of the nanoparticle solution on the size and zeta potential of nanoparticles. We used 2, 5 and 10 kDa chain lengths of PEG for PEGylation of linear chitosan chains. PEG chain lengths were selected due to following reasons: Our results demonstrated that conjugation of PEG with molecular weight lower than 2 kDa to chitosan nanoparticles could not provide colloidal stability in neutral pH and conjugation of PEG with molecular weight higher than 10 kDa to chitosan nanoparticles would cause loss of inherent properties of chitosan (i.e. positive charge). Finally, 5 kDa PEG molecular weight was selected for thorough interpretation of whole system. We also used three different PEG number of moles, i.e. 4, 12 and 20 μmole, per 25 mg for each PEG chain length. Under 4 or above 20 μmole, we could not obtain monodisperse distribution of nanoparticles. After nanoparticle synthesis, we changed the pH of nanoparticle solutions to 6.0, 7.0 and 7.4 since pH interval of 6.0-7.4 is relevant for biomedical applications, and measured size and zeta potential values for each group. Having obtained the experimental data, we created an ANN to predict the size and zeta potential of nanoparticles of different

nanoparticle groups to demonstrate that we can precisely engineer the nanoparticle system. Additionally, we investigated the bioadhesion ability of different group of nanoparticles with HEK293-T cell line, where experimental adhesion behavior observed between nanoparticles and cells were consistent with the predicted zeta potential values of the developed model. This, study is important for understanding fundamental aspects of PEGylated chitosan nanoparticle systems, and ultimately for clinical translation of chitosan nanoparticle systems for different therapeutic applications.

3.2. Experimental

3.2.1. Materials

Low-molecular-weight chitosan, anhydrous dimethyl sulfoxide (DMSO), dialysis membrane (14 kDa cut-off), sodium tripolyphosphate (TPP), phosphate buffered saline 1x, fluorescein diacetate (FDA) were purchased from Sigma Aldrich (St. Louis, MO). 2, 5 and 10 kDa methoxypoly(-ethylene glycol) succinimidyl valerate (mPEG-SVA) were obtained from Laysan Bio Inc. (Arab, AL). Glacial acetic acid (99.7+%) was purchased from Alfa Aesar (Ward Hill, MA.). Sodium hydroxide (NaOH) and hydrochloric acid (HCl) and acetone were purchased from Merck. 2,4,6-Trinitrobenzene Sulfonic Acid (TNBS) was purchased from Termo Fisher Scientific. DMEM (41966), fetal bovine serum (FBS), penicillin/streptomycin, DPBS, and trypsin-EDTA (0.05%) were purchased from Gibco (Grand Island, NY). Ultrapure water was used for all experiments (Milli-Q system water - 18.2 MΩ).

3.2.2. Preparation of PEGylated Chitosan

Low molecular weight chitosan (25 mg) was dissolved in 50 mL (2 $mg \cdot mL^{-1}$) acetic acid solution and stirred overnight. Then, pH of the solution was adjusted to 6 with 6 M NaOH. Next, mPEG-SVA (2, 5 and 10 kDa) were dissolved in DMSO at a concentration of 50 $mg \cdot mL^{-1}$. mPEG-SVA solutions were added to chitosan solution at different moles (4, 12, 20 μmoles and others). Reactions were carried out for 2 days and reaction mixtures were dialyzed against ultrapure water for 4 days. Dialyzed mixtures were lyophilized and resulting new polymers (CS-PEG) were dissolved in acetic acid (1

mg·mL^{-1}) solution (with a final of 0.5 mg·mL^{-1} chitosan concentration). PEGylated chitosan solutions were stored at -20 °C until further use.

Degree of PEGylation for each polymer group was analyzed with TNBS assay. Briefly, 80 µL CS-PEG polymers that were prepared with 0.5 mg·mL^{-1} chitosan concentration were incubated separately with 40 µL of 2% (w/v) $NaHCO_3$ and 60 µL of 0.1% (v/v) TNBS reagent at 37°C for 2 hours. Reactions were terminated using 1 N HCl and absorbance of samples were measured with a plate reader (Biotek, Synergy H1) at 345 nm. Unmodified chitosan at 0.5 mg·mL^{-1} concentration was also prepared as a control and degree of PEGylation for different samples were calculated according to the following equation:

$$\text{Degree of PEGylation\%} = 100 - \frac{\text{Absorbance of Sample}}{\text{Absorbance of Unmodified Chitosan}} \times 100 \quad (1)$$

PEGylation of chitosan was also confirmed with FTIR analysis. The FTIR spectra of chitosan, mPEG-SVA and PEGylated chitosan were recorded in the region of 650-4000 cm^{-1} with Thermo Scientific iS10 FTIR.

3.2.3. Synthesis of PEGylated Chitosan Nanoparticles

PEGylated chitosan nanoparticles (CS-PEG NPs) were synthesized with ionotropic gelation method with some modifications.[74] PEGylated chitosan solutions (0.5 mg·mL^{-1} chitosan concentration) were equilibrated at room temperature and pH of the solutions were adjusted to 4.8 with 6 M NaOH. TPP was dissolved (0.5 mg·mL^{-1}) in ultrapure water and pH of the solution was adjusted to 2.5 with 6 M HCl. Chitosan and TPP solutions were mixed at a chitosan to TPP ratio of 4:1 (v/v) and reactions proceeded for 45 minutes. Different nanoparticle groups are named with their PEG chain length type and 25 mg chitosan to PEG ratio (i.e. 2 kDa - 20 µmole).

3.2.4. Characterization of CS-PEG NPs

Size and zeta potential of nanoparticles were characterized with dynamic light scattering (DLS) technique (Zetasizer, Malvern ZS). After synthesis of nanoparticles, each particle solution was sonicated with probe sonicator for short time period and pH of

each solution was adjusted with 1 M NaOH to 6.0, 7.0 and 7.4. Size and zeta potentials were measured after each pH change, the z-average hydrodynamic diameter and zeta potential values were reported with three measurements and values were presented as means ± standard deviation. Morphology and shape of nanoparticles were analyzed using scanning transmission electron microscopy (STEM) and field emission scanning electron microscopy (FE-SEM) (Zeiss Ultra Plus, Bruker, MA). For these experiments, nanoparticle solutions were dropped onto silicon wafer and dried under vacuum. Images were collected at different magnifications.

3.2.5. ANN Study

ANN model was created using MATLAB R2018a. Samples were divided into two categories; train and test. Train data (26 samples) had experimental conditions with regular increments (i.e. PEG MW of 2, 5 and 10 kDa, PEG mole 4-12-20 μmole, pH 6-7-7.4). Test data included randomly chosen conditions within experimental limits (5 samples). Two different artificial neural networks were created to predict the size and zeta potential of nanoparticles. Three independent input parameters were selected: (i) PEG Chain length (kDa), (ii) PEG mole per 50 mg chitosan (μmole) and (iii) pH of the solution. Output parameters for individual neural networks were size and zeta potential. Different backpropagation methods were selected to test the efficiency of ANN, and number of layers was changed until lowest mean squared error (MSE) and highest determination of coefficient (R^2) for test data were obtained. R^2 was calculated according to following equation:

$$\boldsymbol{R^2 = 1 - \frac{\sum_{i=0}^{n}(y_i - \tilde{y})^2}{\sum_{i=0}^{n}(y_i - \overline{y})^2}} \quad (2)$$

where $\boldsymbol{y_i}$, $\boldsymbol{\tilde{y}}$ and $\boldsymbol{\overline{y}}$ are observed, predicted and mean of the dependent variables respectively.

3.2.6. Cell Culture, Cell Attachment and Cell Staining Experiments

HEK293-T cells were cultured in Dulbecco's Modified Eagle Medium (DMEM) supplemented with 10% fetal bovine serum (FBS) and 1% penicillin/streptomycin at 37

°C and 5% CO_2. A stock solution of fluorescein diacetate (FDA) was prepared by dissolving 5 mg/mL of FDA in acetone. The FDA working solution was obtained by adding 0.008 mL of stock solution to 5 mL of DMEM. 80 microliters of nanoparticle solution were dropped onto 1x1 cm glass slides. Glass slides were dried in 65 °C oven. After slides were dried, 30,000 cells were seeded on nanoparticle coated glass slides. Next, cells were incubated for 3 hours, glass slides were washed with phosphate buffered saline (PBS) and 80 µL of FDA working solution was added. The cells were stained with FDA for 4 min at room temperature under dark conditions. After this step, cell culture medium was added onto cells and cells were examined under fluorescence microscopy. Images were taken from glass slides and number of attached cells was quantified using ImageJ.

3.2.7. Statistical Analysis

All quantitative values are presented as means ± standard deviation. All measurements were performed with at least three replicates for each group. Three-way ANOVA test was used for statistical analysis (separately for size and zeta potential, independent parameters were PEG Mole, PEG molecular weight and pH). Student's t-test was used for cell attachment experiments. p-value of less than 0.05 was considered statistically significant.

3.3. Results and Discussion

The important steps of the experimental protocol are summarized in Figure 3.1. As a first step, PEGylated chitosan with different PEG molecular weights (2, 5 and 10 kDa) and chitosan/PEG ratios (25 mg chitosan to 4, 12 and 20 µmol PEG) were synthesized. In the second step, nanoparticles were synthesized using these new polymers with ionotropic gelation method. Size and zeta potential of different nanoparticle groups were measured at different pH values using DLS technique. ANN model was created using the size and zeta potential of different groups. Then size and zeta potential values of random groups were predicted using ANN model. Finally, adhesion behavior of cells with different nanoparticle sets were investigated further through the comparison of zeta

potential predictions of the ANN model with the total number of cells adhered to nanoparticles from experiments.

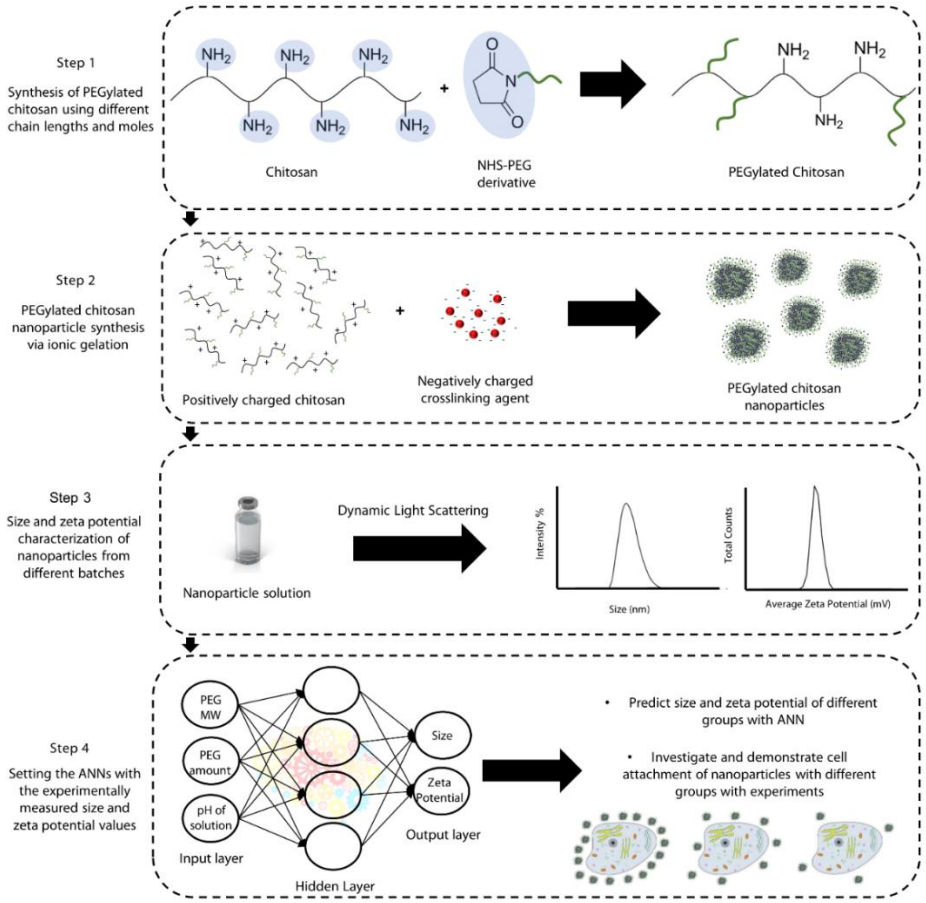

Figure 3.1. Key steps of the study.

3.3.1. Synthesis of PEGylated Chitosan

PEGylated chitosan was synthesized using NHS-Amine coupling chemistry. NHS group of mPEG-SVA reacted with amino groups of chitosan. pH of the chitosan solution was adjusted to 6.0, since nucleophilic/deprotonated state of amino groups reacts more efficiently with NHS group at higher pH values. NHS group also reacts with water (hydrolysis) and resulting product does not have ability to react with amino groups.[87] Thus, NHS-water reaction prevents amino conjugation of NHS-derivative molecules. To minimize this, we used mPEG-SVA polymer which has the highest hydrolysis half-life

among its counterparts.[88] After reaction, dialysis and freeze-drying steps, resulting polymers could be dissolved in water. TNBS assay (amino group quantification assay) was used to characterize the degree of PEGylation for different groups of PEGylated chitosan. Decreases in the concentration of amino groups in PEGylated chitosan samples (compared to unmodified control group) were attributed to PEGylation. Table 3.1 shows the degree of PEGylation of synthesized polymer groups.

Table 3.1. Degree of PEGylation of different polymer groups

	PEG MW (kDa)		
	2	**5**	**10**
	Degree of PEGylation (%)		
20 µmole*	37.4	33.6	21.3
12 µmole*	32.7	29.4	20
4 µmole*	29.9	25.8	18.6

* Number of mole PEG per 25 mg of chitosan

Even though we used the same PEG (or NHS) mole per mass of chitosan, different conjugation degrees were obtained. For example, 2 kDa PEG conjugated to chitosan at higher amounts compared to the other groups while 10 kDa had the lowest conjugation degree. Our theory is the following: Reaction rates were similar for the groups with the same mole but different PEG chain lengths in the beginning. After some time, conjugated PEG chains started to hinder the availability of chitosan monomers. Higher molecular weight PEG chains had much more hindrance effect and prevented the conjugation of other PEG molecules (Fig. 3.2). It was also observed that conjugation degrees were not proportional with the experimental chitosan/PEG ratios used (Table 3.1). Probably, reaction rate of the reaction was high in the beginning of the reaction, some amount of PEG reacted with chitosan. After some time, hindrance effects played important role in

decreasing PEG conjugation rate. Also, hydrolysis of NHS groups in PEG-SVA also slowed down the reactions.

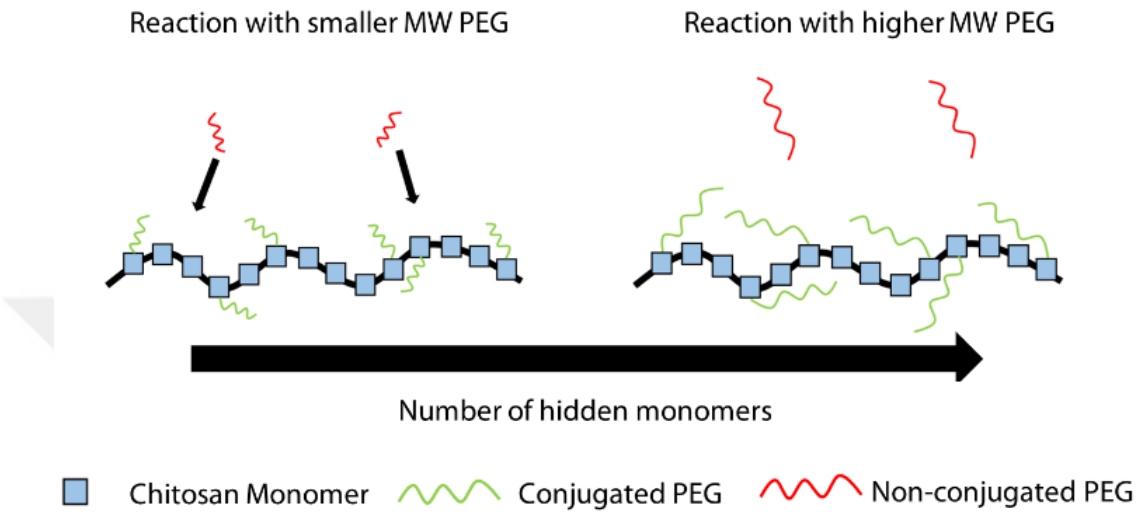

Figure 3.2. Demonstration of hindrance effects due to longer PEG chains. Longer PEG chains hinder available amino group containing chitosan monomers which results in lower conjugation efficiency.

PEGylation of chitosan was also confirmed with FTIR analysis. 5 kDa - 20 µmol PEG condition was selected as a representative group. The IR spectrum of mPEG-SVA has a peak at 1739 cm^{-1}, which corresponds to the free carboxylic group (C=O) on PEG chain (Fig. 3.3). This peak completely disappeared for PEGylated chitosan, which was a significant evidence of PEGylation reaction. Also, amide bond formation was seen at 1562.54 cm^{-1} for PEGylated chitosan. PEGylated chitosan also retained characteristic broad –OH peak between 3000-3500 cm^{-1} region. These results strongly suggested that PEG was chemically conjugated to linear chitosan chains.

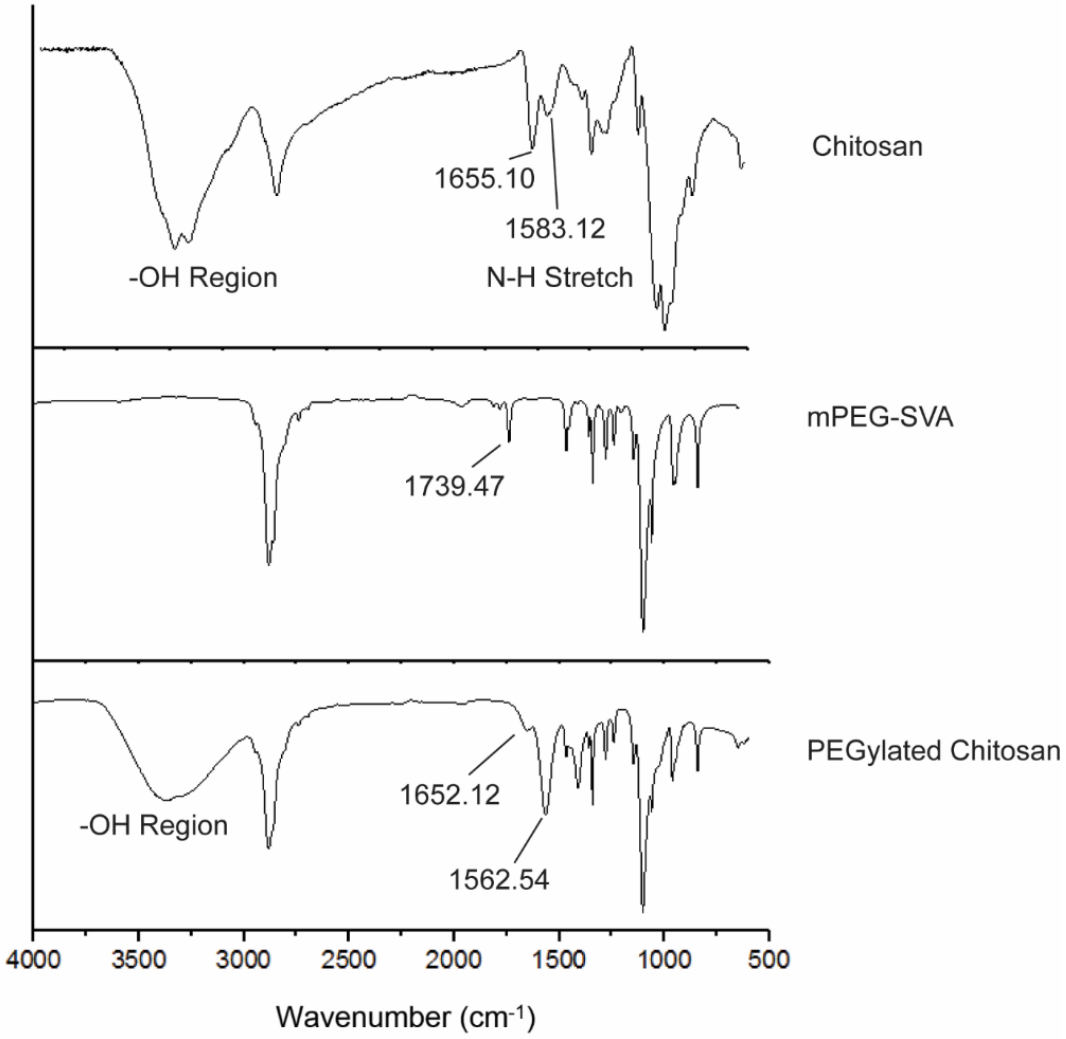

Figure 3.3. FTIR spectra of chitosan, mPEG-SVA and PEGylated chitosan (5 kDa – 20 μmole group)

3.3.2. Synthesis of PEGylated Chitosan Nanoparticles

We synthesized chitosan nanoparticles using different PEGylated chitosan polymers. After preparation of nanoparticles, the resulting pH of the solutions were in between 4.6-4.7 for all samples. pH of solutions were adjusted to 6.0, 7.0 and 7.4. Then, nanoparticles were characterized with respect to their particle size and zeta potential. Size and zeta potential values for all groups are presented in Table 3.2 and Table 3.3 (Raw data is presented in Appendix A, Figure A1-52).

Table 3.2. Size of nanoparticles with different conditions

			PEG MW (kDa)		
			2	5	10
			Particle Size (nm)		
20 µmole*	pH	6	57.50±0.23	56.92±1.36	55.79±0.52
		7	71.55±1.55	66.92±0.36	70.26±0.62
		7.4	112.8±1.21	109.70±0.32	91.90±2.81
12 µmole*	pH	6	72.74±0.10	55.75±1.60	63.56±0.99
		7	75.01±0.13	75.60±1.25	67.32±1.45
		7.4	108.6±0.52	108.5±1.73	112.63±0.4
4 µmole*	pH	6	75.71±1.30	72.40± 0.19	65.75± 0.90
		7	72.09±1.22	74.87±0.96	66.72±0.95
		7.4	Agg.**	153.13±5.65	90.71±1.28

*Number of moles of PEG per 25 mg of chitosan

**Aggregated

Table 3.3. Zeta potential of nanoparticles with different conditions

			PEG MW (kDa)		
			2	5	10
			Zeta Potential (mV)		
20 µmole*	pH	6	11.5±4.53	9.44±3.52	3.28±3.04
		7	4.99±3.20	4.18±4.22	2.36±3.33
		7.4	3.15±2.81	2.29±3.13	2.23±3.14
12 µmole*	pH	6	17.7±3.49	13.2±3.86	9.57±3.56
		7	5.96±3.34	4.75±3.16	3.65±3.35
		7.4	3.83±3.11	2.61±3.11	2.47±3.05
4 µmole*	pH	6	19.8±5.91	18.3±4.17	15.5±4.38
		7	7.07±3.33	6.79±3.03	5.05±3.50
		7.4	Agg.**	3.41±2.96	3.16±3.45

*Number of moles of PEG per 25 mg of chitosan

**Aggregated

Fig. 3.4A demonstrates the size and zeta potential of nanoparticles at different pH values for all groups. Average sizes of nanoparticles were increased at higher pH values

for all groups. The most significant changes in nanoparticle size were observed for the least PEGylated (4 μmole) groups of 2 and 5 kDa PEG MW. 2 kDa - 4 μmole group aggregated irreversibly at pH 7.4. This showed that 29.9% degree of PEGylation (for 2 kDa) was not enough to synthesize stable nanoparticles at 7.4 pH value. On the other hand, we were able to obtain stable nanoparticles using 2 kDa - 12 μmole group which had 32.7% degree of PEGylation. This demonstrates that there is a threshold for the degree of PEGylation between 29.7-32.7% with 2 kDa PEG. Size of 5 kDa - 4 μmole PEG group also increased dramatically from 74.87±0.96 to 153.13±5.65 nm (Table 3.2). The aggregated group, 2 kDa - 4 μmole PEG, had the highest zeta potential between all groups studied at pH 6.0 and pH 7.0. In a widespread manner, nanoparticles with higher zeta potential values are considered to have better stability;[89-90] however, our experiment results suggests that inherent factors of chitosan nanoparticle system play more significant role on the stability of nanoparticles than zeta potential. For 10 kDa - 4 μmole group, the observed change was not as significant as it were with 2 and 5 kDa PEG. Additionally, zeta potential of 10 kDa - 4 μmole group was lower than 2 and 5 kDa - 4 μmole groups. It could be inferred that PEG chain length plays important role on overall stability of the system; chitosan nanoparticles with higher PEG chain lengths have better stability. This phenomenon had less effect at higher chitosan/PEG ratios of 12 and 20 μmole. Size changes were less dramatic for 2, 5 and 10 kDa PEG. For all synthesized groups, we also observed remarkable size increase between pH 7.0 and 7.4. This was probably due to the decrease in repulsion effects between nanoparticles, which eventually resulted in increases in size of the nanoparticle system. Overall, two main factors play important roles on the general stability on PEGylated chitosan nanoparticles: (i) hydrogen bonding between grafted PEG chains and water positively contributes the stability of nanoparticle system, (ii) stronger repulsion forces between nanoparticles also positively contribute to the general stability of the system; but this has much less effect compared to the previous one.

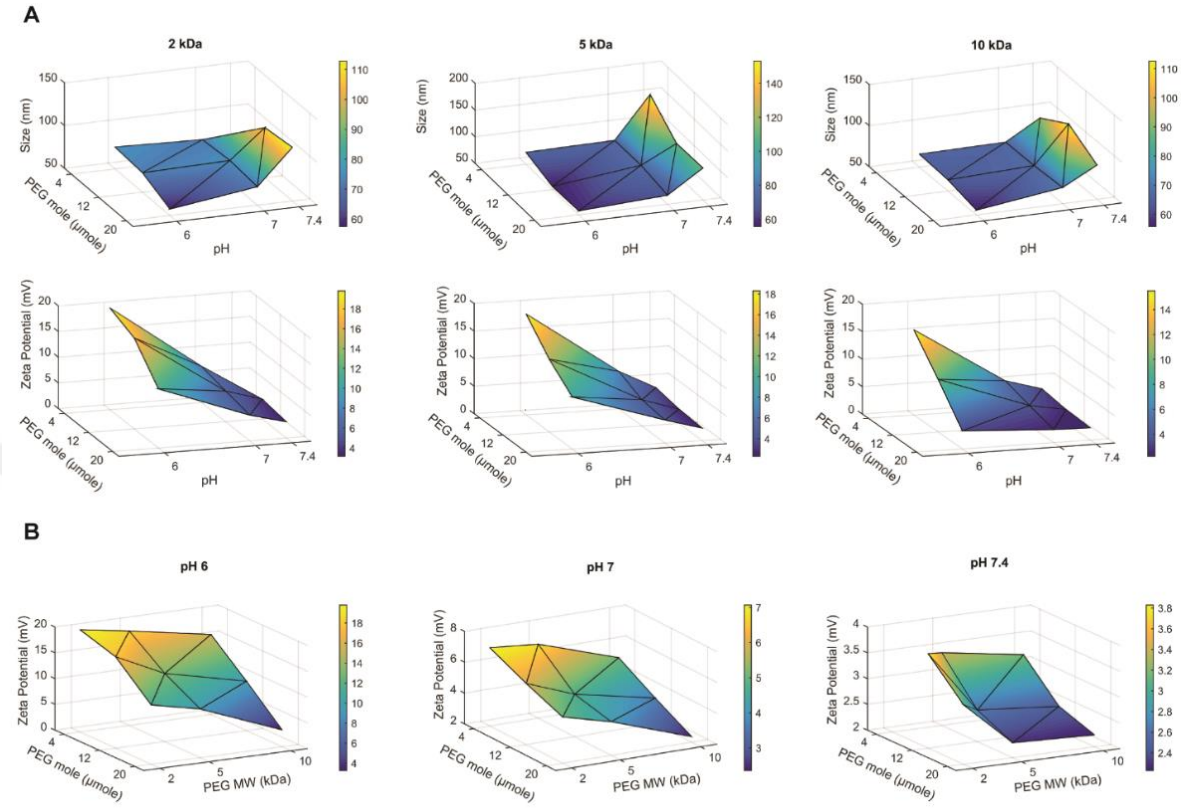

Figure 3.4. Three-dimensional surface plots of size and zeta potential of nanoparticles with respect to different independent variables. Plots were sketched using Table 2 and Table 3. **A)** Size and zeta potentials of nanoparticles for different PEG chain lengths. **B)** Zeta potentials of different PEGylated nanoparticles at different pH values. Note: $p<0.005$ for size and zeta potential values separately.

Zeta potential of all nanoparticle groups decreased while pH was increased from 6.0 to 7.4 as expected. Deprotonation of amino groups caused decreases in zeta potential values. Nanoparticles with higher PEG doses had less zeta potential in individual PEG groups (2, 5 and 10 kDa) (Fig. 3.4B). An unexpected phenomenon was observed in zeta potentials of different groups: Even though more amino groups were consumed after the synthesis of groups that have smaller chain length (Table 3.1), zeta potentials of these groups were much greater than groups with less conjugation with higher PEG chain length (Table 3.3). Since amino groups contribute the surface charge, it was expected that more amino group containing nanoparticles would result in higher zeta potential. However, experimental observations showed that there was an opposite trend (Fig. 3.3B). This

opposite trend was probably due to the hindrance effects caused by PEG with higher chain lengths on the surface of nanoparticles (Fig. 3.5). Opposite trend could also be explained by shift of hydrodynamic shear plane due to surface PEG groups. This effect was more obvious for 10 kDa PEG nanoparticle groups. For instance, 10 kDa - 20 μmole PEG group has 21.3% degree of PEGylation, namely, 21.3% of total amino groups were consumed. On the other side, 2 kDa - 20 μmole group has 37.4% degree of PEGylation which had much smaller number of amino groups compared to 10 kDa - 20 μmole group. Zeta potentials of nanoparticles were measured as 3.28±3.04 and 11.5±4.53 for 10 kDa - 20 μmole and 2 kDa-20 μmole groups respectively at pH 6.0. Even though 10 kDa - 20 μmole group had greater number of amino groups, its zeta potential value was three times less than 2 kDa - 20 μmole group. Same trend was observed for all groups, and this confirmed the opposite trends suggested above.

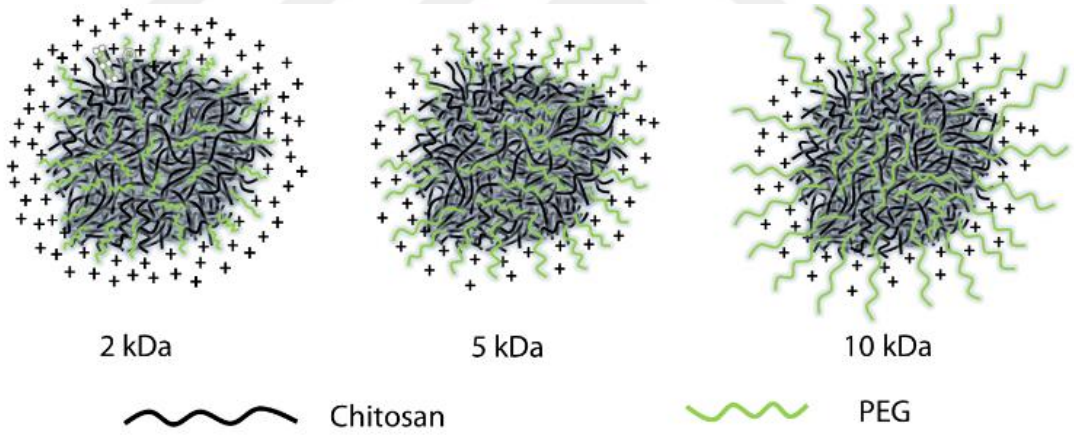

Figure 3.5. Schematic presentation of hindrance effects. Higher PEG chains mask a greater number of protonated amino groups on the surface of nanoparticles.

FE-SEM and STEM techniques were used to analyze morphology and shape of nanoparticles. 5 kDa - 20 μmole and 10 kDa - 20 μmole groups were selected as representative groups for FE-SEM experiments. FE-SEM experiments showed that nanoparticles have spherical shape, and size of nanoparticles were consistent with DLS results (Fig. 3.6 and 3.7). For STEM experiments, 2 kDa - 20 μmole group was selected as representative group. STEM images also confirmed that nanoparticles have spherical shape (Fig. 3.8).

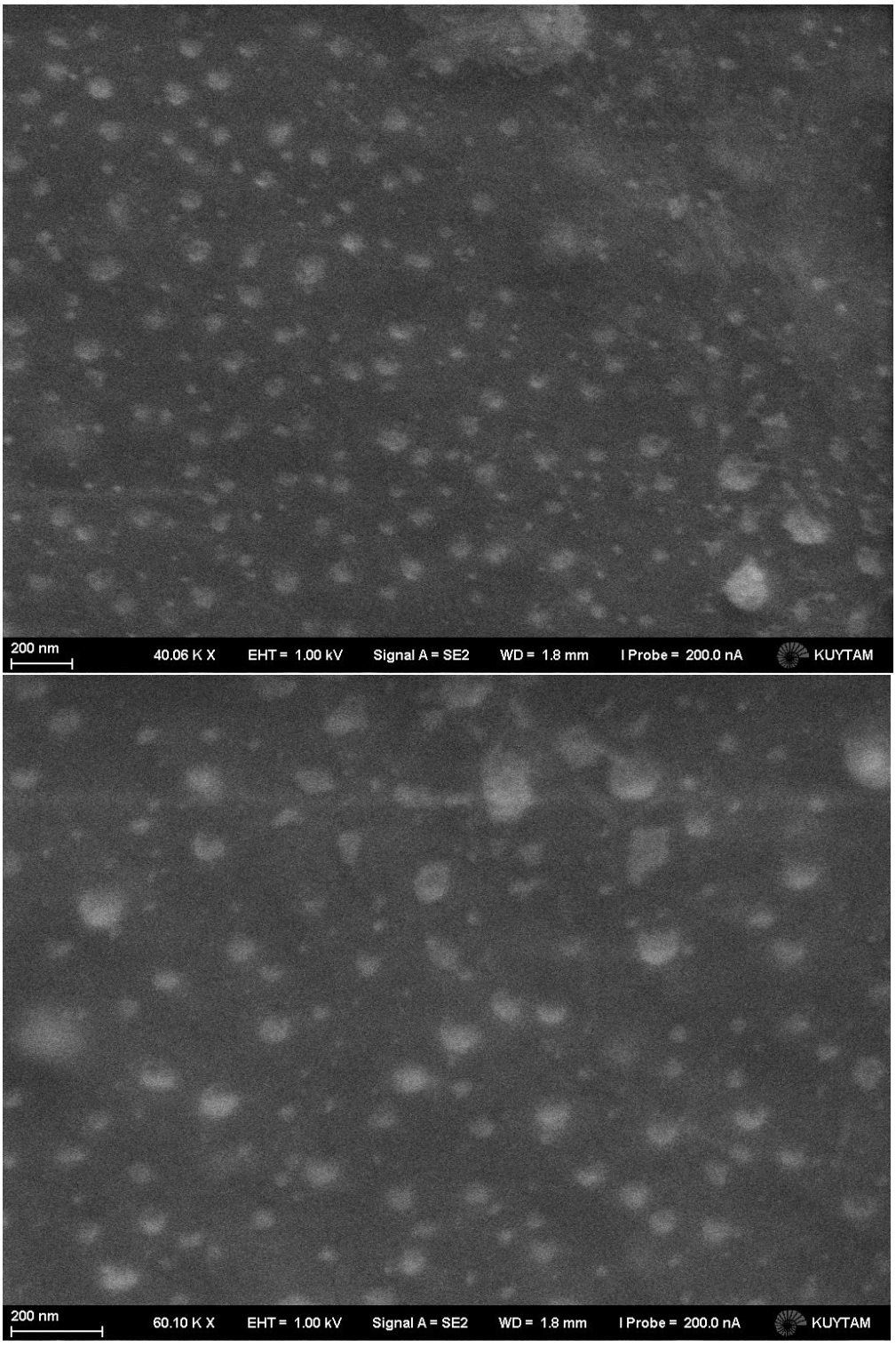

Figure 3.6. FE-SEM images of 5 kDa PEG – 20 μmole nanoparticles

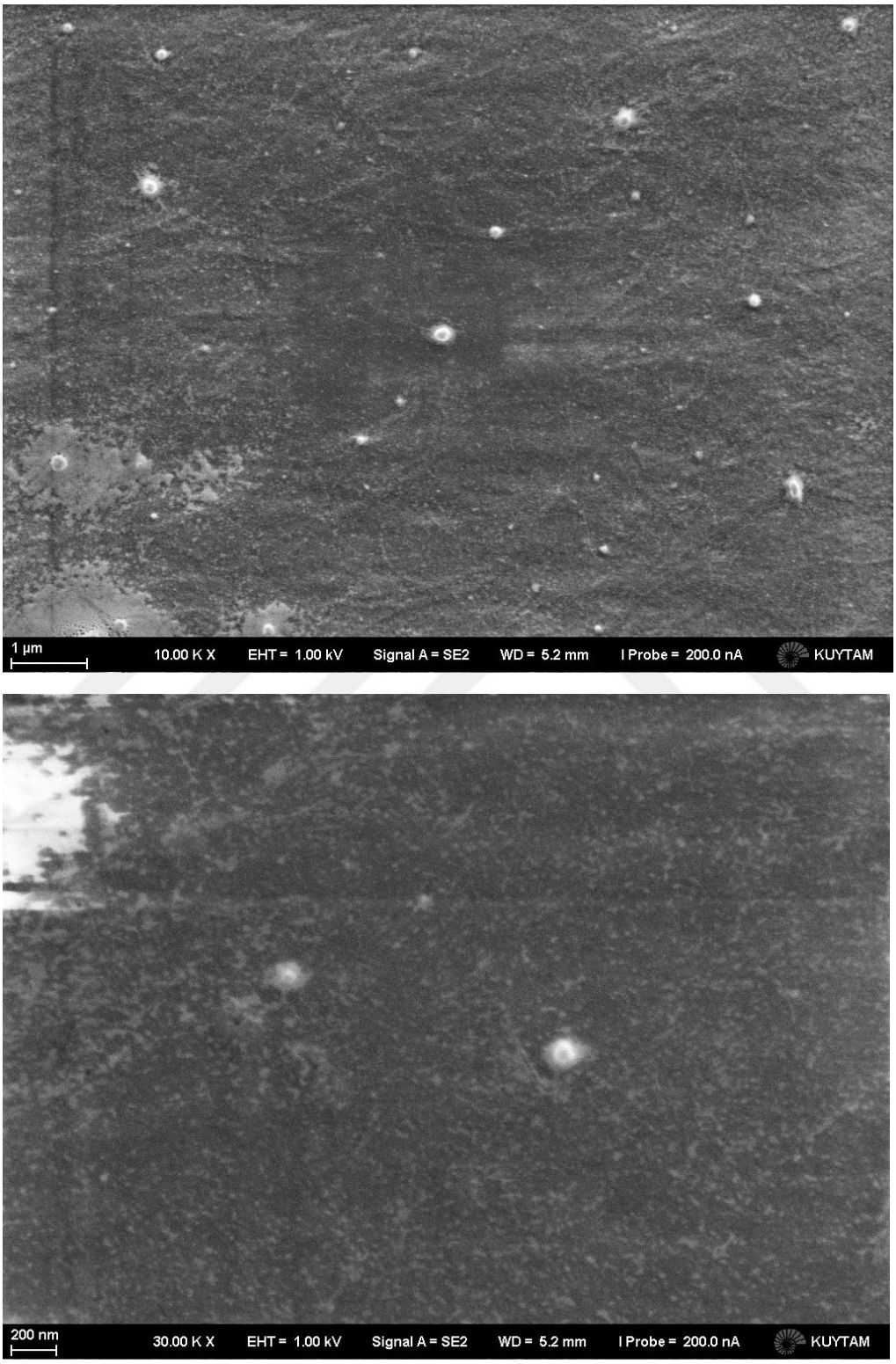

Figure 3.7. FE-SEM image of 10 kDa PEG – 20 µmole nanoparticles

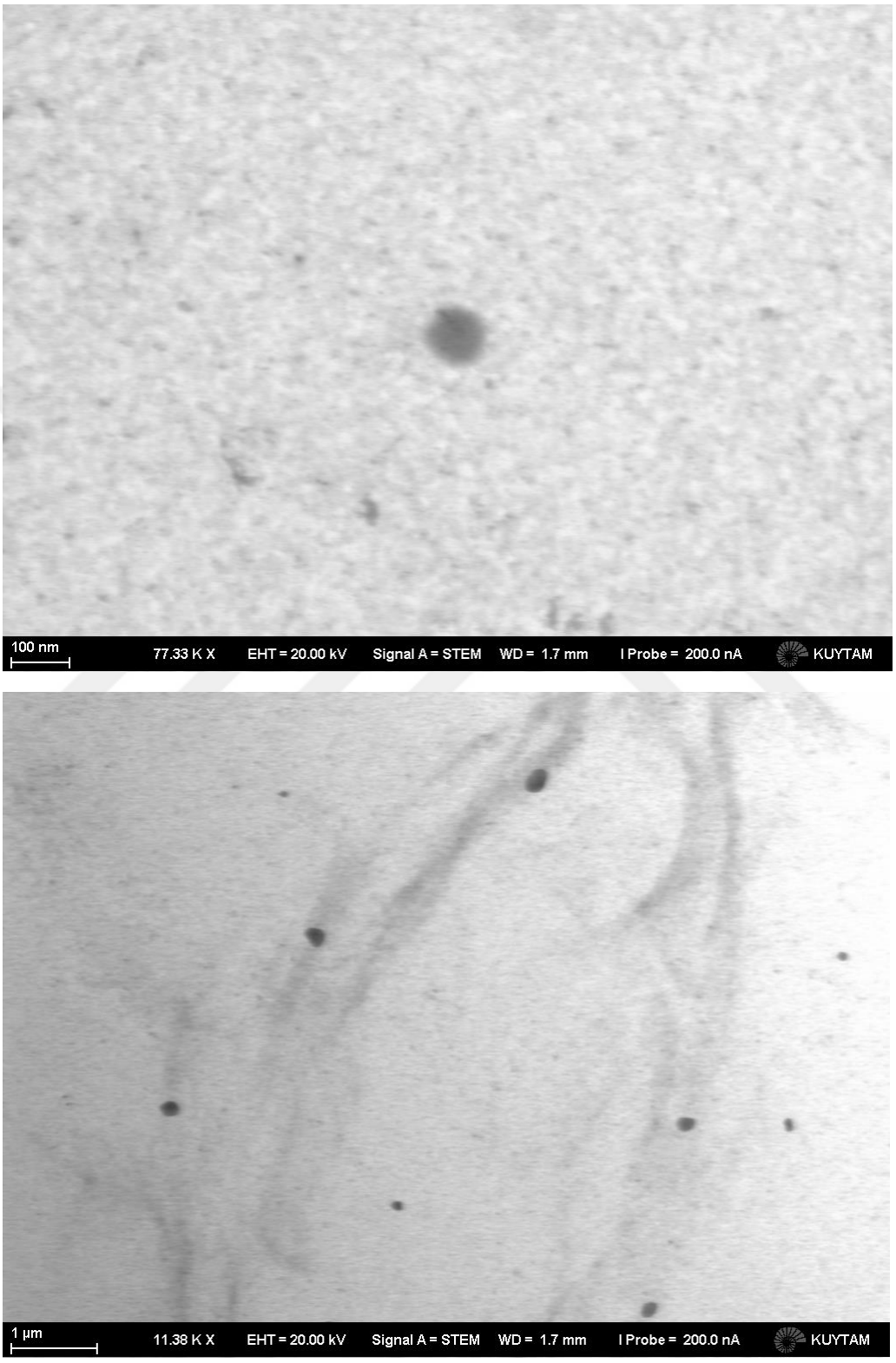

Figure 3.8. STEM images of a 2 kDa PEG – 20 µmole nanoparticles

3.3.3. ANN Model

ANNs with different backpropagation methods were created to test quality of the networks (MATLAB Code is presented in Appendix B). MSE and R^2 values of test data (for size and zeta potential separately) are presented in Appendix C, Table C1. Three representative backpropagation methods (Levenberg–Marquardt, Bayesian Regularization, Gradient descent with adaptive learning rate) were selected among 9 to demonstrate the optimization process (Fig. 3.9). Levenberg–Marquardt algorithm with 1 layer was selected for the size prediction of nanoparticles. This method resulted in the highest R^2 and the lowest MSE value for the size of the nanoparticles (Figure 3.9A). R^2 values were 0.8734 and 0.7869 for train and test data, respectively.

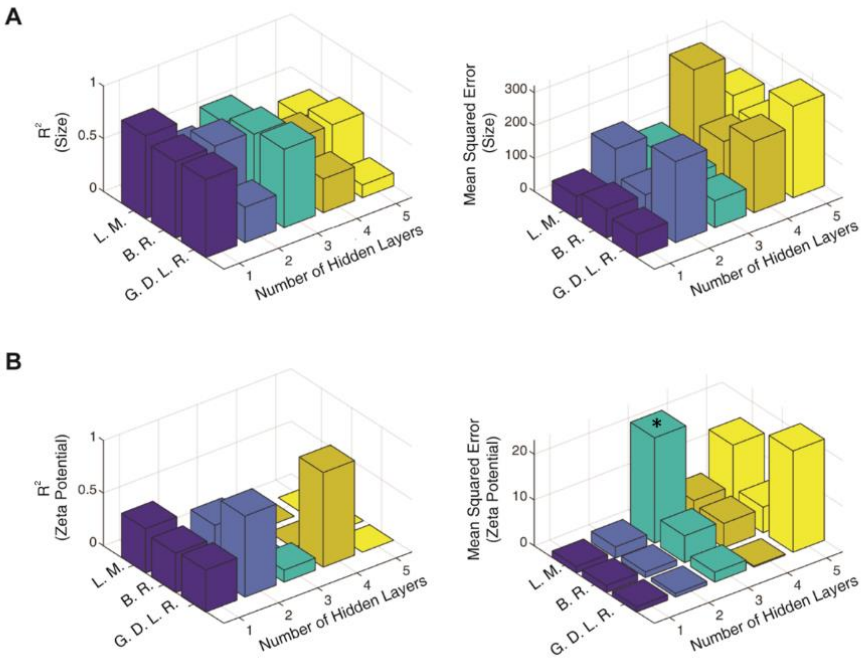

Figure 3.9. Optimization of ANNs. MSE and R^2 values of test data for the different backpropagation methods. A) ANN optimization for size. L. M. with 1 layer was selected. B) ANN optimization for zeta potential, G. D. L. R. with 4 layers was selected.
(L. M. = Levenberg–Marquardt, B. R. = Bayesian regularization, G. D. L. R. = Gradient descent with adaptive learning rate)

*This bar exceeded the graph; real value is 189.84

These values confirms that the created model is competent prediction of other groups.[91] Gradient descent with adaptive learning rate backpropagation method with 4 layers was selected since it had the lowest MSE and highest R^2 value for zeta potential (Figure 3.9B). R^2 were found as 0.9892 and 0.8987 for train and test data, respectively. These values suggested that the model had good capability of prediction of other groups. Observed and predicted size and zeta potential values for training data is given in Table 3.4.

Table 3.4. Data set used to train the ANN. Observed and predicted size & zeta potential values for training data.

	Input Parameters			Output Parameters					
Sample Name	PEG MW (kDa)	PEG Mole* (µmole)	pH	Observed Size (nm)	Predicted Size (nm)	Size Error (nm)	Observed Zeta Potential (mV)	Predicted Zeta Potential (mV)	Zeta Potential Error (mV)
1	2	4	6	75.71	64.26	-11.45	19.80	19.69	-0.11
2	2	4	7	72.09	75.35	3.26	7.07	7.58	0.51
3	2	4	7.4	Agg.**	-	-	Agg.**	-	-
4	2	12	6	72.74	64.24	-8.5	17.70	16.93	-0.77
5	2	12	7	75.01	72.58	-2.43	5.96	6.04	0.08
6	2	12	7.4	108.60	125.62	17.02	3.83	4.10	0.27
7	2	20	6	57.50	64.22	6.72	11.50	11.70	0.2
8	2	20	7	71.55	70.50	-1.05	4.99	4.41	-0.58
9	2	20	7.4	112.80	110.40	-2.4	3.15	2.87	-0.28
10	5	4	6	72.40	64.24	-8.16	18.30	18.74	0.44
11	5	4	7	74.87	73.31	-1.56	6.79	6.37	-0.42
12	5	4	7.4	153.13	130.93	-22.2	3.41	4.24	0.83
13	5	12	6	55.75	64.23	8.48	13.20	14.08	0.88
14	5	12	7	75.60	71.05	-4.55	4.75	4.55	-0.2
15	5	12	7.4	108.5	114.40	5.9	2.61	3.31	0.7
16	5	20	6	56.92	64.22	7.3	9.44	8.67	-0.77
17	5	20	7	66.92	69.35	2.43	4.18	3.95	-0.23
18	5	20	7.4	109.70	101.96	-7.74	2.29	2.63	0.34
19	10	4	6	65.75	64.23	-1.52	15.50	15.34	-0.16
20	10	4	7	66.72	70.71	3.99	5.05	4.26	-0.79
21	10	4	7.4	90.71	111.88	21.17	3.16	2.91	-0.25
22	10	12	6	63.56	64.21	0.65	9.57	9.15	-0.42
23	10	12	7	67.32	69.09	1.77	3.65	3.26	-0.39
24	10	12	7.4	112.63	100.07	-12.56	2.47	1.96	-0.51
25	10	20	6	55.79	64.21	8.42	3.28	4.88	1.60
26	10	20	7	70.26	67.87	-2.39	2.36	2.82	0.46
27	10	20	7.4	91.90	91.18	-0.72	2.23	2.17	-0.06

* Number of PEG mole per 25 mg of chitosan

** Aggregated

Training parameters of ANNs is presented in Table 3.5.

Table 3.5. ANN training parameters

Output Parameters	Size	Zeta Potential
Backpropogation type	Levenberg–Marquardt	Gradient descent with adaptive learning rate
Number of hidden layers	1	4
Learning rate	0.01	0.01
Maximum number of epochs	1000	1000
Minimum performance gradient	1e-7	1e-5
Transfer function in hidden layers	Hyperbolic tangent sigmoid	Hyperbolic tangent sigmoid and Linear transfer function

Test results has shown that created ANNs could efficiently estimate the size and zeta potential of different groups (Table 3.6, Appendix A, Figure A53-62).

Table 3.6. Observed and predicted size & zeta potential values for the test data set.

	Input Parameters			Output Parameters					
Sample Name	PEG MW (kDa)	PEG Mole* (μmole)	pH	Observed Size (nm)	Predicted Size (nm)	Size Error (nm)	Observed Zeta Potential (mV)	Predicted Zeta Potential (mV)	Zeta Potential Error (mV)
27	5	12	6.5	55.35	64.75	9.4	6.87	6.99	0.12
28	10	4	6.3	63.41	64.38	0.97	9.50	9.67	0.17
29	2	15	6.4	60.36	64.56	4.2	8.68	8.92	0.24
30	5	8	7.2	74.82	85.59	10.77	5.08	4.36	-0.72
31	5	8	6.5	54.11	64.84	10.73	7.67	8.45	0.78

* Number of PEG mole per 25 mg of chitosan

Based on the ANN results, PEGylated chitosan nanoparticles with required size and zeta potentials can be synthesized using the artificial neural network results. This model significantly reduces the experimental efforts for obtaining nanoparticles with required properties. Since adhesion behavior of nanoparticles to cells is highly sensitive to zeta potential differences, adhesion ability of nanoparticles to cells and can be predicted with our model. As a future work, this model could be useful to tune transfection efficiency of nanoparticles for gene delivery applications.

3.3.4. Cell Attachment Experiments

Two sets of experiments were performed to show that surface charge has direct effect on cell-nanoparticle interaction. In the first set, nanoparticles were synthesized from 2 kDa - 12 μmole PEG group and these nanoparticles were coated on glass slides. Cells were seeded on the uncoated and nanoparticle coated glass slides, and pH of cell culture media were 6.5 and 7.4 (Fig 3.10A). It was observed that there were a greater number of cells on the nanoparticle coated glass slides compared to bare glass surfaces at pH 6.5 (Fig 3.10B). There were also a greater number of cells at pH 6.5 compared to the condition at pH 7.4. This strongly confirms that higher surface charge of nanoparticles promotes the adhesion of cells. However, at pH 7.4, it was observed that there were a greater number of cells on uncoated glass slide than coated glass slide. There may be two main reasons for this: (i) zeta potential of nanoparticles at pH 7.4 was not strong enough for cell adhesion, (ii) a different adhesion mechanism was dominant at 7.4 pH.

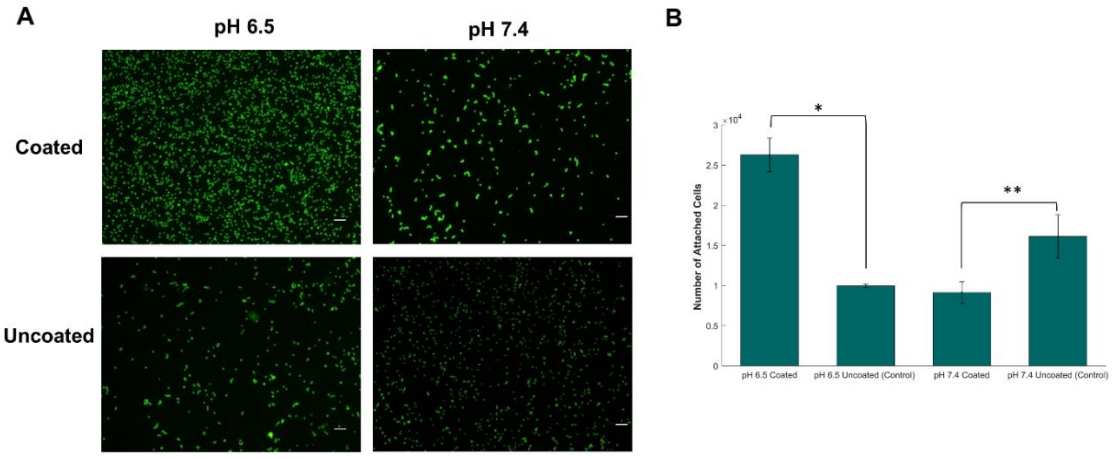

Figure 3.10. Cell attachment experiments in different pH values. Glass surfaces were coated with nanoparticles from 2 kDa - 12 μmole group. A) FDA staining of living cells. There are a greater number of cells on coated surfaces in pH 6.5. B) Quantification of number of attached cells on glass slides. pH 6.5 group has much greater number of cells compared to pH 7.4. For both groups, uncoated slides have a smaller number of cells. Note: * $p<0.005$, ** $p<0.05$

Having confirmed that zeta potential has direct impact on adhesion of cells, second set of experiments was performed. In the second set, 2, 5 and 10 kDa - 12 μmole nanoparticle groups was compared at pH of 6.5. Zeta potential of these nanoparticles were

measured as 8.35, 6.87 and 4.94 mV for 2 kDa - 12 µmole, 5 kDa - 12 µmole and 10 kDa - 12 µmole groups, respectively at pH of 6.5 (Appendix A53, 63, 64). Then, cell attachment experiments with these three groups were performed. It was observed that 2 kDa group had the highest number of attached cells (Fig. 311A, B). Linear trend was observed for 2, 5 and 10 kDa - 12 µmole groups in terms of number of attached cells (Fig. 3.11C). This linear trend was used as a calibration curve. Linear curve was utilized to estimate the number of attached cells on the coated glass slides for different group of nanoparticles (Fig. 3.11C).

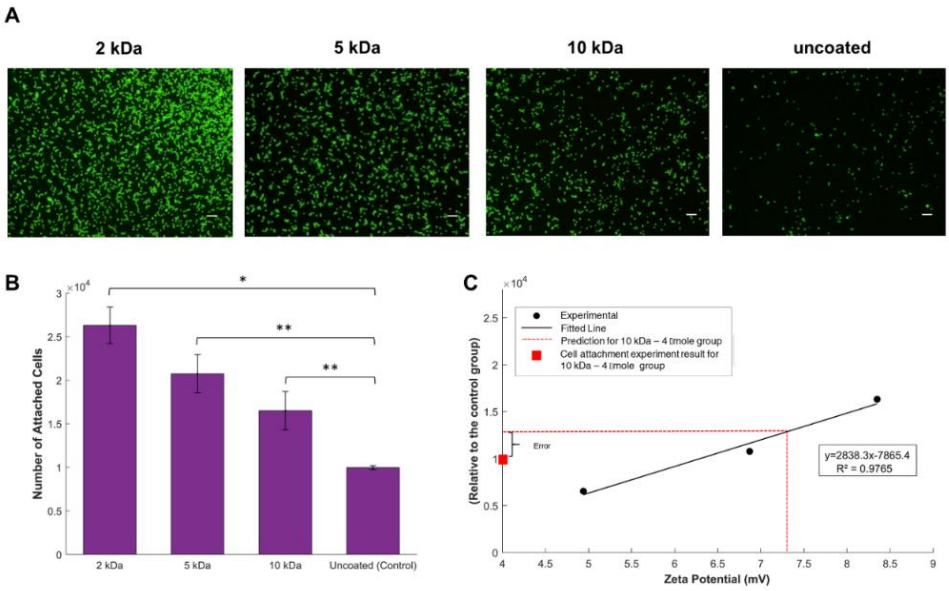

Figure 3.11. Cell attachment experiments with 2, 5 &10 kDa – 12 µmole groups in pH 6.5. **A)** FDA staining of attached cells. 2 kDa group has the highest number of attached cells according to its zeta potential. **B)** Quantification of number of attached cells. **C)** Zeta potential versus number of attached cells. Effect of negative control was subtracted from each group. Number of attached cells was estimated from the fitted line. Note: * $p<0.005$, ** $p<0.05$

First, ANN model was used to estimate zeta potential value of a different nanoparticle group at pH 6.5. Then zeta potential value was substituted into the equation of the fitted line to estimate number of attached cells (relative to control group). 10 kDa - 4 µmole group was used in ANN model, and estimated zeta potential value was 7.34 mV at pH 6.5. Estimated zeta potential value was substituted into the equation of the fitted

line and 12,968 attached cells (relative to the control group) was obtained. Finally, the real cell adhesion experiment was performed to compare the prediction with the experimental observation. There were 9,971 of attached cells on the surface (relative to the control group). This demonstrated that the model had relatively good ability to predict number of attached cells.

3.4. Conclusions

The impact of PEG chain length and chitosan/PEG ratio on size and zeta potential of nanoparticles was carefully investigated at different pH values. It was found out that smaller chain lengths of PEG reacted more with chitosan. It was also explored that nanoparticles conjugated with higher PEG chain length had smaller zeta potential, even though they had lower conjugation degree. This was due to hindrance of the surface charge of particles by longer PEG chains. Having explored the fundamentals of the system, ANN model was developed based on the experimental data. This model was used to predict size and zeta potential values of nanoparticle groups at different conditions. Model was efficient to estimate size and zeta potential of different groups. This suggested that PEGylated chitosan nanoparticles with desired size and surface charges can be obtained based on the predictions from the ANN model. As a final step, it was demonstrated that the difference between adhesion ability of nanoparticles based on their zeta potential to cells *in vitro*. Also, adhesion ability of nanoparticles and cells was predicted based on ANN results. In conclusion, this study is useful to synthesize chitosan nanoparticles with desired properties for various delivery systems, for possible drug and gene delivery applications.

CHAPTER 4

Synthesis of PEGylated Chitosan Nanoparticles as a Gene Delivery Vehicle

4.1. Introduction

Gene therapy is the delivery of nucleic acids (RNA and DNA) into the unhealthy cells for the treatment of various diseases.[92] Since nucleic acids have net negative charge, they are not easily uptaken by negatively charged cell membrane.[28, 93] Thus, different nucleic acid carrier systems have been established including viral and non-viral delivery systems.[28] Chitosan is a promising canditate as a non-viral gene delivery carrier due its cationic nature, biodegradability and biocompatibility.

Nanoparticle-based delivery of therapeutic agents offer several advantages including improved delivery of agents, protection of agents from the surrounding environment and targeted delivery of therapeutic agents.[5] Chitosan nanoparticles can be fabricated with various techniques[75], and ionic gelation is the easiest method to fabricate chitosan nanoparticles since it does not require complex setups or reaction pathways.[74] However, low solubility of chitosan restritcs the potential biomedical engineering applications. PEGylation of chitosan is a well-known method to increase solubility and circulation time of chitosan carriers.[35]

Another concern for nanoparticle-based delivery is the size of the nanoparticles. Many studies have been demonstrated that nanoparticles having 1-100 nm size are more advantageous compared to microparticles, namely, nanoparticles have much higher cellular uptake compared to microparticles.[5] Also, it was shown that nano- sized carriers accumulates more in tumor tissues compared the naked therapeutics or microparticles due the enhanced permeability and retention effect.[43] In addition to these, peptide modification of nanoparticles have become a promising approach since it makes nanoparticles selective to cancer cells only.[94] In that way, side effects of nanoparticles would be much lower and this increases therapeutic efficiency.

Here, we present a PEGylated chitosan nanoparticle-based gene delivery vehicle which also has CREKA peptide modification. CREKA peptide modification has been

proven to increase cellular uptake of nanoparticles to cancer cells[95-96], and CREKA peptide was conjugated to chitosan polymer backbone by means of a PEG linker. Also, TNF-related apoptosis-inducing ligand (TRAIL) encoded plasmid DNA was encapsulated into nanoparticles with high encapsulation efficiency. This nanoparticle delivery system is promising for the delivery of TRAIL gene for the treatment of various cancer types.

4.2. Experimental

4.2.1. Materials

Low-molecular-weight chitosan, anhydrous dimethyl sulfoxide (DMSO), dialysis membrane (14 kDa cut-off), sodium tripolyphosphate (TPP), cysteine hydrochloride monohydrate, sodium phosphate, ethylenediaminetetraacetic acid (EDTA) were purchased from Sigma Aldrich (St. Louis, MO). SVA-PEG-MAL 5 kDa was purchased from Laysan Bio (Arab, AL). Glacial acetic acid (99.7+%) was purchased from Alfa Aesar (Ward Hill, MA.). Sodium hydroxide (NaOH) and hydrochloric acid (HCl) and acetone were purchased from Merck. CREKA peptide was purchased from Elim BioPharm (Hayward, USA). Ellman's Reagent and Pierce BCA Protein Assay Kit were purchased from Thermo Fisher Scientific.

4.2.2. Synthesis of Chitosan-PEG-CREKA Conjugate

Low molecular weight chitosan (25 mg) was dissolved in 50 mL (2 $mg \cdot mL^{-1}$) acetic acid solution and stirred for overnight. Then, pH of the solution was adjusted to 6 with 6 M NaOH. After that, 100 mg of SVA-PEG-MAL in 2 mL DMSO and 20 mg of CREKA in 3 mL (CREKA amount is excess) of PBS are added to chitosan solution. Reaction was proceeded for 2 days and resulting mixture was dialyzed for 4 days against DI water. Dialyzed mixture was lyophilized and stored for further use.

4.2.2.1. TNBS and Ellman's Assay

Conjugation of PEG molecule to chitosan is confirmed by TNBS assay. Experimental procedure for TNBS assay was given in chapter 2 ("2.2.2. Preparation of PEGylated Chitosan" section).

Conjugation of CREKA to PEG linker was confirmed with Ellman's assay based on consumption of -SH groups. To perform Ellman's assay, cysteine standard curve was prepared using cysteine hydrochloride monohydrate. Initially, reaction buffer was prepared containing 0.1 M sodium phosphate and 1 mM EDTA at pH 8. Then cysteine hydrochloride monohydrate was added with different concentrations to reaction buffer (0, 0.25, 0.5, 0.75, 1, 1.25 and 1.25 mM). Ellman's reagent was prepared in 10 mL reaction buffer at the concentration of 4 $mg \cdot mL^{-1}$. For standards and unknown sample (Chitosan-PEG-CREKA), 250 µL of sample was mixed with 50 µL Ellman's solution. 2.5 mL of reaction buffer was added to resulting mixture and incubated at room temperature for 15 minutes. Absorbance at 412 nm was measured for all samples. For Chitosan-PEG-CREKA sample, absorbance of mixture was measured just before dialysis part.

4.2.2.2. Peptide Quantification with Pierce™ BCA Protein Assay Kit

Peptide amount in chitosan-PEG-CREKA conjugate was quantified with Pierce™ BCA Protein Assay Kit. Initially, bovine serum albumin (BSA) standards were prepared for the calibration curve. Albumin standards were prepared in DI water in various concentrations (0, 25, 125, 250, 500, 750, 1000, 1500 and 2000 $\mu g \cdot mL^{-1}$). 25 µL of standard solution were mixed with 200 µL of Pierce working reagent and incubated for 30 min at 37 °C. Absorbance was measured at 562 nm. For chitosan-PEG-CREKA sample, freeze dried sample was dissolved with the concentration of 1000 $\mu g \cdot mL^{-1}$.

4.2.2.3 FT-IR Analysis

Conjugation of CREKA peptide was also confirmed with FTIR analysis. The FTIR spectra of chitosan, chitosan-PEG and chitosan-PEG-CREKA were recorded in the region of 650-4000 cm^{-1} with Thermo Scientific iS10 FTIR.

4.2.3. Synthesis of DNA loaded CREKA Modified Chitosan Nanoparticles

DNA loaded and CREKA Modified PEGylated Chitosan Nanoparticles (CS-PEG-CREKA NPs) were synthesized with ionotropic gelation method.[74] Lyophilized chitosan-PEG-CREKA conjugate was dissolved in 1 $mg \cdot mL^{-1}$ acetic acid (0.5 $mg \cdot mL^{-1}$ chitosan concentration). pH of solution was changed to 4.8 with 6 M NaOH. TPP was dissolved

(0.5 mg·mL^{-1}) in ultrapure water and pH of the solution was adjusted to 2.5 with 6 M HCl. Plasmid DNA solution was added to chitosan solution as 20:1 nitrogen to phosphate ratio. Chitosan-PEG-CREKA and TPP solutions were mixed at a chitosan to TPP ratio of 4:1 (v/v) and reactions proceeded for 45 minutes. Size and zeta potentials of DNA loaded CS-PEG-CREKA NPs was measured with dynamic light scattering (DLS) technique.

4.2.3.1. Encapsulation Efficiency

Encapsulation efficiency of DNA into nanoparticles was evaluated with NanoDrop Fluorospectrometer (Termo Scientific). DNA concentration nanoparticle solution was measured in NanoDrop. After that, nanoparticle solution was centrifuged at 20,000 rpm for 30 min, and DNA concentration of supernatant was measured. Ratio between these two concentration gave the encapsulation efficiency.

4.3. Results and Discussion

4.3.1. Synthesis of Chitosan-PEG-CREKA Conjugate

Chitosan-PEG-CREKA conjugate was synthesized using NHS-Amine and sulfhydryl-reactive chemistry. Namely, SVA end of PEG molecule reacted with amino groups of chitosan and Maleimide (MAL) end of PEG reacted with -SH groups of CREKA. Maleimide group is also reactive with amino group at pH 8. To prevent the formation of byproducts, pH of reaction was selected as 6 since reaction between -SH and MAL is dominant at that particular pH value. Illustration of conjugation process is shown in Figure 4.1.

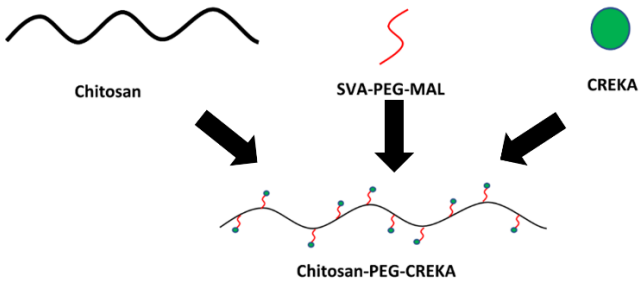

Figure 4.1. Synthesis of chitosan-PEG-CREKA conjugate

4.3.1.1. TNBS and Ellman's Assay

TNBS assay was performed for the synthesized conjugate. From TNBS assay, PEGylation degree was determined as 16.02%, in other words, 16.02% of amino groups on chitosan were conjugated with SVA groups of PEG.

Ellman's calibration curve was prepared using cysteine standarts. Calibration curve is presented in Figure 4.2.

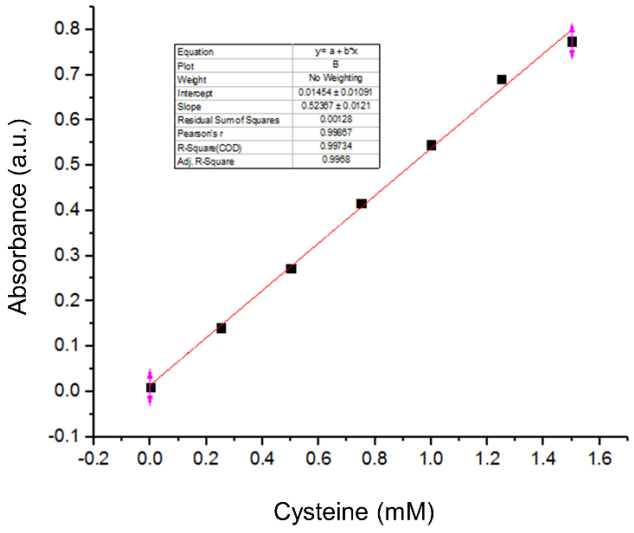

Figure 4.2. Calibration curve for Ellman's assay

Ellman's assay was performed for chitosan-PEG-CREKA, just after finishing the reaction (before dialysis). Ellman's assay has shown that resulting reaction mixture has 0.0239 mM -SH groups. For the conjugation reaction, 20 mg or 1.32 mM CREKA was used. This showed that approximately 98% of -SH molecules were consumed during the reaction. This is a strong evidence for conjugation of -SH molecules to the MAL end of PEG.

4.3.1.2. Peptide Quantification with Pierce™ BCA Protein Assay Kit

After dialysis and freeze drying, peptide amount in the conjugate was determined with BCA protein assay kit. BCA standard calibration curve is presented in Figure 4.3.

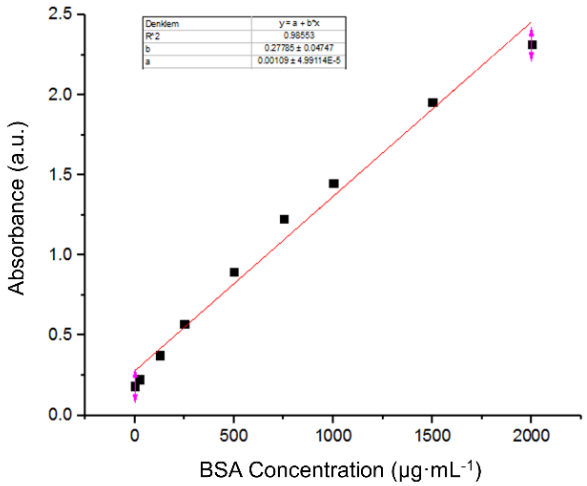

Figure 4.3. BCA standard calibration curve

Assay has shown that peptide concentration was 75.9 µg·mL^{-1} in 1000 µg·mL^{-1} conjugate concentration. This showed that the polymer conjugate had peptide inside. Considering most of the peptides went to DI water phase during the dialysis, this was also a strong evidence for conjugation of peptide.

4.3.1.3 FT-IR Analysis

FT-IR analysis was performed for chitosan, chitosan-PEG and chitosan-PEG-CREKA samples. FT-IR spectrum of chitosan-PEG-CREKA conjugate is shown in Figure 4.4.

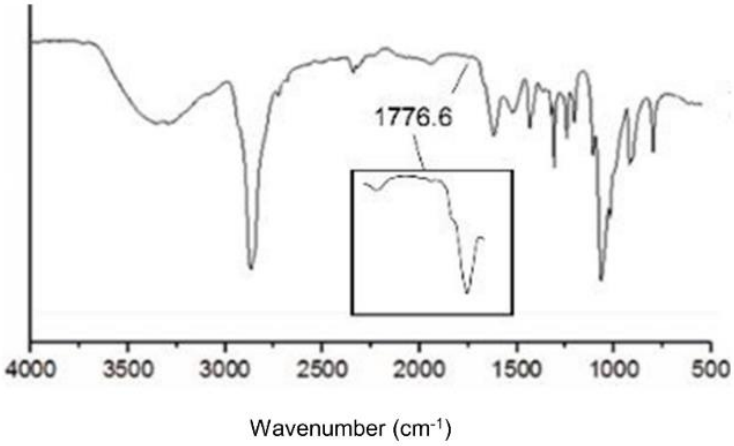

Figure 4.4. FT-IR spectrum of chitosan-PEG-CREKA

In FT-IR spectrum, amide bond formation was observed around 1560 cm^{-1} which is a evidence for PEGylation. Thioester bond gives a band around 1281 cm^{-1}, however, we could not observe this band since it may have overlapped with other peaks in the spectrum. However, C=O band in maleimide group was observed around 1770 cm^{-1}. Also, new conjugate retained -OH and N-H bands around 3000-3500 and 1580 cm^{-1}. These results suggested that CREKA was chemically bound.

4.3.2. Synthesis of CREKA Modified PEGylated Chitosan Nanoparticles

Nanoparticles were synthesized using the new CS-PEG-CREKA conjugate. Interaction between positively charged and CS-PEG-CREKA and negatively charged TPP resulted in electrostatically crosslinked nanoparticles in the presence of plasmid DNA. DLS results (Fig. 4.5). showed that particles were monodisperse and had z-average size around 76.88 nm (at pH 4.7).

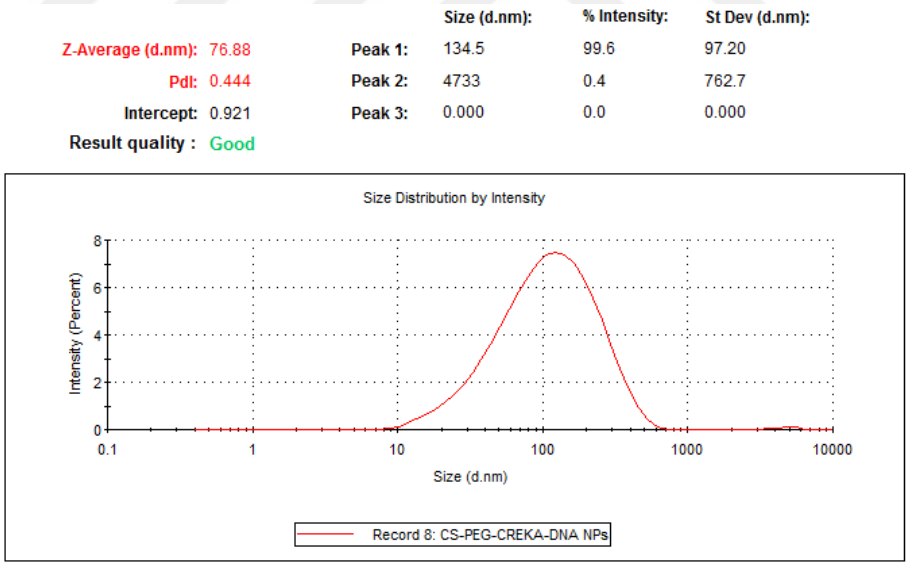

Figure 4.5. Size distribution of DNA loaded CS-PEG-CREKA NPs

Also, the new nanoparticles have highly positive charge as expected in pH 4.7 (Fig. 4.6)

		Mean (mV)	Area (%)	St Dev (mV)
Zeta Potential (mV): 29.7	Peak 1:	29.7	100.0	3.61
Zeta Deviation (mV): 3.36	Peak 2:	0.00	0.0	0.00
Conductivity (mS/cm): 0.744	Peak 3:	0.00	0.0	0.00

Result quality : Good

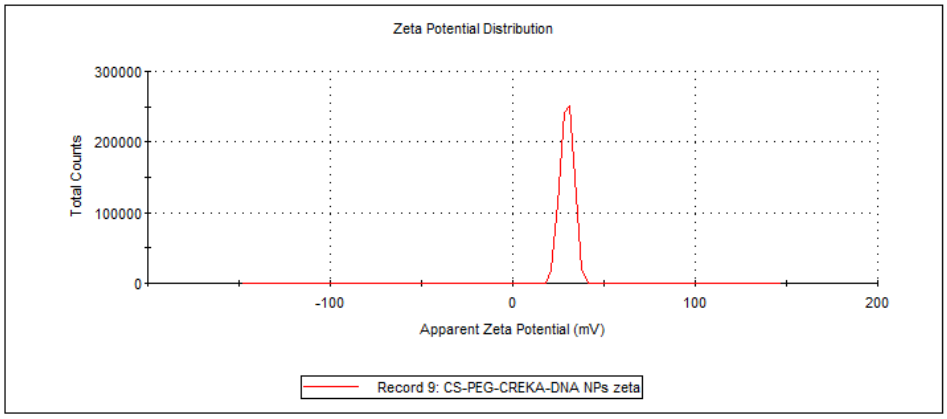

Figure 4.6. Zeta potential of DNA loaded CS-PEG-CREKA NPs

To see the effect of CREKA, we also synthesized DNA loaded nanoparticles with PEGylated chitosan with 5 kDa under experimental same conditions. DLS results showed that DNA loaded PEGylated chitosan nanoparticles had smaller size (Figure 4.7). We deduced that CREKA conjugation increases the size of the nanoparticles.

		Size (d.nm):	% Intensity:	St Dev (d.nm):
Z-Average (d.nm): 60.05	Peak 1:	94.32	99.0	75.01
PdI: 0.322	Peak 2:	4242	1.0	1006
Intercept: 0.946	Peak 3:	0.000	0.0	0.000

Result quality : Good

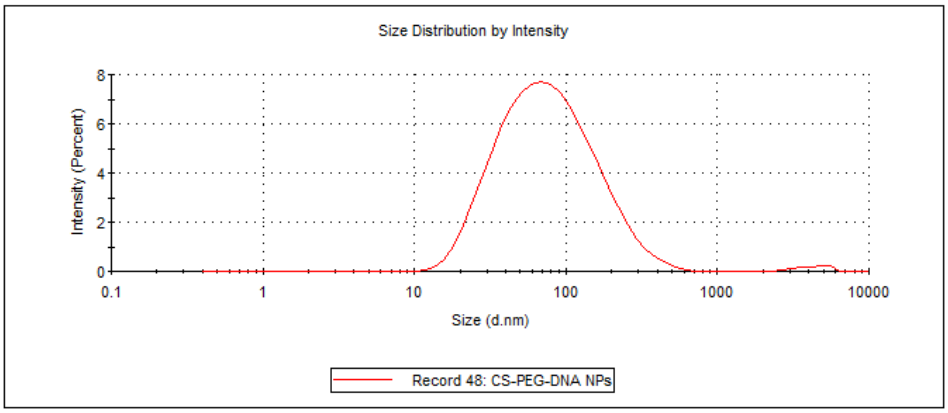

Figure 4.7. Size distribution of PEGylated chitosan nanoparticles

Also, DNA loaded and PEGylated chitosan nanoparticles had much smaller zeta potential compared to CS-PEG-CREKA NPs at same pH (Figure 4.8). Higher zeta potential of CS-PEG-CREKA NPs was probably due to positive charges of amino acids in CREKA peptide in pH 4.7. Since side groups were positively charged, they increased the surface charge of nanoparticles.

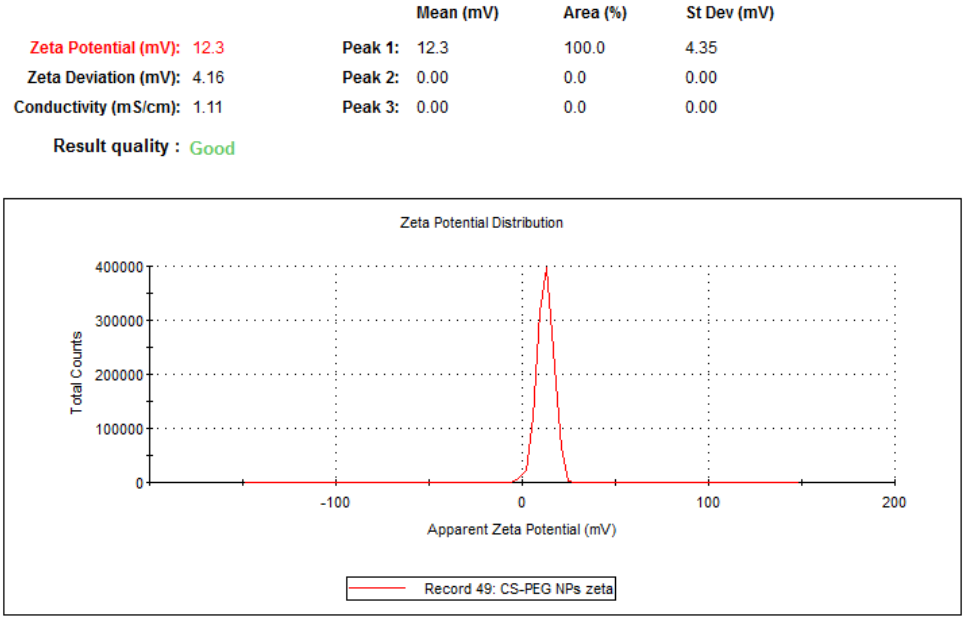

Figure 4.8. Zeta potential of DNA loaded PEGylated chitosan nanoparticles

Encapsulation efficiency experiments for CS-PEG-CREKA NPs demonstrated that approximately 80% included DNA was encapsulated into the nanoparticles.

4.4. Conclusions and Future Work

DNA loaded and CREKA modified chitosan nanoparticles was successfully synthesized. As a future work, transfection efficiency of different nanoparticles will be tested on various cancerous cell lines. As mentioned in introduction part, plasmid DNA that was encapsulated contains TRAIL code. TRAIL protein kills the cancerous cell lines; thus, these chitosan nanoparticles are promising for treatment of cancer related diseases

CHAPTER 5

Light-Triggered Drug Release from 3D-Printed Magnetic Chitosan Microswimmers

5.1. Introduction

Magnetic microswimmers have great potential in biomedical applications due to their wireless actuation and precise localization capabilities.[45, 97] Their micron size and wireless control can allow deep tissue penetration, and could open a new era for minimally invasive therapies.[47] Thus far, synthetic and biohybrid magnetic microswimmers have been used in different applications such as targeted cargo delivery, cell manipulation and tissue engineering.[98-106]

The advancements in two-photon polymerization technique realized fabrication of more complex 3D structures at micron scale and eased local 3D micropatterning of these structures using versatile chemical moieties.[54-55, 57-58] Fabrication and design of complex structured micron scale materials are challenging with conventional microfabrication techniques, in fact, only simple geometric structures can be fabricated with limited design. To overcome these problems, utilizing computer aided designs combined with two-photon direct laser writing (TDLW) is a recently emerging technology and this technology allows printing of complicated structures up to 100 nm resolution by using photosensitive materials [54, 107-108]. Interaction between focused femtosecond laser and photosensitive materials results in radical monomers and finally covalently crosslinked structures in computer-controlled trajectories [58, 107-108]. Having photosensitive materials is the key factor for TDLW, however, only few materials have photosensitive characteristics. Yet, polymers like chitosan that do not have photosensitive characteristics can be modified from their monomers by introducing photosensitive groups while polysaccharide backbone remains unchanged.

Triggered systems are attractive for facilitating release of therapeutics to desired sites at desired times. Thus, concentration of therapeutic agents on desired sites can be increased, and overall injected dose can be decreased. Light-triggered release systems are particularly attractive among the other trigger mechanisms such as pH and temperature due to their high spatiotemporal accuracies.[109] In ultraviolet (UV) light-triggered release

systems, low tissue penetration depth of the UV light severely limits the potential biomedical applications. However, optical upconversion processes can be solution in more realistic real-life applications of UV triggered systems. In upconversion processes, low energy photons (e.g. NIR) are transformed to high-energy photons, an (*e.g.*, UV light) and enhanced penetration depth can be obtained.[110]

Here, we developed biodegradable chitosan-based microrobotic system for light-triggered drug release. The microswimmers had 6 μm diameter and 20 and were fabricated from photocrosslinkable methacrylamide chitosan with photoinitiator and SPIONs. The microswimmers were driven in an aqueous environment, average speed of microswimmers was 3.34 ± 0.71 μm·s^{-1} under a 10 mT and 4.5 Hz rotating magnetic field. Azide-modified doxorubicin (DOX) was selected as a model drug for light-triggered drug release. DOX was bound to alkyne groups of the microswimmers after conjugating the *o*-nitrobenzyl linker to microswimmers through NHS-Amine reaction. Also, biodegradability of the chitosan microswimmers was shown at 37 °C with various lysozyme concentrations. Overall, we designed a biocompatible and biodegradable magnetic chitosan microswimmer system with a controlled drug release mechanism. This system decreases the side effects of the therapeutic system due to precise drug localization capability and further increase therapeutic index of the system.

5.2. Experimental

5.2.1. Materials

All materials were purchased from Sigma-Aldrich unless otherwise specified.

5.2.2. Synthesis of Methacrylamide Chitosan

Methacrylamide chitosan (ChMA) was synthesized according to previously described protocol with some modifications.[111] 3% (w/v) low molecular weight chitosan was dissolved in 3% (v/v) acetic acid solution, and then stirred at room temperature (RT) for 24 h. Methacrylic anhydride (MA) was added to that solution at 3.5:1 (ChMA:MA) ratio to obtain ~70% methacrylation degree. The reaction was performed for 3 h with vortex mixer at RT. Reaction medium was diluted with distilled water and dialyzed (14

kDa cut-off) against distilled water for 4 d. Distilled water was changed three times per day. The resulting solution was lyophilized, ChMA flakes were stored at -20°C for further use.

5.2.3. Degree of Methacrylation Characterization

Degree of methacrylation of ChMA macromolecules was determined with 2,4,6-Trinitrobenzene Sulfonic Acid (TNBS) assay. As it was mentioned in previous chapters, TNBS assay quantifies amino groups, and degree of methacrylation was determined based on the quantification of unmodified free amino groups. Briefly, unmodified chitosan, as a control group, and 0.05% (w/v) ChMA macromolecules were dissolved in 0.2% (v/v) acetic acid solution. 80 µL of the solutions were incubated with 40 µL of 2% (w/v) $NaHCO_3$ and 60 µL of 0.1% (v/v) TNBS reagent (Thermo Fisher Scientific) at 37°C for 2 h. After the incubation period, 60 µL of 1 N HCl was added into the solutions to terminate reaction, and then absorbance of the samples was measured at 345 nm using a plate reader (BioTek Gen5 Synergy 2, Bad Friedrichshall, Germany). Degree of methacrylation was calculated according to the following equation:

$$\text{Degree of Methacrylation \%} = 100 - \frac{\text{Absorbance of Sample}}{\text{Absorbance of Unmodified Chitosan}} \times 100 \quad (1)$$

5.2.4. 3D Printing of the Microswimmers

ChMA (30 $mg \cdot mL^{-1}$), phenyl-2,4,6-trimethylbenzoylphosphinate (LAP) photoinitiator (20 $mg \cdot mL^{-1}$) (Tokyo Chemical Industry Co. Ltd.) and superparamagnetic iron oxide nanoparticles (5 $mg \cdot mL^{-1}$) (50 nm fluidMAG-PEG/Amine from Chemicell GmbH) were dissolved in 8% (v/v) acetic acid solution. Polymer solution was heated and stirred for at least 2 hours until obtaining clear solution. The resulting polymer solution was dropped on a trichloro(1H,1H,2H,2H-perfluorooctyl)silane treated glass slide. This treatment enabled us to detach microswimmers from the surface. Microprinting was performed with a commercially available direct laser writing system (Photonic Professional, Nanoscribe GmbH). After the fabrication of microswimmers, glass slides were washed with distilled water. Clean glass slides were kept at 4°C in fridge for further use.

5.2.5. Enzymatic Degradation of Microswimmers

3D printed microswimmers were treated lysozyme solutions with various concentrations (1.5, 15 and 150 $\mu g \cdot mL^{-1}$) in phosphate buffered saline, at 37°C. The length and diameter of the microswimmers were measured in different time periods using Nikon Eclipse Ti-E inverted microscope with 20x magnification in DIC mode. Enzyme solutions were changed every 12 h.

5.2.6. Photocleavable Linker and Drug Binding on Microswimmers

As a first step, *o*-nitrobenzyl linker was chemically conjugated to fabricated swimmers through NHS-Amine coupling. 500 μM of *o*-nitrobenzyl linker was dissolved in anhydrous dimethyl sulfoxide, and microswimmer containing glass slides were treated with this solution for 4 hours at RT. To couple azide-DOX to alkyne end of the linker molecules on microswimmers, previously described protocol was adapted with some modifications.[112] Microswimmer containing glass slides were treated with solution containing 50 μM azide-DOX, 100 μM $CuSO_4$, 5 mM sodium ascorbate, 500 μM Tris(3-hydroxypropyltriazolylmethyl)amine for 3 hours at RT. At the end, glass slides were washed with distilled water, and kept in dark conditions to prevent photobleaching of DOX.

5.2.7. Light-Triggered Drug Release from the Microswimmers

The main assumption for the drug release experiments was that the initial fluorescence intensity of the microswimmers was equal to 100% drug loading to the microswimmers. Thus, the drug release from the microswimmers was analyzed based on the fluorescence intensity decrease. Before drug release experiments, fluorescence bleaching of microswimmers was analyzed performed to confirm that there was no photobleaching- and diffusion-related fluorescence intensity changes in the microswimmers. Accordingly, microswimmers were exposed to 365nm or 470 nm, and fluorescent images were obtained every 10 s. Tests were performed for both 3 and 30 mW and lasted for 30 min. Fluorescence intensities were analyzed with LASX analysis toolbox (Leica Microsystems).

Light-triggered drug release from the microswimmers was investigated using fluorescence inverted microscope with light exposure at 365 nm (DMi8, Leica Microsystems). Fluorescent images of microswimmers were obtained every 10 s for 30 min. Light output power was selected as either 3 mW or 30 mW. Light exposure time was chosen as 1 s. Drug release or decrease in fluorescence intensities of the microswimmers were measured with LASX analysis toolbox (Leica Microsystems). For on-demand light-triggered drug release experiment, 1 min of light exposure was followed by 5 min blank period. For all experiments, background fluorescence was subtracted.

5.3. Results and Discussion

5.3.1. Synthesis of Methacrylamide Chitosan

Photosensitive form of chitosan, methacrylamide chitosan (ChMA), was synthesized by reaction between amino groups of the polymer with methacrylic anhydride.[111] Some of the amino groups of the chitosan were converted to photosensitive methacrylamide groups.[113] New polymer chains had crosslinking ability with photoinitator around 365 nm wavelength UV light. Degree of methacrylation of ChMA polymers was determined with TNBS assay. Reaction time was kept constant and methacrylic anhydride/chitosan ratio was changed (Fig. 5.1).

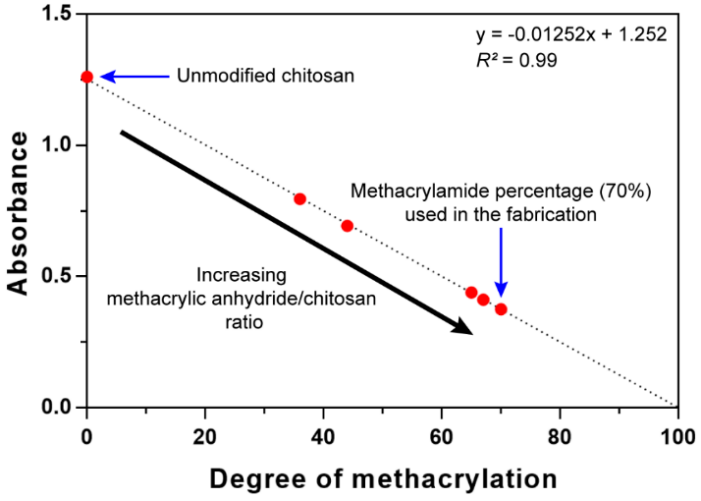

Figure 5.1. TNBS assay results. Unmodified chitosan gives the highest amino group absorbance at 345 nm. Amino groups absorbance decreases since amino groups are consumed after reaction.

The assay has shown that number of amino groups decreased with increasing methacrylic anhydride/chitosan ratio. ChMA with 70% methacrylation degree was selected for 3D printing since it was easier to print and had higher solubility.

5.3.2. 3D Printing of the Microswimmers

Methacrylamide chitosan (Fig 5.2A) was used to fabricate chitosan-based microswimmers with double helices geometry. Prepolymer solution had 30 $mg \cdot mL^{-1}$ ChMA, 20 $mg \cdot mL^{-1}$ LAP and 5 $mg \cdot mL^{-1}$ PEG/Amine-functionalized 50 nm SPIONs (Fig. 5.2B). Embedded SPIONs enabled control and steering of the microswimmers in 3D aqueous environments using rotating magnetic fields. In addition, usage of SPIONs in microswimmer designs has two main advantages: (1) they are often considered to be biocompatible and have no severe side effects *in vivo*,[114] and (2) they dramatically increase the availability of drug and cargo release sites compared to cobalt- or nickel-based surface coatings.

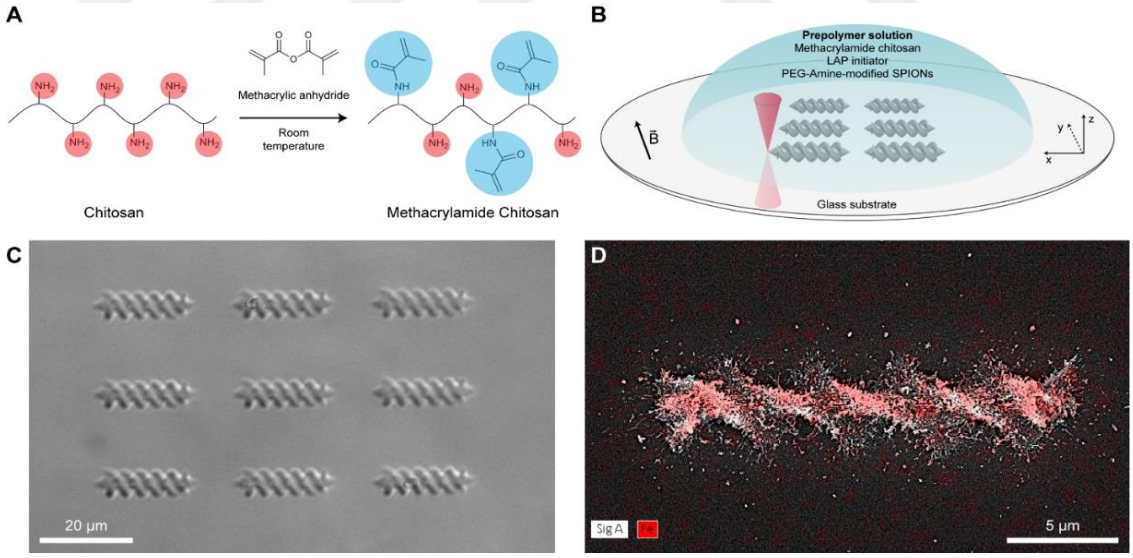

Figure 5.2. Overview of the synthesis and fabrication processes**. A)** Synthesis of the photocrosslinkable methacrylamide chitosan from natural chitosan. **B)** 3D printing of the microswimmers using two-photon direct laser writing technique. **C)** Optical microscopy image of 3D printed 3x3 array of the microswimmers. **D)** Energy-dispersive x-ray spectroscopy elemental mapping shows the presence of iron atoms (red color) in the microswimmers.

A single microswimmer had 20 μm length and 6 μm outer diameter (Fig. 5.2C). Average printing rate was around 10 seconds for an individual microswimmer. Energy-dispersive x-ray spectroscopy (EDS) elemental mapping confirmed homogenous dispersion of iron atoms in the microswimmers (Fig. 5.2D). The 3D structure of the microswimmers affected during the EDS elemental mapping due to the applied energy (15 keV) and accusation time (10 min).

5.3.3. Magnetic Actuation and Control of the Microswimmers

The microswimmers were actuated and steered using a five-coiled electromagnetic setup, which can be mounted on an inverted optical microscope. The experiments were performed using a 10 mT rotating magnetic field. Initially, step-out frequency of the microswimmers was investigated by gradually increasing the frequency of the applied rotating magnetic field from 1 Hz to 6 Hz with 0.5 Hz steps. It was demonstrated that the fabricated microswimmers were actuated and steered optimally at 4.5 Hz under a 10 mT rotating magnetic field (Fig. 5.3A). The average forward velocity of the microswimmers at optimum actuation frequency was measured to be 3.34 ± 0.71 $\mu m \cdot sec^{-1}$. Finally, the microswimmers were steered in different paths to demonstrate the controllability of the microsystem, and it was shown that it is possible to drive the microswimmers at both 4.5 Hz and 5 Hz under a 10 mT rotating magnetic field (Fig. 5.3, Fig. 5.4)

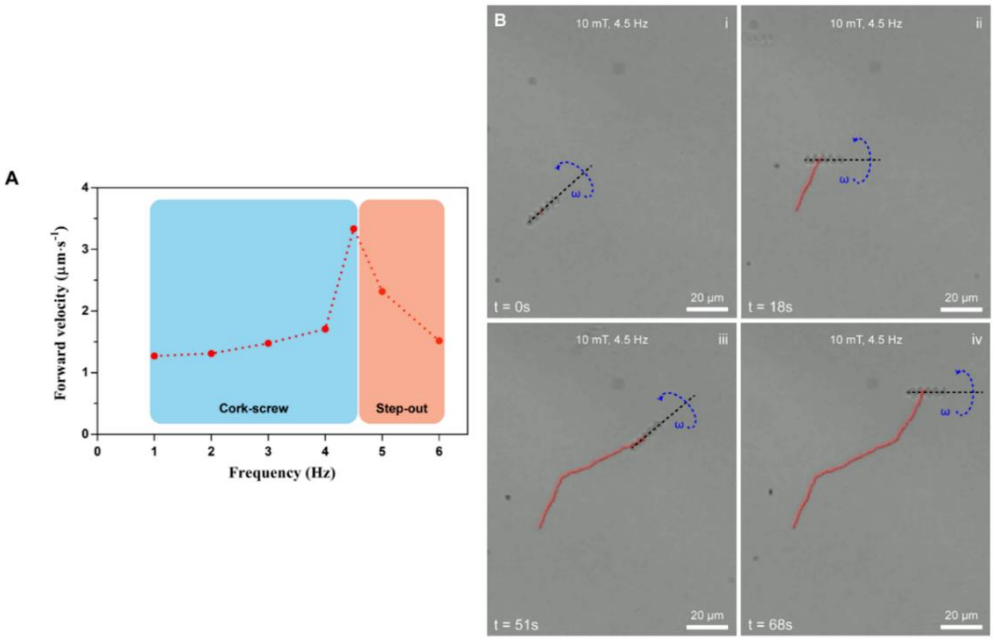

Figure 5.3. Actuation and steering of the microswimmers using a rotating magnetic field. A) Forward velocity of the microswimmers as a function of magnetic excitation frequency demonstrates a step-out frequency of 4.5 Hz. B) Controlled swimming trajectory snapshots (red lines) of the microswimmers under a 10 mT rotating magnetic field at 4.5 Hz.

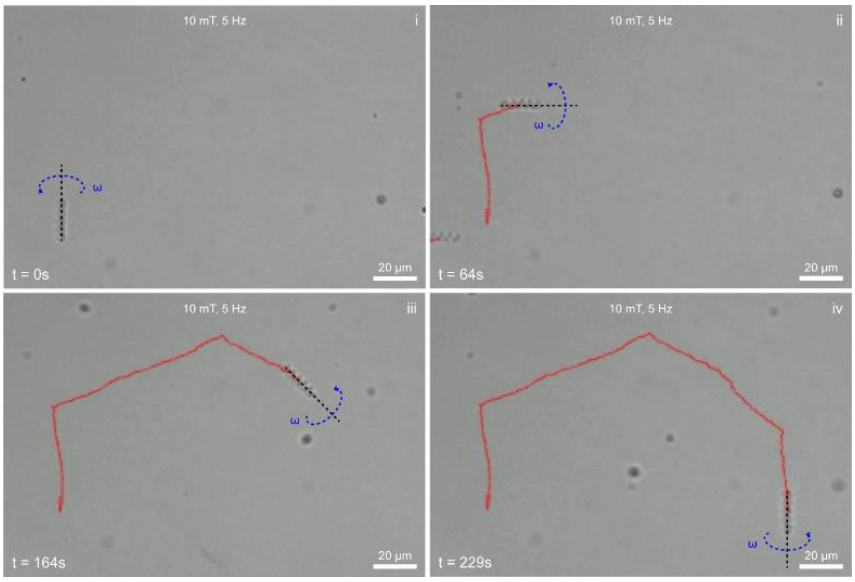

Figure 5.4. Controlled swimming trajectory of the microswimmers at 5 Hz under a 10 mT rotating magnetic field.

5.3.4. Enzymatic Degradation of Microswimmers

Biodegradable materials have gained attention in biomedical engineering applications since they are able to break down and disappear from the body.[115] Chitosan is mainly degraded by lysozyme enzyme, which presents in various tissues and body fluids with a range of approximately 1-15 $\mu g \cdot mL^{-1}$ concentrations.[116-118] Lysozyme enzyme breaks the glycosidic bonds between the chitosan monomers, and the small chains are removed naturally from the human body.[119] Here, we used three different lysozyme enzyme concentrations (1.5, 15 and 150 $\mu g \cdot mL^{-1}$) for biodegradation of the chitosan microswimmers, where 150 $\mu g \cdot mL^{-1}$ represented an unrealistically high condition. Biodegradation of the microswimmers with 15 $\mu g \cdot mL^{-1}$ lysozyme concentration was shown in Figure 5.5A. Biodegradation of the microswimmers occurred by surface erosion mechanism. In surface erosion mechanism, water and enzymes could not penetrate inside the crosslinked structures, and thus, degradation was started from the exterior surface of microswimmers.[120] Helices and sharp edges of the chitosan microswimmers were degraded first. For all enzyme concentrations, the microswimmers were partially degraded after 204 hours. Unrealistically high lysozyme enzyme concentration group (150 $\mu g \cdot mL^{-1}$) had the lowest diameter and length while 1.5 $\mu g \cdot mL^{-1}$ lysozyme concentration group had the highest after 204 hours (Fig. 5.5B, C).

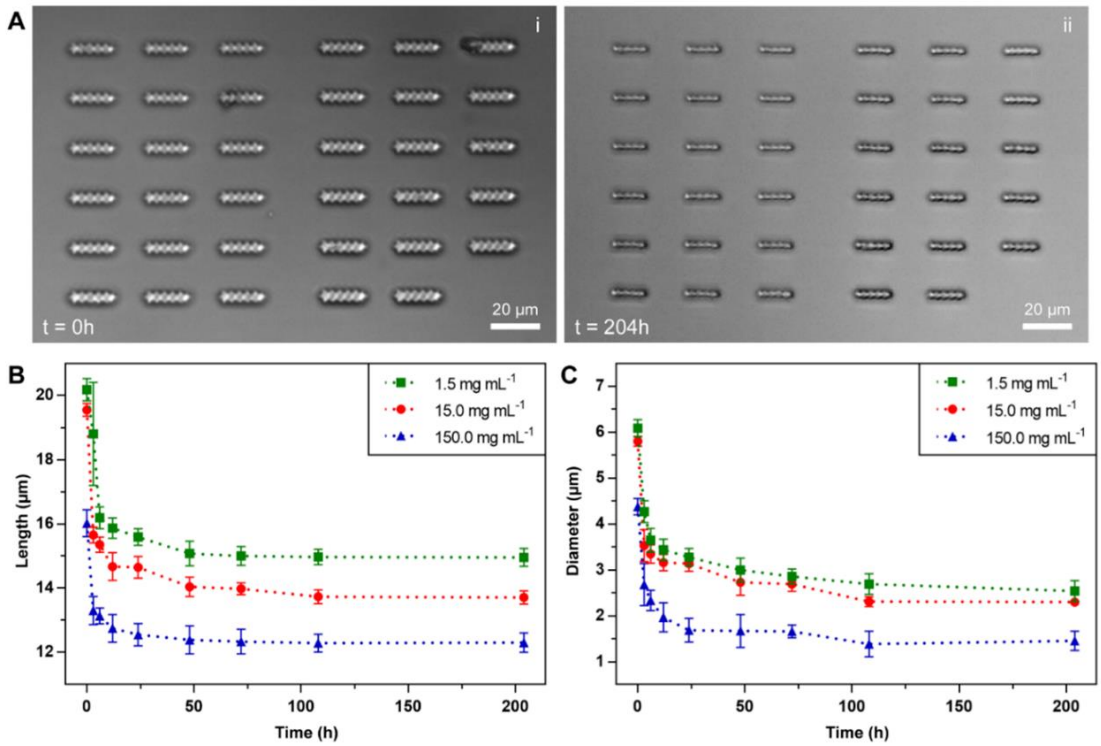

Figure 5.5. Enzymatic degradation of the microswimmers using lysozyme. **A)** Optical microscopy images of the microswimmers treated with 15 µg·mL^{-1} lysozyme, **i.** t = 0 h and **ii.** t = 204 h reveal a surface corrosion-based degradation mechanism. **B)** Changes in length of the microswimmers in time with different lysozyme concentrations. **C)** Changes in diameter of the microswimmers in time with different lysozyme concentrations.

There was rapid diameter and length changes in all groups due to the surface erosion. After biodegradation of the helices and the edges, the rate of diameter and length changes dramatically decreased as expected since helices and the edges had much smaller volume compared to whole body of the microswimmers. It did not mean decrease in the degradation rate, because lysozyme enzyme then started to degrade cylindrical microswimmer body which had lower surface area to volume ratio. Because of this phenomenon, it became harder to observe length and diameter changes after some point. Partial degradation of the microswimmers in 204 hours was consistent with the literature findings, where full degradation was not observed after several weeks for most of the studies.[121-124]

5.3.5. Photocleavable Linker and Drug Binding to the Microswimmers

Photocleavage-based light-triggered delivery systems have been studied to regulate the release rates of various molecules. In photocleavage-based systems, molecules are chemically bound to photocleavable linkers. The photocleavable linker molecules divide into two part upon light radiation and then molecules are released.[110] Functional *o*-nitrobenzyl derivatives have been used for delivery of different molecules.[125-126] N-Hydroxysuccinimide ester (NHS) and alkyne modified o-nitrobenzyl derivative is effective for the release of molecules owing to its chemical functionality.[126] NHS functional group selectively reacts with amino groups and alkyne group react with azide groups (known as copper (I) catalyzed Click reaction). We conjugated NHS end of photocleavable linker molecules to free amino groups of the chitosan microswimmers. After that, we conjugated azide-modified DOX to the alkyne ends of photocleavable linker molecules (Fig. 5.6A). For the first reaction, the microswimmers were treated with the *o*-nitrobenzyl photocleavable linker molecules containing solution. Alkyne-ended microswimmers were obtained after this reaction. For the second reaction, alkyne ended microswimmers were treated with azide-DOX containing solution. With a different group of microswimmers (negative control group), only the second step was performed. Azide-modified DOX could not be bound to the microswimmers in the negative control since there was no reaction between amino and azide groups. To confirm DOX was chemically bound to DOX modified group, it was compared with the negative control group using fluorescence microscopy. DOX-modified group had significantly higher fluorescence emission than the negative group at same exposure intensity and time (Fig. 5.6B, C). Fluorescence microscopy experiments confirmed the chemical conjugation of *o*-nitrobenzyl linker and azide-modified DOX to the microswimmers. Negative group also gave slight fluorescence, which was caused by simple diffusion of DOX molecules.

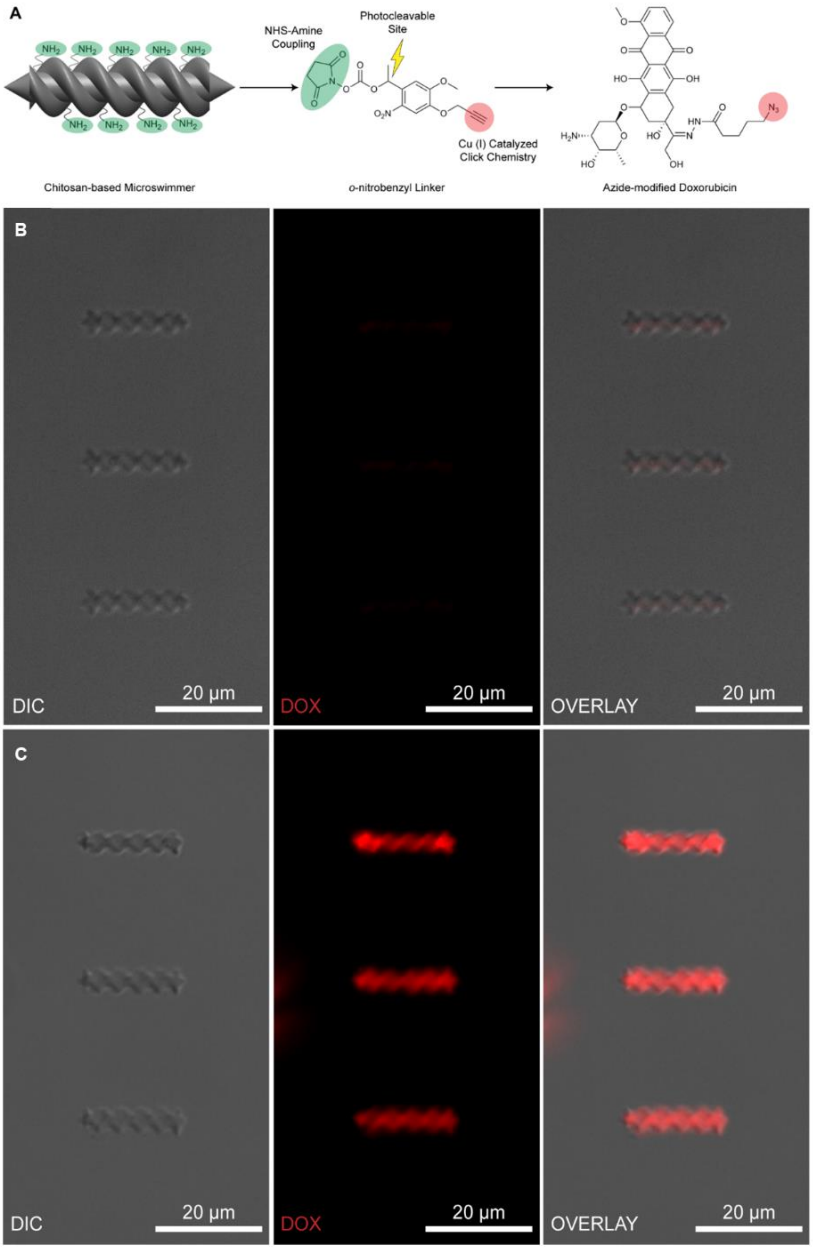

Figure 5.6. Drug binding on microswimmers. A) Schematic shows the reaction pathway to obtain DOX-modified microswimmers. Amino groups on the microswimmers react with NHS group of o-nitrobenzyl photocleavable linker molecules. Then, azide-modified DOX reacts with alkyne ends of the microswimmers. B) Microswimmers without the o-nitrobenzyl linker modification were directly treated with the drug molecules (azide-DOX). C) Microswimmers with the o-nitrobenzyl linker modification were treated with the drug molecules (azide-DOX). Images were captured with the same fluorescence intensity and exposure time, and represent the controlled integration of azide-DOX onto the microswimmers.

5.3.6. Light-Triggered Drug Release From the Microswimmers

Light-triggered drug release experiments was performed with 365 nm wavelength. The main assumption for the drug release experiments was that the initial fluorescence intensity of the microswimmers corresponds to 100% drug loading in the microswimmers. Decrease in fluorescence intensity upon light radiation was attributed to drug release from microswimmers. Bleaching tests were performed to confirm there was no photobleaching or diffusion related intensity change. The negative group were exposed to light at 365 and 470 nm, which was used for o-nitrobenzyl cleavage and DOX excitation respectively. The results showed that fluoresence intensity did not change with 365 and 470 wavelength (Fig. 5.7). Fluorescence decrease was not observed for 470 nm (Fig. 5.7A) and 365 nm for two laser output power (3, 30 mW, Figure 5.7B, C). These results suggested that decrease in fluorescence intensity upon light exposure was due to light-triggered drug release.

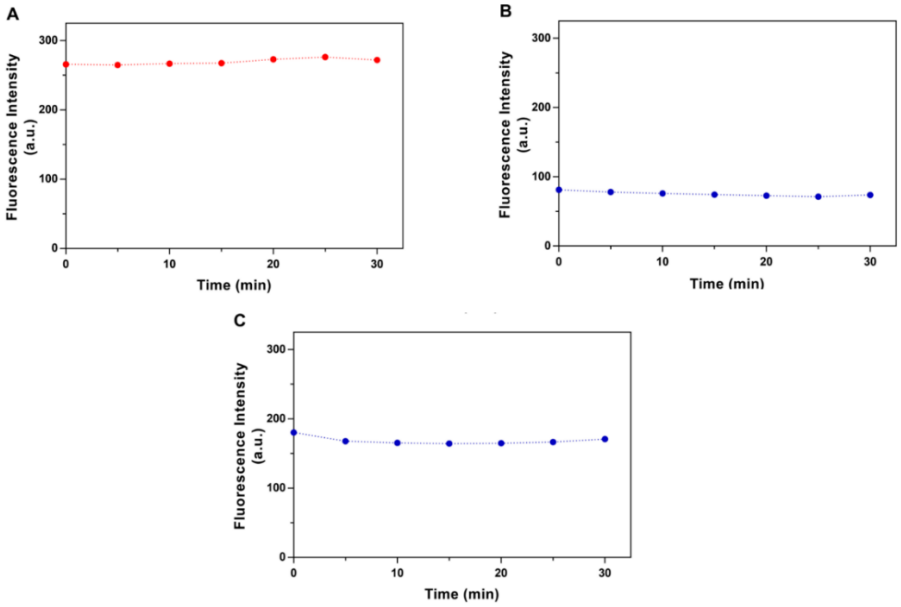

Figure 5.7. Photobleaching tests for the drug molecules prior to controlled release experiments. A) 470 nm wavelength light excitation for 30 min to negative group (microswimmers without the *o*-nitrobenzyl linker modification) **B)** 3 mW 365 nm wavelength light exposure for 30 min to negative group. **C)** 30 mW 365 nm wavelength light exposure for 30 min to negative group.

3 and 30 mW laser output powers were selected for 365 nm wavelength to demonstrate light-triggered drug release. For 30 mW, there was remarkable fluorescence intensity decrease in microswimmers after 30 min which means that DOX was released from the microswimmers (Fig. 5.8A). 60% of the bound DOX was released within 5 min for 30 mW light intensity (Fig. 5.8B). The release rate dramatically decreased after 5 min. The incomplete release is due to low photochemical conversion observed for nitrobenzyl groups.[127] Slow release after 5 min was observed due to slower diffusion of DOX molecules which were cleaved-off from inside of the chitosan microswimmers. As expected, slower drug release was observed for 3 mW light intensity compared to 30 mW light intensity. Drug release rate decreased and converged approximately to 40% (Fig. 5.8B). Lower drug release rate is probably due to slower reaction kinetics due to the lower light intensity.[127]

Smart dosing of therapeutics has gained considerable attention since many drugs have serious off-target side effects.[128] Accordingly, we showed drug can be released from swimmers on-demand by switching the light on and off. Light at 365 nm wavelength was turned on for 1 min and then turned off for 5 min, and this was repeated for twice. A clear drug release from the microswimmers was observed when light was on (30 mW light intensity) for 1 min, and there was almost no drug release from the microswimmers when the UV light was off for 5 min (Fig. 5.8C). Approximately 15% of the total drug was released per 1 min and this showed that the user can control on-demand drug release profile from the chitosan microswimmers.

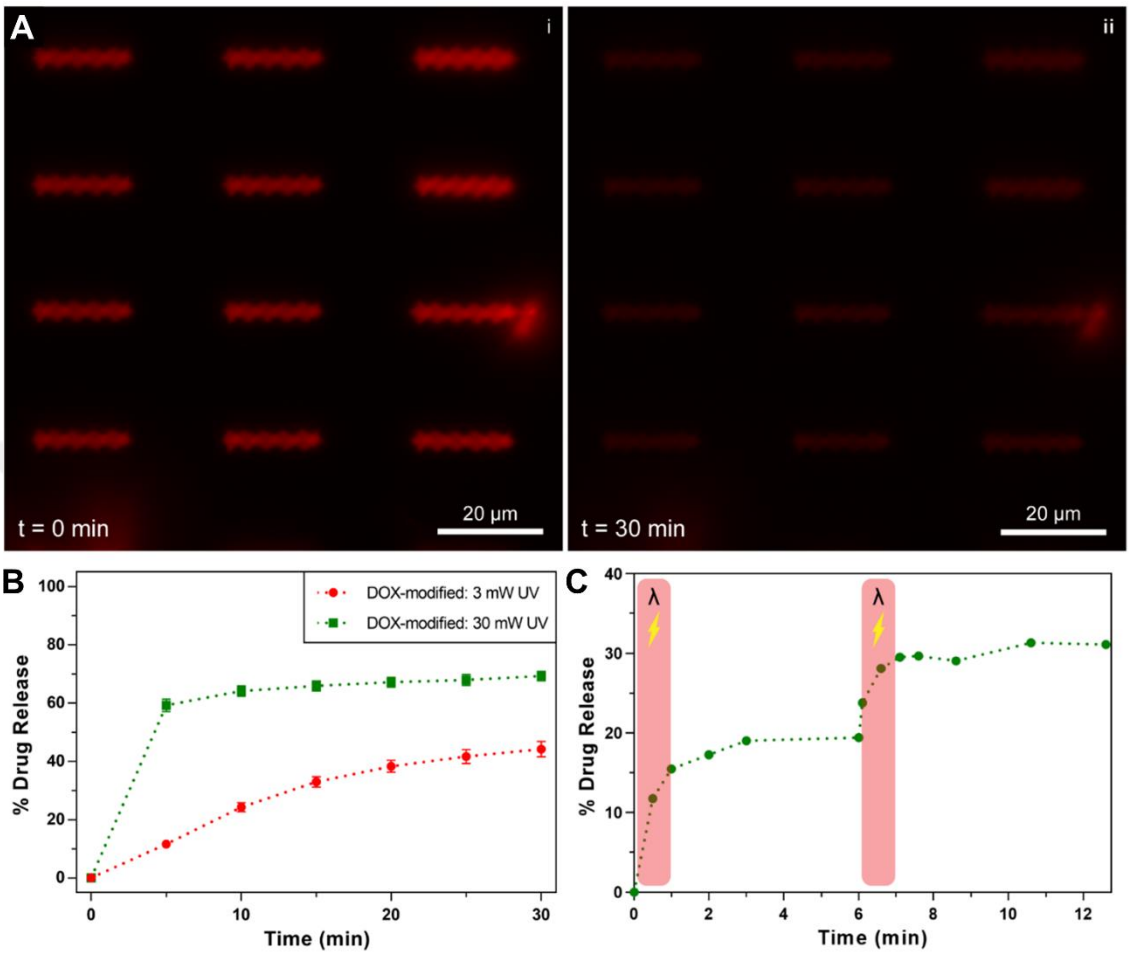

Figure 5.8. Light-triggered drug release from the microswimmers. A) DOX release from the microswimmers exposed to 30 mW light intensity for 30 min. Decrease in the fluorescence intensity indicates the cleavage of DOX from the microswimmers and its release. B) Cumulative DOX release from the microswimmers for 3 mW and 30 mW light intensity. C) Smart dosing of DOX from the microswimmers. 365 nm wavelength light is on in the red regions. Roughly, 15% of DOX was released per minute from the microswimmers.

It was also shown that the drug release can be localized by focusing the light on specific group of microswimmers. Drug was released from specific group of the microswimmers while others kept the drug inside (Fig. 5.9A). Moreover, it was also demonstrated that the drug could be released from half body of the microswimmers (Fig. 5.9B). Overall, it was shown that *o*-nitrobenzyl group is an efficient photocleavable linker molecule for the release of drug molecules from the microswimmers. Drug dose can also be controlled by changing the light parameters.

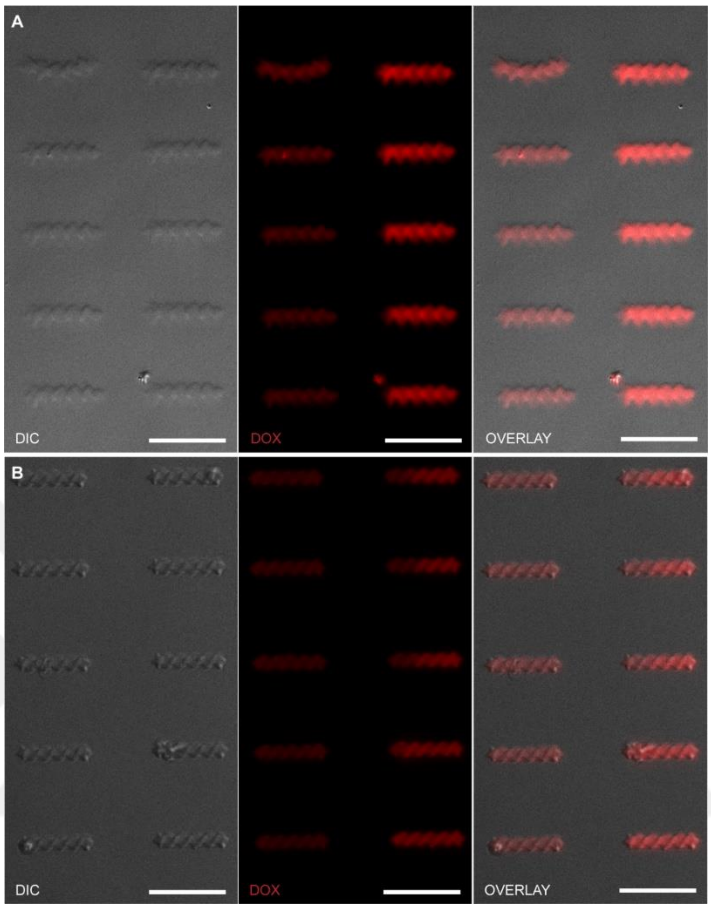

Figure 5.9. Controlled and localized drug release from chitosan-based microswimmers. A) UV exposure was focused onto the microswimmers found in left column. Drug molecules were controlled released upon UV exposure while the other group, found in right column, still had the integrated drug molecules. B) Precise drug release from half of the microswimmers body. Scale bars are 20 microns.

5.4. Conclusions

In summary, we developed microrobotic light-triggered drug delivery system from a biocompatible and biodegradable material. We synthesized photosensitive version of chitosan, chitosan methacrylamide, and fabricated microrobots from this new material with TDLW in the dimensions of 20 µm length and 6 µm outer diameter. We demonstrated controlled moving ability of microrobots. We present the combination of light-triggered drug delivery with microrobotic mobility for the first time. According to our knowledge, this system is promising for the challenges associated with delivery of therapeutics for the treatment of various diseases.

CHAPTER 6

Conclusions and Future Work

Biomaterial-based drug delivery systems has gained huge attention in treatment of various diseases. Such that, some of them were commercialized and saved thousand of people's lives. Unique properties of biomaterials could help to cure some other diseases. There is an urgent need to design of smart and functional materials that can be targeted to diseased cells. Also, availability and feasibility of the the base material is an important consideration for further commercialization of these systems. Undoubfully, chitosan is a promising material for biomedical engineering applications due to its unique properties. In this thesis, synthesis of colloidally stable chitosan nanoparticles were developed, and dynamics of the systems were investigated in detail for the first time. Studies about PEGylated chitosan nanoparticles are limited, but these nanoparticles can be used as therapeutic carriers in the future. Highly reproducible nature of the system will enable people to perform *in vivo*, and hopefully clinical stage experiments in the future. In parallel with, plasmid DNA loaded and tumor homing peptide modified chitosan nanoparticles were developed in the second part of the thesis. Cell culture studies will be performed with these nanoparticles to assess therapeutic efficiency of the system in the future.

In the last chapter of the thesis, it was shown that chitosan was a suitable material for microrobotic drug delivery applications. Chitosan-based microswimmers were able to swim in aqueous media in fully controllable manner. The microswimmers also had light-triggered drug release capability, which is desirable for localization of chemotherapeutics at desired sites. With the development of microrobotic systems as in this study, realization of Paul Ehrlich's "magic bullet" concept will be possible in the future. However, studies about cell-microrobot interactions and therapeutic efficiency of the systems must be thoroughly examined through *in vitro* and *in vivo* experiments.

BIBLIOGRAPHY

1. Rinaudo, M., Chitin and Chitosan: Properties and Applications. *Prog. Polym. Sci.* **2006,** *31* (7), 603-632.
2. Ariful Islam, M.; Park, T.-E.; Reesor, E.; Cherukula, K.; Hasan, A.; Firdous, J.; Singh, B.; Kang, S.-K.; Choi, Y.-J.; Park, I.-K., Mucoadhesive Chitosan Derivatives as Novel Drug Carriers. *Curr. Pharm. Des.* **2015,** *21* (29), 4285-4309.
3. Peer, D.; Karp, J. M.; Hong, S.; Farokhzad, O. C.; Margalit, R.; Langer, R., Nanocarriers as an Emerging Platform for Cancer Therapy. *Nat. Nanotechnol.* **2007,** *2* (12), 751.
4. Singh, R.; Lillard Jr, J. W., Nanoparticle-Based Targeted Drug Delivery. *Exp. Mol. Pathol.* **2009,** *86* (3), 215-223.
5. Sun, T.; Zhang, Y. S.; Pang, B.; Hyun, D. C.; Yang, M.; Xia, Y., Engineered Nanoparticles for Drug Delivery in Cancer Therapy. *Angew. Chem., Int. Ed.* **2014,** *53* (46), 12320-12364.
6. Cheung, R. C. F.; Ng, T. B.; Wong, J. H.; Chan, W. Y., Chitosan: An Update on Potential Biomedical and Pharmaceutical Applications. *Mar. Drugs* **2015,** *13* (8), 5156-5186.
7. Younes, I.; Rinaudo, M., Chitin and Chitosan Preparation from Marine Sources. Structure, Properties and Applications. *Mar. Drugs* **2015,** *13* (3), 1133-1174.
8. Croisier, F.; Jérôme, C., Chitosan-based biomaterials for tissue engineering. *European Polymer Journal* **2013,** *49* (4), 780-792.
9. Karagozlu, M. Z.; Kim, S.-K., Anti-Cancer Effects of Chitin and Chitosan Derivatives. In *Handbook of Anticancer Drugs from Marine Origin*, Kim, S.-K., Ed. Springer: 2015; pp 413-421.
10. Martins, A. F.; Facchi, S. P.; Follmann, H. D.; Pereira, A. G.; Rubira, A. F.; Muniz, E. C., Antimicrobial Activity of Chitosan Derivatives Containing N-Quaternized Moieties in Its Backbone: A Review. *Int. J. Mol. Sci.* **2014,** *15* (11), 20800-20832.
11. Ngo, D.-H.; Kim, S.-K., Antioxidant Effects of Chitin, Chitosan, and Their Derivatives. In *Advances in Food and Nutrition Research*, Elsevier: 2014; Vol. 73, pp 15-31.
12. Kumar, M. R.; Muzzarelli, R. A.; Muzzarelli, C.; Sashiwa, H.; Domb, A., Chitosan Chemistry and Pharmaceutical Perspectives. *Chem. Rev.* **2004,** *104* (12), 6017-6084.
13. Chandy, T.; Sharma, C. P., Chitosan-as a Biomaterial. *Biomater., Artif. Cells, Artif. Organs* **1990,** *18* (1), 1-24.
14. Zhang, Y.; Zhang, M., Three-Dimensional Macroporous Calcium Phosphate Bioceramics with Nested Chitosan Sponges for Load-Bearing Bone Implants. *J. Biomed. Mater. Res.* **2002,** *61* (1), 1-8.
15. M Ways, T. M.; Lau, W. M.; Khutoryanskiy, V. V., Chitosan and Its Derivatives for Application in Mucoadhesive Drug Delivery Systems. *Polymers* **2018,** *10* (3), 267.
16. Kim, I.-Y.; Seo, S.-J.; Moon, H.-S.; Yoo, M.-K.; Park, I.-Y.; Kim, B.-C.; Cho, C.-S., Chitosan and Its Derivatives for Tissue Engineering Applications. *Biotechnol. Adv.* **2008,** *26* (1), 1-21.
17. Shukla, S. K.; Mishra, A. K.; Arotiba, O. A.; Mamba, B. B., Chitosan-Based Nanomaterials: A State-of-the-Art Review. *Int. J. Biol. Macromol.* **2013,** *59,* 46-58.

18. Taravel, M.; Domard, A., Collagen and Its Interaction with Chitosan: II. Influence of the Physicochemical Characteristics of Collagen. *Biomaterials* **1995,** *16* (11), 865-871.
19. Taravel, M.; Domard, A., Collagen and Its Interactions with Chitosan: III. Some Biological and Mechanical Properties. *Biomaterials* **1996,** *17* (4), 451-455.
20. Ma, L.; Gao, C.; Mao, Z.; Zhou, J.; Shen, J.; Hu, X.; Han, C., Collagen/Chitosan Porous Scaffolds with Improved Biostability for Skin Tissue Engineering. *Biomaterials* **2003,** *24* (26), 4833-4841.
21. Ueno, H.; Yamada, H.; Tanaka, I.; Kaba, N.; Matsuura, M.; Okumura, M.; Kadosawa, T.; Fujinaga, T., Accelerating Effects of Chitosan for Healing at Early Phase of Experimental Open Wound in Dogs. *Biomaterials* **1999,** *20* (15), 1407-1414.
22. Vakili, M.; Rafatullah, M.; Salamatinia, B.; Abdullah, A. Z.; Ibrahim, M. H.; Tan, K. B.; Gholami, Z.; Amouzgar, P., Application of Chitosan and Its Derivatives as Adsorbents for Dye Removal from Water and Wastewater: A Review. *Carbohydr. Polym.* **2014,** *113*, 115-130.
23. Boamah, P. O.; Huang, Y.; Hua, M.; Zhang, Q.; Wu, J.; Onumah, J.; Sam-Amoah, L. K.; Boamah, P. O., Sorption of Heavy Metal Ions onto Carboxylate Chitosan Derivatives—A Mini-Review. *Ecotoxicol. Environ. Saf.* **2015,** *116*, 113-120.
24. Ngo, H. H.; Guo, W.; Zhang, J.; Liang, S.; Ton-That, C.; Zhang, X., Typical Low Cost Biosorbents for Adsorptive Removal of Specific Organic Pollutants from Water. *Bioresour. Technol.* **2015,** *182*, 353-363.
25. Nechita, P., Applications of chitosan in wastewater treatment. In *Biological Activities and Application of Marine Polysaccharides*, InTech: 2017.
26. Bernkop-Schnürch, A.; Dünnhaupt, S., Chitosan-Based Drug Delivery Systems. *Eur. J. Pharm. Biopharm.* **2012,** *81* (3), 463-469.
27. Bhise, K. S.; Dhumal, R. S.; Paradkar, A. R.; Kadam, S. S., Effect of Drying Methods on Swelling, Erosion and Drug Release from Chitosan–Naproxen Sodium Complexes. *AAPS PharmSciTech* **2008,** *9* (1), 1-12.
28. Saranya, N.; Moorthi, A.; Saravanan, S.; Devi, M. P.; Selvamurugan, N., Chitosan and Its Derivatives for Gene Delivery. *Int. J. Biol. Macromol.* **2011,** *48* (2), 234-238.
29. Gupta, S.; Vyas, S. P., Carbopol/Chitosan Based pH Triggered in Situ Gelling System for Ocular Delivery of Timolol Maleate. *Sci. Pharm.* **2010,** *78* (4), 959-976.
30. Schipper, N. G.; Olsson, S.; Hoogstraate, J. A.; Vårum, K. M.; Artursson, P., Chitosans as Absorption Enhancers for Poorly Absorbable Drugs 2: Mechanism of Absorption Enhancement. *Pharm. Res.* **1997,** *14* (7), 923-929.
31. Casettari, L.; Illum, L., Chitosan in Nasal Delivery Systems for Therapeutic Drugs. *J. Controlled Release* **2014,** *190*, 189-200.
32. Banerjee, T.; Mitra, S.; Singh, A. K.; Sharma, R. K.; Maitra, A., Preparation, Characterization and Biodistribution of Ultrafine Chitosan Nanoparticles. *Int. J. Pharm.* **2002,** *243* (1-2), 93-105.
33. Bugnicourt, L.; Ladavière, C., Interests of Chitosan Nanoparticles Ionically Cross-Linked with Tripolyphosphate for Biomedical Applications. *Prog. Polym. Sci.* **2016,** *60*, 1-17.
34. Fan, W.; Yan, W.; Xu, Z.; Ni, H., Formation Mechanism of Monodisperse, Low Molecular Weight Chitosan Nanoparticles by Ionic Gelation Technique. *Colloids Surf., B* **2012,** *90*, 21-27.

35. Casettari, L.; Vllasaliu, D.; Castagnino, E.; Stolnik, S.; Howdle, S.; Illum, L., PEGylated Chitosan Derivatives: Synthesis, Characterizations and Pharmaceutical Applications. *Prog. Polym. Sci.* **2012,** *37* (5), 659-685.
36. Hirpara, M. R.; Manikkath, J.; Sivakumar, K.; Managuli, R. S.; Gourishetti, K.; Krishnadas, N.; Shenoy, R. R.; Jayaprakash, B.; Rao, C. M.; Mutalik, S., Long Circulating PEGylated-Chitosan Nanoparticles of Rosuvastatin Calcium: Development and in Vitro and in Vivo Evaluations. *Int. J. Biol. Macromol.* **2018,** *107*, 2190-2200.
37. Mohammed, M. A.; Syeda, J.; Wasan, K. M.; Wasan, E. K., An Overview of Chitosan Nanoparticles and Its Application in Non-Parenteral Drug Delivery. *Pharmaceutics* **2017,** *9* (4), 53.
38. Rodrigues, S.; Dionísio, M.; López, C. R.; Grenha, A., Biocompatibility of Chitosan Carriers with Application in Drug Delivery. *J. Funct. Biomater.* **2012,** *3* (3), 615-641.
39. Zhang, M.; Li, X.; Gong, Y.; Zhao, N.; Zhang, X., Properties and Biocompatibility of Chitosan Films Modified by Blending with PEG. *Biomaterials* **2002,** *23* (13), 2641-2648.
40. Garg, N. K.; Dwivedi, P.; Campbell, C.; Tyagi, R. K., Site Specific/Targeted Delivery of Gemcitabine Through Anisamide Anchored Chitosan/Poly Ethylene Glycol Nanoparticles: An Improved Understanding of Lung Cancer Therapeutic Intervention. *Eur. J. Pharm. Sci.* **2012,** *47* (5), 1006-1014.
41. Jiang, X.; Dai, H.; Leong, K. W.; Goh, S. H.; Mao, H. Q.; Yang, Y. Y., Chitosan-g-PEG/DNA Complexes Deliver Gene to the Rat Liver via Intrabiliary and Intraportal Infusions. *J. Gene Med.* **2006,** *8* (4), 477-487.
42. Ragelle, H.; Danhier, F.; Préat, V.; Langer, R.; Anderson, D. G., Nanoparticle-Based Drug Delivery Systems: A Commercial and Regulatory Outlook as the Field Matures. *Expert Opin. Drug Delivery* **2017,** *14* (7), 851-864.
43. Fang, J.; Nakamura, H.; Maeda, H., The EPR Effect: Unique Features of Tumor Blood Vessels for Drug Delivery, Factors Involved, and Limitations and Augmentation of the Effect. *Adv. Drug Delivery Rev.* **2011,** *63* (3), 136-151.
44. Sitti, M., Miniature Devices: Voyage of the Microrobots. *Nature* **2009,** *458* (7242), 1121.
45. Sitti, M.; Ceylan, H.; Hu, W.; Giltinan, J.; Turan, M.; Yim, S.; Diller, E., Biomedical Applications of Untethered Mobile Milli/Microrobots. *Proc. IEEE* **2015,** *103* (2), 205-224.
46. Ceylan, H.; Yasa, I. C.; Yasa, O.; Tabak, A. F.; Giltinan, J.; Sitti, M., 3D-Printed Biodegradable Microswimmer for Drug Delivery and Targeted Cell Labeling. *bioRxiv* **2018**, 379024.
47. Ceylan, H.; Giltinan, J.; Kozielski, K.; Sitti, M., Mobile Microrobots for Bioengineering Applications. *Lab Chip* **2017,** *17* (10), 1705-1724.
48. Peyer, K. E.; Zhang, L.; Nelson, B. J., Bio-inspired Magnetic Swimming Microrobots for Biomedical Applications. *Nanoscale* **2013,** *5* (4), 1259-1272.
49. Chen, X.-Z.; Jang, B.; Ahmed, D.; Hu, C.; Marco, D., Small-Scale Machines Driven by External Power Sources. *Adv. Mater.* **2018**.
50. Honda, T.; Arai, K. I.; Ishiyama, K., Micro Swimming Mechanisms Propelled by External Magnetic Fields. *IEEE Trans. Magn.* **1996,** *32* (5(2)).

51. Behkam, B.; Sitti, M., Design Methodology for Biomimetic Propulsion of Miniature Swimming Robots. *J. Dyn. Syst., Meas., Control* **2006,** *128* (1).
52. Zhang, L.; Abbott, J. J.; Dong, L.; Kratochvil, B. E.; Bell, D.; Nelson, B. J., Artificial Bacterial Flagella: Fabrication and Magnetic Control. *Appl. Phys. Lett.* **2009,** *94* (6).
53. Ghosh, A.; Fischer, P., Controlled Propulsion of Artificial Magnetic Nanostructured Propellers. *Nano Lett.* **2009,** *9* (6).
54. Maruo, S.; Nakamura, O.; Kawata, S., Three-Dimensional Microfabrication with Two-Photon-Absorbed Photopolymerization. *Opt. Lett.* **1997,** *22* (2), 132-134.
55. Sun, H.-B.; Matsuo, S.; Misawa, H., Three-Dimensional Photonic Crystal Structures Achieved with Two-Photon-Absorption Photopolymerization of Resin. *Appl. Phys. Lett.* **1999,** *74* (6), 786-788.
56. Suter, M.; Zhang, L.; Siringil, E. C.; Peters, C.; Luehmann, T.; Ergeneman, O.; Peyer, K. E.; Nelson, B. J.; Hierold, C., Superparamagnetic Microrobots: Fabrication by Two-Photon Polymerization and Biocompatibility. *Biomed. Microdevices* **2013,** *15* (6).
57. Richter, B.; Pauloehrl, T.; Kaschke, J.; Fichtner, D.; Fischer, J.; Greiner, A. M.; Wedlich, D.; Wegener, M.; Delaittre, G.; Barner-Kowollik, C., Three-Dimensional Microscaffolds Exhibiting Spatially Resolved Surface Chemistry. *Adv. Mater.* **2013,** *25* (42), 6117-6122.
58. Ceylan, H.; Yasa, I. C.; Sitti, M., 3D Chemical Patterning of Micromaterials for Encoded Functionality. *Adv. Mater.* **2017,** *29* (9).
59. Tottori, S.; Zhang, L.; Qiu, F.; Krawczyk, K. K.; Franco-Obregón, A.; Nelson, B. J., Magnetic Helical Micromachines: Fabrication, Controlled Swimming, and Cargo Transport. *Adv. Mater.* **2012,** *24* (6), 811-816.
60. Qiu, F.; Mhanna, R.; Zhang, L.; Ding, Y.; Fujita, S.; Nelson, B. J., Artificial Bacterial Flagella Functionalized with Temperature-Sensitive Liposomes for Controlled Release. *Sens. Actuators, B* **2014,** *196*, 676-681.
61. Qiu, F.; Fujita, S.; Mhanna, R.; Zhang, L.; Simona, B. R.; Nelson, B. J., Magnetic Helical Microswimmers Functionalized With Lipoplexes for Targeted Gene Delivery. *Adv. Funct. Mater.* **2015,** *25* (11), 1666-1671.
62. Servant, A.; Qiu, F.; Mazza, M.; Kostarelos, K.; Nelson, B. J., Controlled in Vivo Swimming of a Swarm of Bacteria-Like Microrobotic Flagella. *Adv. Mater.* **2015,** *27* (19), 2981-2988.
63. Lavan, D. A.; McGuire, T.; Langer, R., Small-Scale Systems for in Vivo Drug Delivery. *Nat. Biotechnol.* **2003,** *21* (10), 1184-1191.
64. Ferrari, M., Cancer Nanotechnology: Opportunities and Challenges. *Nat. Rev. Cancer* **2005,** *5* (3), 161-171.
65. Farokhzad, O. C.; Karp, J. M.; Langer, R., Nanoparticle–Aptamer Bioconjugates for Cancer Targeting. *Expert Opin. Drug Delivery* **2006,** *3* (3), 311-324.
66. Zhang, L.; Gu, F.; Chan, J.; Wang, A.; Langer, R.; Farokhzad, O., Nanoparticles in Medicine: Therapeutic Applications and Developments. *Clin. Pharmacol. Ther.* **2008,** *83* (5), 761-769.
67. Farokhzad, O. C.; Langer, R., Impact of Nanotechnology on Drug Delivery. *ACS Nano* **2009,** *3* (1), 16-20.
68. Kean, T.; Thanou, M., Biodegradation, Biodistribution and Toxicity of Chitosan. *Adv. Drug Delivery Rev.* **2010,** *62* (1), 3-11.

69. Sogias, I. A.; Khutoryanskiy, V. V.; Williams, A. C., Exploring the Factors Affecting the Solubility of Chitosan in Water. *Macromol. Chem. Phys.* **2010,** *211* (4), 426-433.
70. El-Shabouri, M., Positively Charged Nanoparticles for Improving the Oral Bioavailability of Cyclosporin-A. *Int. J. Pharm.* **2002,** *249* (1-2), 101-108.
71. Brunel, F.; Véron, L.; David, L.; Domard, A.; Delair, T., A Novel Synthesis of Chitosan Nanoparticles in Reverse Emulsion. *Langmuir* **2008,** *24* (20), 11370-11377.
72. Maitra, A.; Ghosh, P. K.; De, T. K.; Sahoo, S. K., Process for the Preparation of Highly Monodispersed Polymeric Hydrophilic Nanoparticles. Google Patents: 1999.
73. Divya, K.; Jisha, M., Chitosan Nanoparticles Preparation and Applications. *Environ. Chem. Lett.* **2017,** *16* (1), 101–112.
74. Calvo, P.; Remunan-Lopez, C.; Vila-Jato, J. L.; Alonso, M., Novel Hydrophilic Chitosan-Polyethylene Oxide Nanoparticles as Protein Carriers. *J. Appl. Polym. Sci.* **1997,** *63* (1), 125-132.
75. Grenha, A., Chitosan Nanoparticles: a Survey of Preparation Methods. *J. Drug Targeting* **2012,** *20* (4), 291-300.
76. Makhlof, A.; Tozuka, Y.; Takeuchi, H., Design and Evaluation of Novel pH-Sensitive Chitosan Nanoparticles for Oral Insulin Delivery. *Eur. J. Pharm. Sci.* **2011,** *42* (5), 445-451.
77. Huang, Y.; Cai, Y.; Lapitsky, Y., Factors Affecting the Stability of Chitosan/Tripolyphosphate Micro-and Nanogels: Resolving the Opposing Findings. *J. Mater. Chem. B* **2015,** *3* (29), 5957-5970.
78. Gan, Q.; Wang, T.; Cochrane, C.; McCarron, P., Modulation of Surface Charge, Particle Size and Morphological Properties of Chitosan–TPP Nanoparticles Intended for Gene Delivery. *Colloids Surf., B* **2005,** *44* (2-3), 65-73.
79. Amani, A.; Mohammadyani, D., Artificial Neural Networks: Applications in Nanotechnology. In *Artificial Neural Networks-Application*, InTech: 2011.
80. Baharifar, H.; Amani, A., Size, Loading Efficiency, and Cytotoxicity of Albumin-Loaded Chitosan Nanoparticles: An Artificial Neural Networks Study. *J. Pharm. Sci.* **2017,** *106* (1), 411-417.
81. Hashad, R. A.; Ishak, R. A.; Fahmy, S.; Mansour, S.; Geneidi, A. S., Chitosan-Tripolyphosphate Nanoparticles: Optimization of Formulation Parameters for Improving Process Yield at a Novel pH Using Artificial Neural Networks. *Int. J. Biol. Macromol.* **2016,** *86*, 50-58.
82. Baharifar, H.; Amani, A., Cytotoxicity of Chitosan/Streptokinase Nanoparticles as a Function of Size: An Artificial Neural Networks Study. *Nanomedicine* **2016,** *12* (1), 171-180.
83. Aslan, C.; Çelebi, N.; Değim, İ. T.; Atak, A.; Özer, Ç., Development of Interleukin-2 Loaded Chitosan-Based Nanogels Using Artificial Neural Networks and Investigating the Effects on Wound Healing in Rats. *AAPS PharmSciTech* **2017,** *18* (4), 1019-1030.
84. Ali, H. S.; Blagden, N.; York, P.; Amani, A.; Brook, T., Artificial Neural Networks Modelling the Prednisolone Nanoprecipitation in Microfluidic Reactors. *Eur. J. Pharm. Sci.* **2009,** *37* (3-4), 514-522.
85. Amani, A.; York, P.; Chrystyn, H.; Clark, B. J., Factors Affecting the Stability of Nanoemulsions—Use of Artificial Neural Networks. *Pharm. Res.* **2010,** *27* (1), 37-45.

86. Ketabchi, N.; Naghibzadeh, M.; Adabi, M.; Esnaashari, S. S.; Faridi-Majidi, R., Preparation and Optimization of Chitosan/Polyethylene Oxide Nanofiber Diameter Using Artificial Neural Networks. *Neural Comput. Appl.* **2017,** *28* (11), 3131-3143.
87. Cline, G. W.; Hanna, S. B., Kinetics and Mechanisms of the Aminolysis of N-Hydroxysuccinimide Esters in Aqueous Buffers. *J. Org. Chem.* **1988,** *53* (15), 3583-3586.
88. Le, Y.; Scott, M. D., Immunocamouflage: The Biophysical Basis of Immunoprotection by Grafted Methoxypoly (ethylene glycol)(mPEG). *Acta Biomater.* **2010,** *6* (7), 2631-2641.
89. Bhattacharjee, S., DLS and Zeta Potential–What They are and What They are not? *J. Controlled Release* **2016,** *235*, 337-351.
90. Patel, V. R.; Agrawal, Y., Nanosuspension: An Approach to Enhance Solubility of Drugs. *J. Adv. Pharm. Technol. Res.* **2011,** *2* (2), 81.
91. Alexander, D.; Tropsha, A.; Winkler, D. A., Beware of R 2: Simple, Unambiguous Assessment of the Prediction Accuracy of QSAR and QSPR Models. *J. Chem. Inf. Model.* **2015,** *55* (7), 1316-1322.
92. Kaji, E. H.; Leiden, J. M., Gene and Stem Cell Therapies. *Jama* **2001,** *285* (5), 545-550.
93. Liu, W. G.; De Yao, K., Chitosan and Its Derivatives—a Promising Non-Viral Vector for Gene Transfection. *J. Controlled Release* **2002,** *83* (1), 1-11.
94. Gilad, Y.; Firer, M.; Gellerman, G., Recent Innovations in Peptide Based Targeted Drug Delivery to Cancer Cells. *Biomedicines* **2016,** *4* (2), 11.
95. Okur, A. C.; Erkoc, P.; Kizilel, S., Targeting Cancer Cells via Tumor-Homing Peptide CREKA Functional PEG Nanoparticles. *Colloids Surf., B* **2016,** *147*, 191-200.
96. Zhao, J.; Zhang, B.; Shen, S.; Chen, J.; Zhang, Q.; Jiang, X.; Pang, Z., CREKA Peptide-Conjugated Dendrimer Nanoparticles for Glioblastoma Multiforme Delivery. *J. Colloid Interface Sci.* **2015,** *450*, 396-403.
97. Sitti, M., *Mobile Microrobotics*. MIT Press: 2017.
98. Nelson, B. J.; Kaliakatsos, I. K.; Abbott, J. J., Microrobots for Minimally Invasive Medicine. *Annu. Rev. Biomed. Eng.* **2010,** *12*, 55-85.
99. Xu, H.; Medina-Sánchez, M.; Magdanz, V.; Schwarz, L.; Hebenstreit, F.; Schmidt, O. G., Sperm-Hybrid Micromotor for Targeted Drug Delivery. *ACS Nano* **2017**.
100. Park, B.-W.; Zhuang, J.; Yasa, O.; Sitti, M., Multifunctional Bacteria-Driven Microswimmers for Targeted Active Drug Delivery. *ACS Nano* **2017,** *11* (9).
101. Alapan, Y.; Yasa, O.; Schauer, O.; Giltinan, J.; Tabak, A. F.; Sourjik, V.; Sitti, M., Soft Erythrocyte-Based Bacterial Microswimmers for Cargo Delivery. *Science Robotics* **2018,** *3* (17), eaar4423.
102. Zhang, L.; Peyer, K. E.; Nelson, B. J., Artificial Bacterial Flagella for Micromanipulation. *Lab Chip* **2010,** *10* (17), 2203-2215.
103. Srivastava, S. K.; Medina-Sánchez, M.; Koch, B.; Schmidt, O. G., Medibots: Dual-Action Biogenic Microdaggers for Single-Cell Surgery and Drug Release. *Adv. Mater.* **2016,** *28* (5), 832-837.
104. Tasoglu, S.; Diller, E.; Guven, S.; Sitti, M.; Demirci, U., Untethered Micro-Robotic Coding of Three-Dimensional Material Composition. *Nat. Commun.* **2014,** *5*, 3124.
105. Carlsen, R.; Edwards, M. R.; Zhuang, J.; Pacoret, C.; Sitti, M., Magnetic Steering Control of Multi-Cellular Bio-Hybrid Microswimmers. *Lab Chip* **2014,** *14* (19).

106. Vannozzi, L.; Yasa, I. C.; Ceylan, H.; Menciassi, A.; Ricotti, L.; Sitti, M., Self-Folded Hydrogel Tubes for Implantable Muscular Tissue Scaffolds. *Macromol. Biosci.* **2018**, 1700377.
107. Kawata, S.; Sun, H.-B.; Tanaka, T.; Takada, K., Finer Features for Functional Microdevices. *Nature* **2001,** *412* (6848), 697-698.
108. Hohmann, J. K.; Renner, M.; Waller, E. H.; von Freymann, G., Three-Dimensional μ-Printing: An Enabling Technology. *Adv. Opt. Mater.* **2015,** *3* (11), 1488-1507.
109. Linsley, C. S.; Wu, B. M., Recent Advances in Light-Responsive on-demand Drug-Delivery Systems. *Ther. Delivery* **2017,** *8* (2), 89-107.
110. Barhoumi, A.; Liu, Q.; Kohane, D. S., Ultraviolet Light-Mediated Drug Delivery: Principles, Applications, and Challenges. *J. Controlled Release* **2015,** *219*, 31-42.
111. Yu, L. M.; Kazazian, K.; Shoichet, M. S., Peptide Surface Modification of Methacrylamide Chitosan for Neural Tissue Engineering Applications. *J. Biomed. Mater. Res., Part A* **2007,** *82* (1), 243-255.
112. Hong, V.; Presolski, S. I.; Ma, C.; Finn, M., Analysis and Optimization of Copper-Catalyzed Azide–Alkyne Cycloaddition for Bioconjugation. *Angew. Chem., Int. Ed.* **2009,** *48* (52), 9879-9883.
113. Erkoc, P.; Seker, F.; Bagci-Onder, T.; Kizilel, S., Gelatin Methacryloyl Hydrogels in the Absence of a Crosslinker as 3D Glioblastoma Multiforme (GBM)-Mimetic Microenvironment. *Macromol. Biosci.* **2018**.
114. Mahmoudi, M.; Hofmann, H.; Rothen-Rutishauser, B.; Petri-Fink, A., Assessing the in Vitro and in Vivo Toxicity of Superparamagnetic Iron Oxide Nanoparticles. *Chem. Rev.* **2011,** *112* (4), 2323-2338.
115. Ulery, B. D.; Nair, L. S.; Laurencin, C. T., Biomedical Applications of Biodegradable Polymers. *J. Polym. Sci., Part B: Polym. Phys.* **2011,** *49* (12), 832-864.
116. Hankiewicz, J.; Swierczek, E., Lysozyme in Human Body Fluids. *Clin. Chim. Acta* **1974,** *57* (3), 205-209.
117. Klockars, M.; Reitamo, S., Tissue Distribution of Lysozyme in Man. *J. Histochem. Cytochem.* **1975,** *23* (12), 932-940.
118. Porstmann, B.; Jung, K.; Schmechta, H.; Evers, U.; Pergande, M.; Porstmann, T.; Kramm, H.-J.; Krause, H., Measurement of Lysozyme in Human Body Fluids: Comparison of Various Enzyme Immunoassay Techniques and Their Diagnostic Application. *Clin. Biochem.* **1989,** *22* (5), 349-355.
119. Jennings, J., Controlling Chitosan Degradation Properties in Vitro and in Vivo. In *Chitosan Based Biomaterials Volume 1*, Elsevier: 2017; pp 159-182.
120. Tamada, J.; Langer, R., Erosion Kinetics of Hydrolytically Degradable Polymers. *Proc. Natl. Acad. Sci. U. S. A.* **1993,** *90* (2), 552-556.
121. Freier, T.; Koh, H. S.; Kazazian, K.; Shoichet, M. S., Controlling Cell Adhesion and Degradation of Chitosan Films by N-acetylation. *Biomaterials* **2005,** *26* (29), 5872-5878.
122. Guangyuan, L.; Baiyang, S.; Gan, W.; Yujun, W.; Yandao, G.; Xiufang, Z.; Lihai, Z., Controlling the Degradation of Covalently Cross-Linked Carboxymethyl Chitosan Utilizing Bimodal Molecular Weight Distribution. *J. Biomater. Appl.* **2009,** *23* (5), 435-451.

123. Wei, L.; Cai, C.; Lin, J.; Wang, L.; Zhang, X., Degradation Controllable Biomaterials Constructed from Lysozyme-Loaded Ca-Alginate Microparticle/Chitosan Composites. *Polymer* **2011,** *52* (22), 5139-5148.
124. Lim, S. M.; Song, D. K.; Oh, S. H.; Lee-Yoon, D. S.; Bae, E. H.; Lee, J. H., In Vitro and in Vivo Degradation Behavior of Acetylated Chitosan Porous Beads. *J. Biomater. Sci., Polym. Ed.* **2008,** *19* (4), 453-466.
125. Kaneko, S.; Nakayama, H.; Yoshino, Y.; Fushimi, D.; Yamaguchi, K.; Horiike, Y.; Nakanishi, J., Photocontrol of Cell Adhesion on Amino-Bearing Surfaces by Reversible Conjugation of Poly (ethylene glycol) via a Photocleavable Linker. *Phys. Chem. Chem. Phys.* **2011,** *13* (9), 4051-4059.
126. Wegner, S. V.; Sentürk, O. I.; Spatz, J. P., Photocleavable Linker for the Patterning of Bioactive Molecules. *Sci. Rep.* **2015,** *5*, 18309.
127. Klán, P.; Šolomek, T. s.; Bochet, C. G.; Blanc, A. l.; Givens, R.; Rubina, M.; Popik, V.; Kostikov, A.; Wirz, J., Photoremovable Protecting Groups in Chemistry and Biology: Reaction Mechanisms and Efficacy. *Chem. Rev.* **2012,** *113* (1), 119-191.
128. Ruskowitz, E. R.; DeForest, C. A., Photoresponsive Biomaterials for Targeted Drug Delivery and 4D Cell Culture. *Nat. Rev. Mater.* **2018,** *3*, 17087.

APPENDIX A - RAW DYNAMIC LIGHT SCATTERING DATA

According to international standards (ISO22412:2017 & ASTM E2490-09(15)), z-average is the most robust value, so z-average value was reported for size of nanoparticles in the study.

1) 2 kDa PEG – 4 µmole – pH 6

		Size (d.nm):	% Intensity:	St Dev (d.nm):
Z-Average (d.nm): 75.71	Peak 1:	95.85	96.5	55.46
PdI: 0.297	Peak 2:	4409	3.5	1030
Intercept: 0.927	Peak 3:	0.000	0.0	0.000
Result quality : Good				

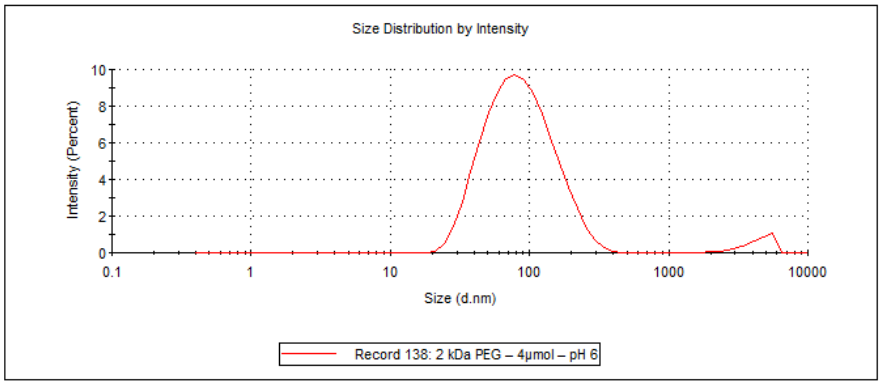

Figure A1. Size of 2 kDa PEG – 4 µmole – pH 6

		Mean (mV)	Area (%)	St Dev (mV)
Zeta Potential (mV): 19.8	Peak 1:	19.8	100.0	6.13
Zeta Deviation (mV): 5.91	Peak 2:	0.00	0.0	0.00
Conductivity (mS/cm): 1.25	Peak 3:	0.00	0.0	0.00
Result quality : Good				

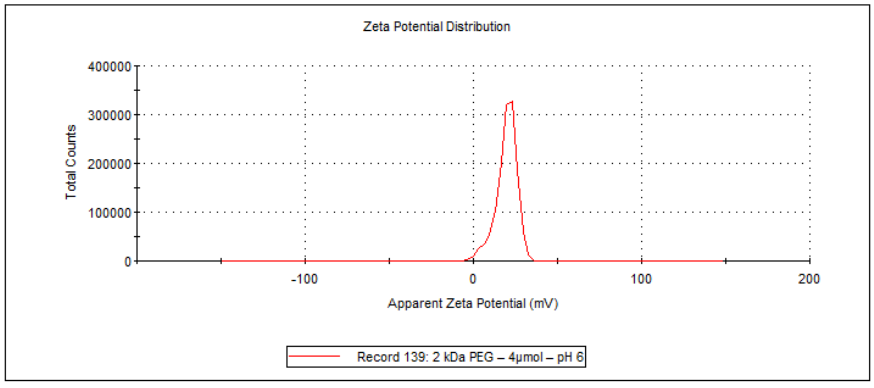

Figure A2. Zeta potential of 2 kDa PEG – 4 µmole – pH

2) 2 kDa PEG – 4 µmole – pH 7

a) Size

		Size (d.nm):	% Intensity:	St Dev (d.nm):
Z-Average (d.nm): 72.09	Peak 1:	85.12	100.0	37.72
PdI: 0.164	Peak 2:	0.000	0.0	0.000
Intercept: 0.948	Peak 3:	0.000	0.0	0.000
Result quality : Good				

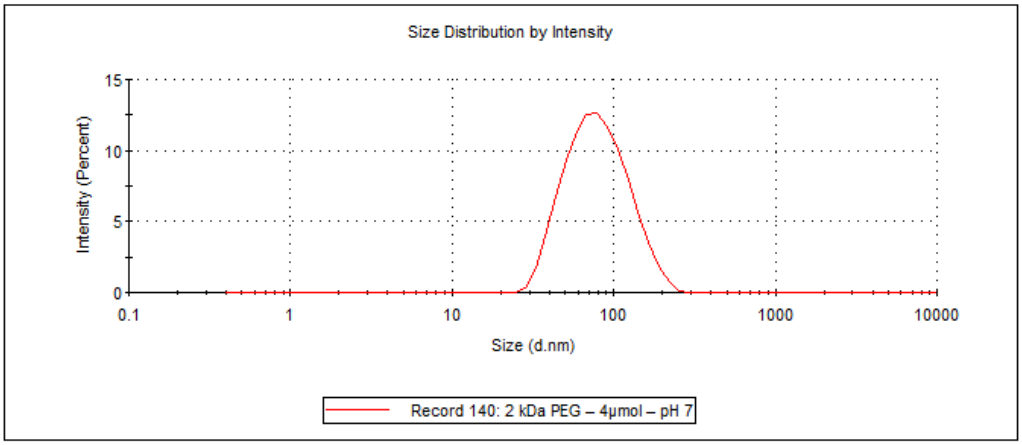

Figure A3. Size of 2 kDa PEG – 4 µmole – pH 7

b) Zeta Potential

		Mean (mV)	Area (%)	St Dev (mV)
Zeta Potential (mV): 7.07	Peak 1:	7.05	100.0	3.54
Zeta Deviation (mV): 3.33	Peak 2:	0.00	0.0	0.00
Conductivity (mS/cm): 1.36	Peak 3:	0.00	0.0	0.00
Result quality : Good				

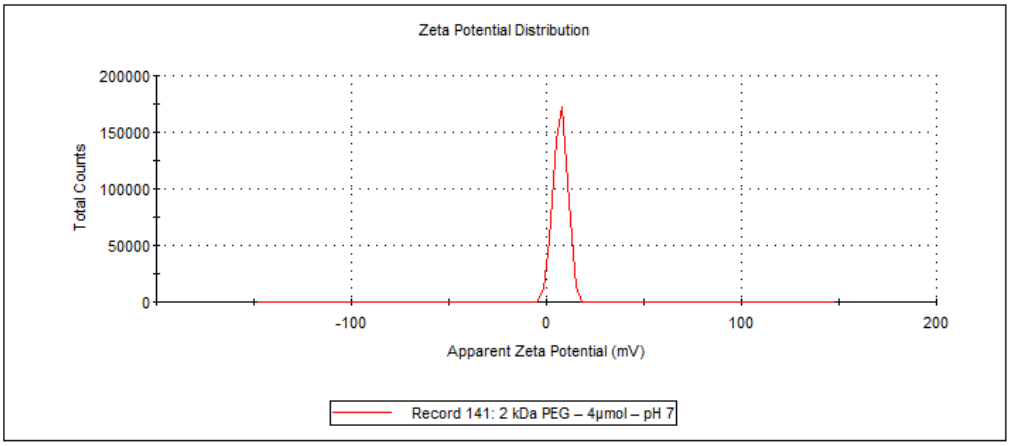

Figure A4. Zeta potential of 2 kDa PEG – 4 µmole – pH

3) 2 kDa PEG – 12 µmole – pH 6

a) Size

		Size (d.nm):	% Intensity:	St Dev (d.nm):
Z-Average (d.nm): 72.74	Peak 1:	96.04	98.0	54.83
PdI: 0.257	Peak 2:	3926	2.0	1239
Intercept: 0.943	Peak 3:	0.000	0.0	0.000

Result quality : Good

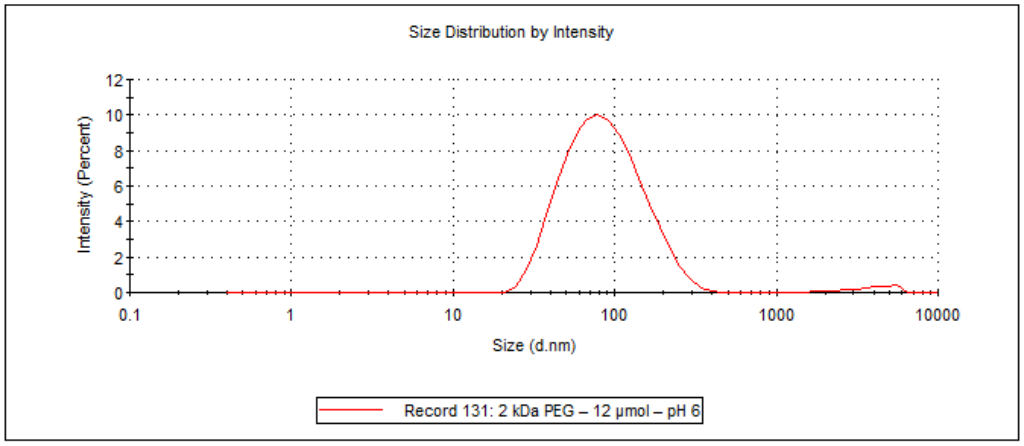

Figure A5. Size of 2 kDa PEG – 12 µmole – pH 6

b) Zeta Potential

		Mean (mV)	Area (%)	St Dev (mV)
Zeta Potential (mV): 17.7	Peak 1:	17.6	100.0	3.78
Zeta Deviation (mV): 3.49	Peak 2:	0.00	0.0	0.00
Conductivity (mS/cm): 1.24	Peak 3:	0.00	0.0	0.00

Result quality : Good

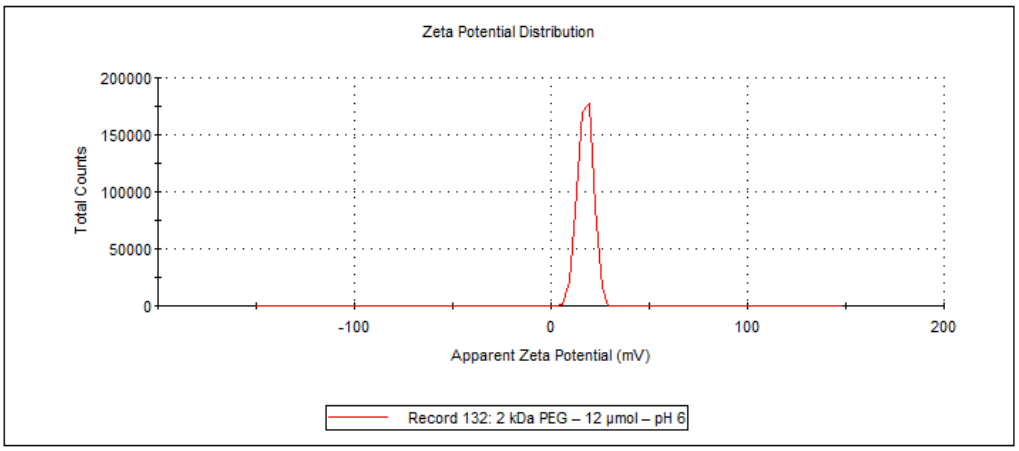

Figure A6. Zeta potential of 2 kDa PEG – 12 µmole – pH 6

4) 2 kDa PEG – 12 µmole – pH 7

a) Size

		Size (d.nm):	% Intensity:	St Dev (d.nm):
Z-Average (d.nm): 75.01	Peak 1:	89.38	99.0	39.84
PdI: 0.189	Peak 2:	4638	1.0	811.2
Intercept: 0.947	Peak 3:	0.000	0.0	0.000
Result quality : Good				

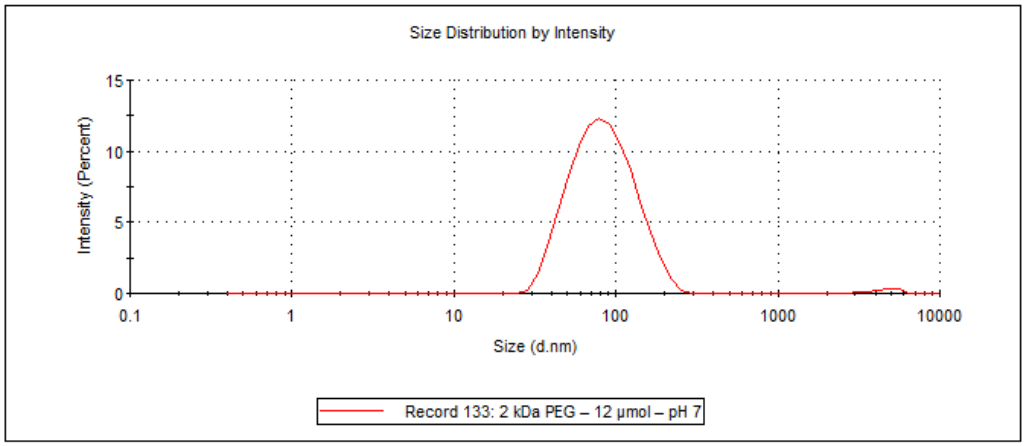

Figure A7. Size of 2 kDa PEG – 12 µmole – pH 7

b) Zeta Potential

		Mean (mV)	Area (%)	St Dev (mV)
Zeta Potential (mV): 5.96	Peak 1:	5.90	100.0	3.55
Zeta Deviation (mV): 3.34	Peak 2:	0.00	0.0	0.00
Conductivity (mS/cm): 1.42	Peak 3:	0.00	0.0	0.00
Result quality : Good				

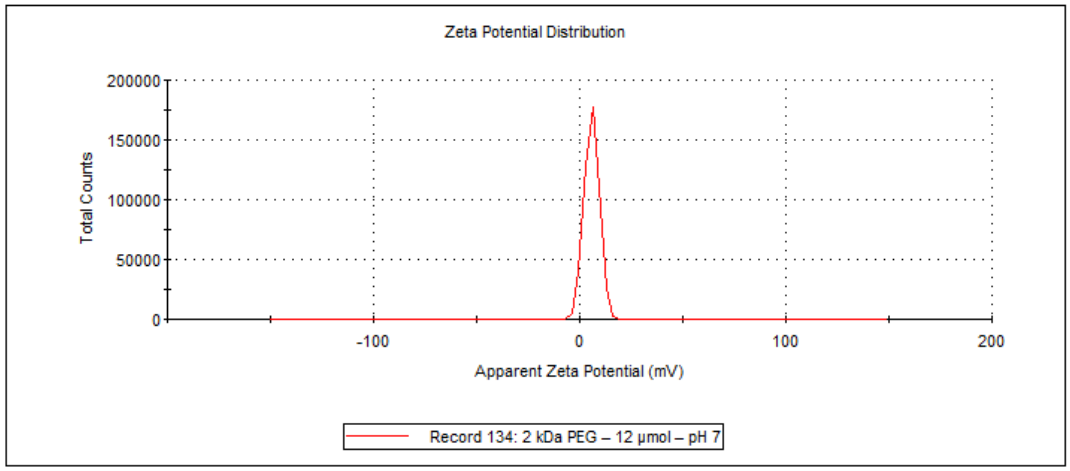

Figure A8. Zeta potential of 2 kDa PEG – 12 µmole – pH 7

5) 2 kDa PEG – 12 µmole – pH 7.4

a) Size

		Size (d.nm):	% Intensity:	St Dev (d.nm):
Z-Average (d.nm): 108.6	Peak 1:	147.3	100.0	86.19
PdI: 0.251	Peak 2:	0.000	0.0	0.000
Intercept: 0.917	Peak 3:	0.000	0.0	0.000
Result quality : Good				

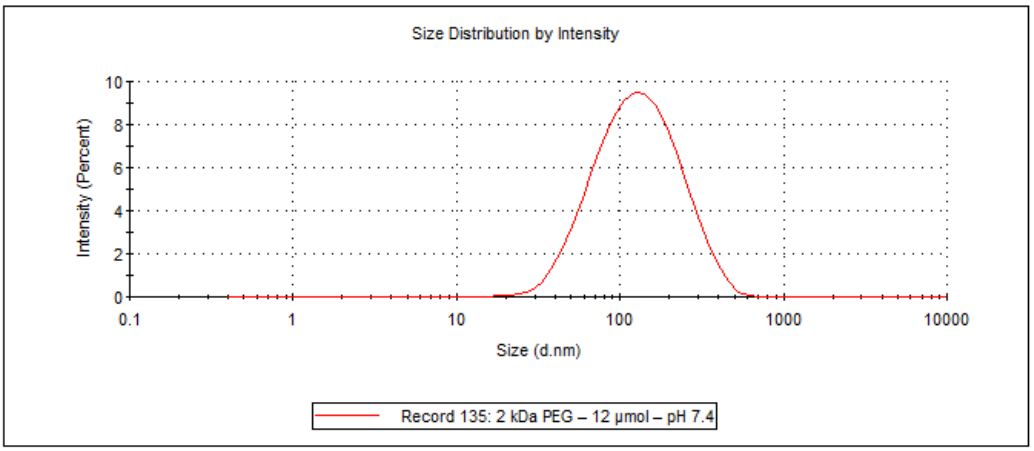

Figure A9. Size of 2 kDa PEG – 12 µmole – pH 7.4

b) Zeta Potential

		Mean (mV)	Area (%)	St Dev (mV)
Zeta Potential (mV): 3.83	Peak 1:	3.83	100.0	3.36
Zeta Deviation (mV): 3.11	Peak 2:	0.00	0.0	0.00
Conductivity (mS/cm): 1.53	Peak 3:	0.00	0.0	0.00
Result quality : Good				

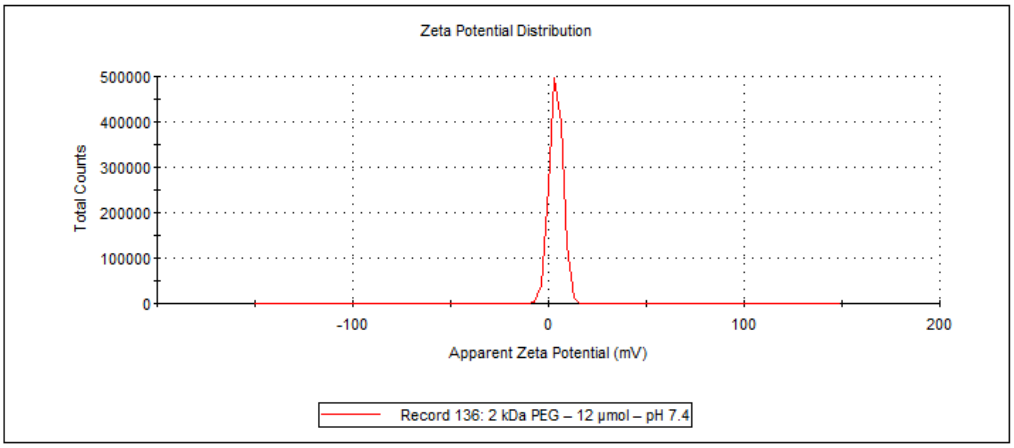

Figure A10. Zeta potential of 2 kDa PEG – 12 µmole – pH 7.4

6) 2 kDa PEG – 20 µmole – pH 6

a) Size

		Size (d.nm):	% Intensity:	St Dev (d.nm):
Z-Average (d.nm): 57.50	Peak 1:	73.84	99.3	38.62
PdI: 0.225	Peak 2:	4428	0.7	910.6
Intercept: 0.941	Peak 3:	0.000	0.0	0.000
Result quality : Good				

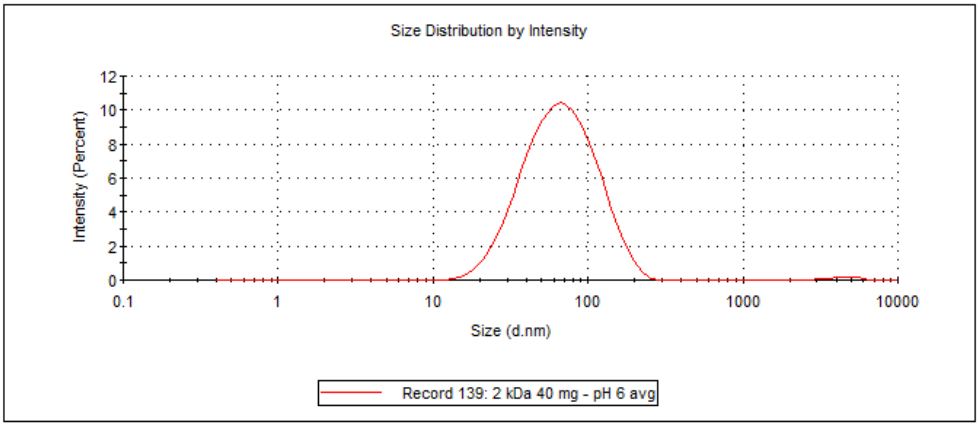

Figure A11. Size of 2 kDa PEG – 20 µmole – pH 6

b) Zeta Potential

		Mean (mV)	Area (%)	St Dev (mV)
Zeta Potential (mV): 11.5	Peak 1:	11.4	100.0	4.69
Zeta Deviation (mV): 4.53	Peak 2:	0.00	0.0	0.00
Conductivity (mS/cm): 1.22	Peak 3:	0.00	0.0	0.00
Result quality : Good				

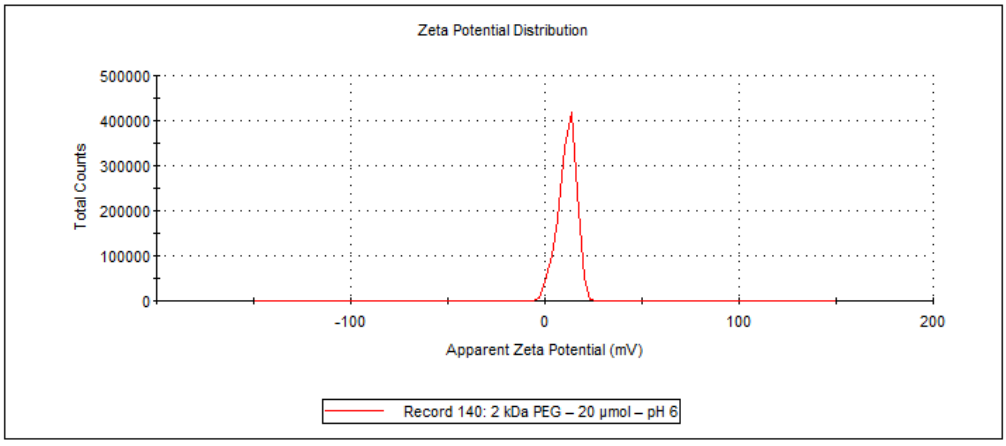

Figure A12. Zeta potential of 2 kDa PEG – 20 µmole – pH 6

7) 2 kDa PEG – 20 µmole – pH 7

a) Size

		Size (d.nm):	% Intensity:	St Dev (d.nm):
Z-Average (d.nm): 71.55	Peak 1:	82.68	97.8	35.69
PdI: 0.206	Peak 2:	4550	2.2	860.1
Intercept: 0.951	Peak 3:	0.000	0.0	0.000
Result quality : Good				

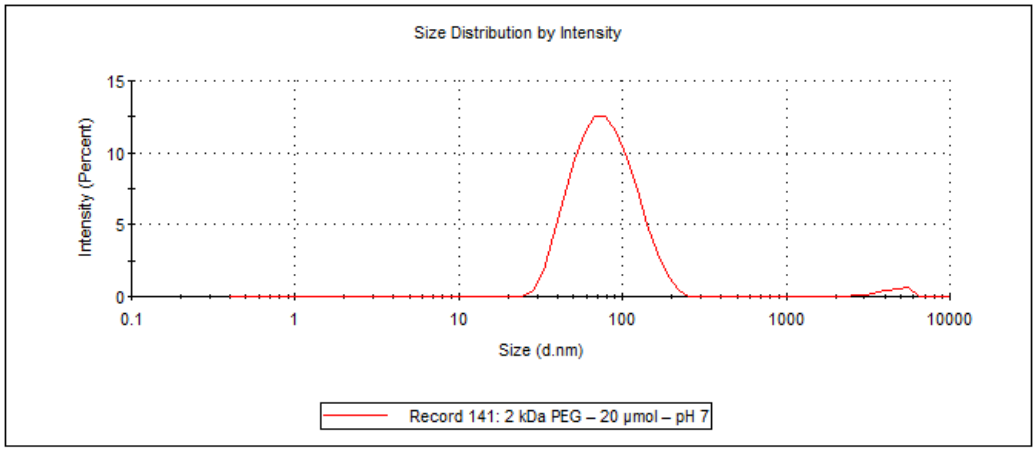

Figure A13. Size of 2 kDa PEG – 20 µmole – pH 7

b) Zeta Potential

		Mean (mV)	Area (%)	St Dev (mV)
Zeta Potential (mV): 4.99	Peak 1:	4.95	100.0	3.45
Zeta Deviation (mV): 3.20	Peak 2:	0.00	0.0	0.00
Conductivity (mS/cm): 1.39	Peak 3:	0.00	0.0	0.00
Result quality : Good				

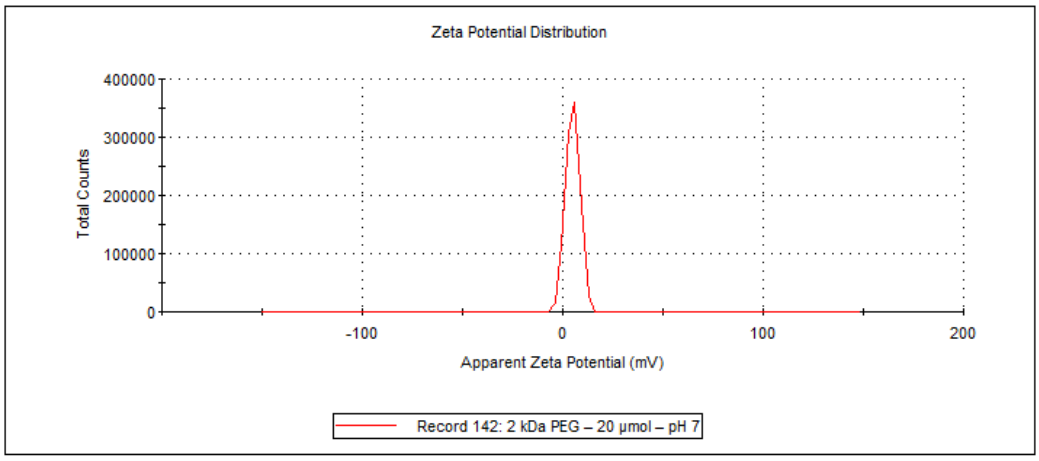

Figure A14. Zeta potential of 2 kDa PEG – 20 µmole – pH 7

8) 2 kDa PEG – 20 µmole – pH 7.4

a) Size

		Size (d.nm):	% Intensity:	St Dev (d.nm):
Z-Average (d.nm): 112.8	Peak 1:	128.2	100.0	49.45
PdI: 0.180	Peak 2:	0.000	0.0	0.000
Intercept: 0.922	Peak 3:	0.000	0.0	0.000
Result quality : Good				

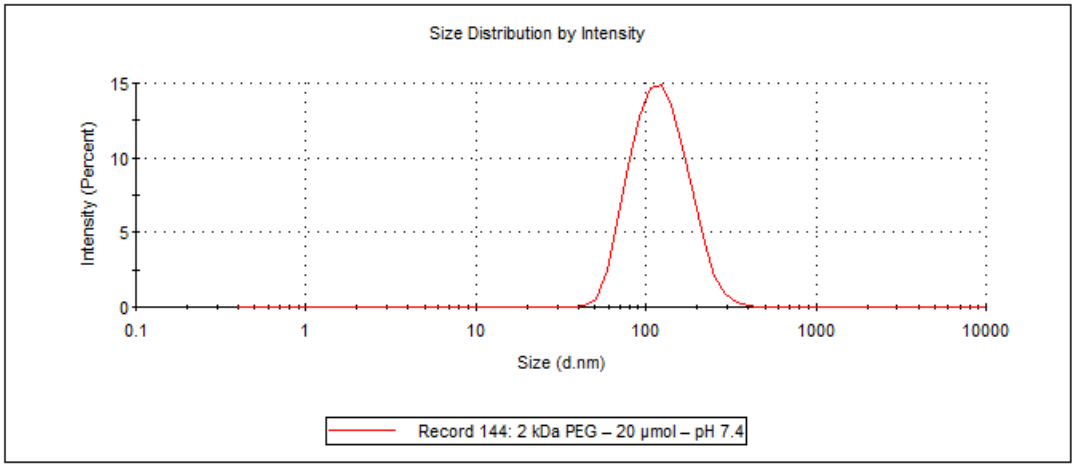

Figure A15. Size of 2 kDa PEG – 20 µmole – pH 7.4

b) Zeta Potential

		Mean (mV)	Area (%)	St Dev (mV)
Zeta Potential (mV): 3.15	Peak 1:	3.15	100.0	3.10
Zeta Deviation (mV): 2.90	Peak 2:	0.00	0.0	0.00
Conductivity (mS/cm): 1.45	Peak 3:	0.00	0.0	0.00
Result quality : Good				

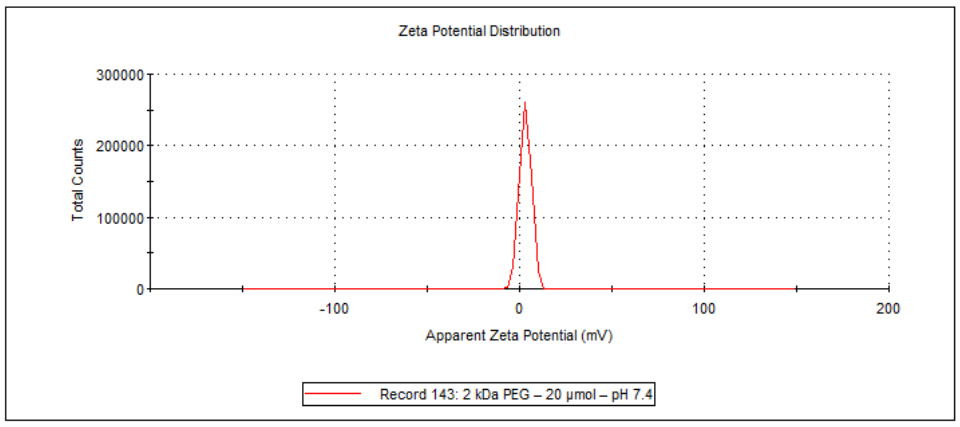

Figure A16. Zeta potential of 2 kDa PEG – 20 µmole – pH 7.4

9) 5 kDa PEG – 4 µmole – pH 6

a) Size

		Size (d.nm):	% Intensity:	St Dev (d.nm):
Z-Average (d.nm): 72.40	Peak 1:	94.37	99.8	51.62
PdI: 0.221	Peak 2:	5.807	0.1	1.052
Intercept: 0.943	Peak 3:	12.54	0.1	2.061
Result quality : Good				

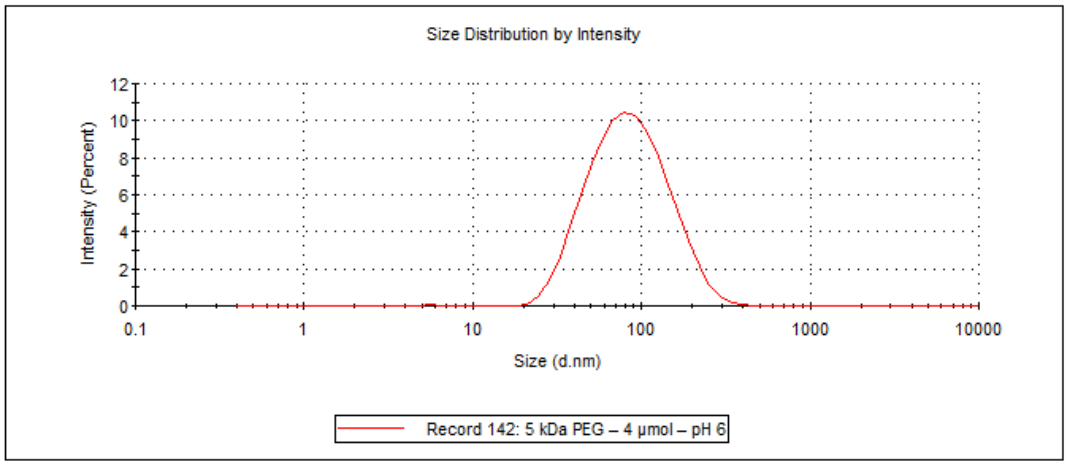

Figure A17. Size of 5 kDa PEG – 4 µmole – pH 6

b) Zeta Potential

		Mean (mV)	Area (%)	St Dev (mV)
Zeta Potential (mV): 18.3	Peak 1:	18.3	100.0	4.39
Zeta Deviation (mV): 4.17	Peak 2:	0.00	0.0	0.00
Conductivity (mS/cm): 1.26	Peak 3:	0.00	0.0	0.00
Result quality : Good				

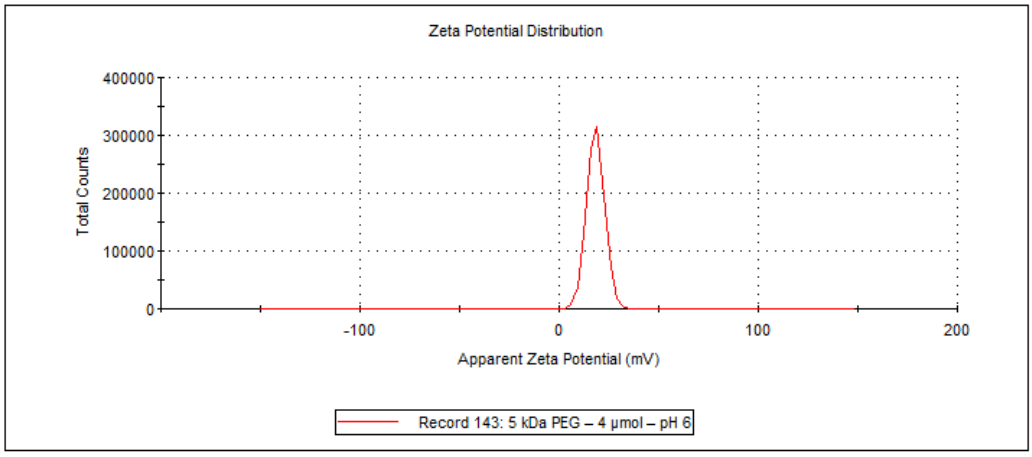

Figure A18. Zeta potential of 5 kDa PEG – 4 µmole – pH 6

10) 5 kDa PEG – 4 µmole – pH 7

a) Size

		Size (d.nm):	% Intensity:	St Dev (d.nm):
Z-Average (d.nm): 74.87	Peak 1:	89.74	99.5	39.53
PdI: 0.182	Peak 2:	4698	0.5	779.8
Intercept: 0.946	Peak 3:	0.000	0.0	0.000
Result quality : Good				

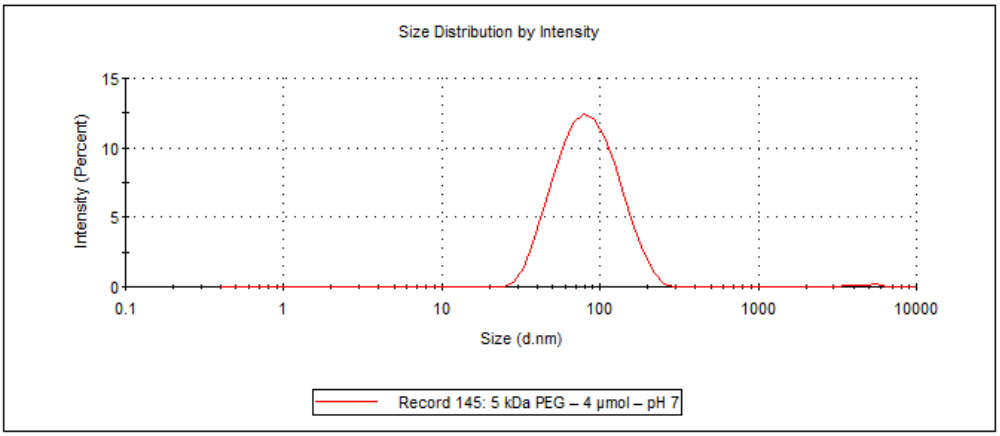

Figure A19. Size of 5 kDa PEG – 4 µmole – pH 7

b) Zeta Potential

		Mean (mV)	Area (%)	St Dev (mV)
Zeta Potential (mV): 6.79	Peak 1:	6.79	100.0	3.29
Zeta Deviation (mV): 3.03	Peak 2:	0.00	0.0	0.00
Conductivity (mS/cm): 1.35	Peak 3:	0.00	0.0	0.00
Result quality : Good				

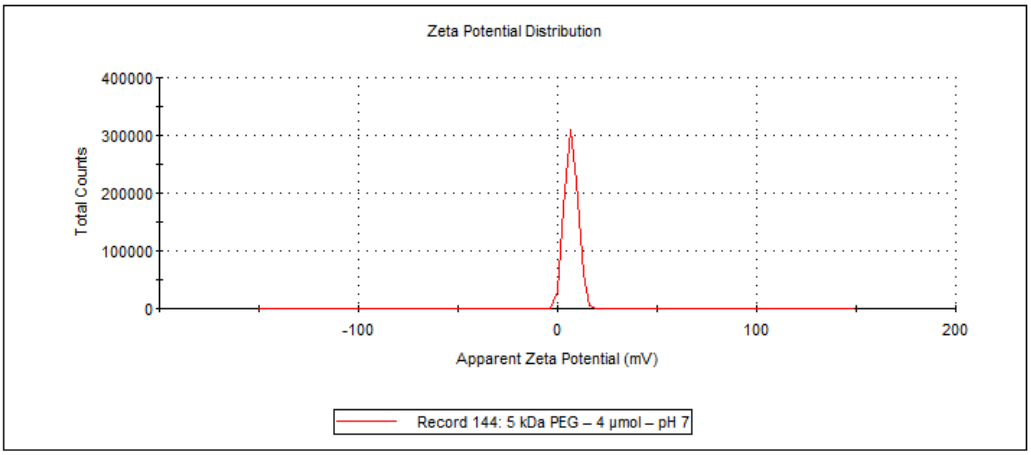

Figure A20. Zeta potential of 5 kDa PEG – 4 µmole – pH 7

11) 5 kDa PEG – 4 µmole – pH 7.4

a) Size

			Size (d.nm):	% Intensity:	St Dev (d.nm):
Z-Average (d.nm):	153.1	Peak 1:	226.5	99.1	135.8
PdI:	0.338	Peak 2:	4066	0.9	1036
Intercept:	0.343	Peak 3:	0.000	0.0	0.000
Result quality :	Good				

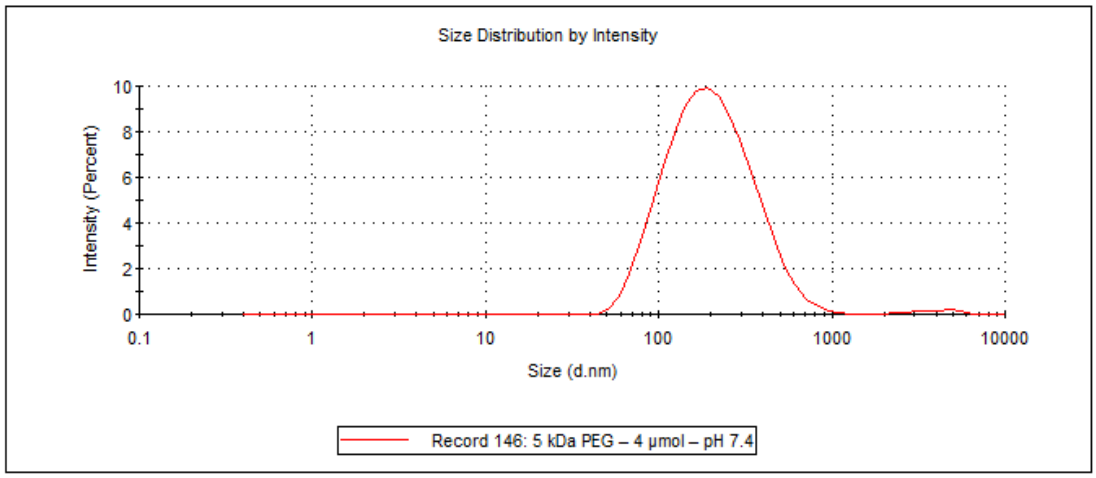

Figure A21. Size of 5 kDa PEG – 4 µmole – pH 7.4

b) Zeta Potential

			Mean (mV)	Area (%)	St Dev (mV)
Zeta Potential (mV):	3.41	Peak 1:	3.41	100.0	3.29
Zeta Deviation (mV):	2.96	Peak 2:	0.00	0.0	0.00
Conductivity (mS/cm):	1.43	Peak 3:	0.00	0.0	0.00
Result quality :	Good				

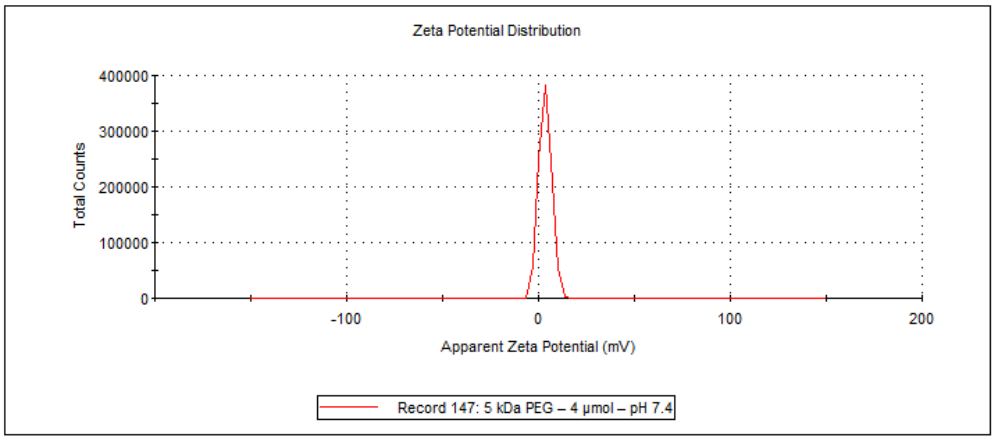

Figure A22. Zeta potential of 5 kDa PEG – 4 µmole – pH 7.4

12) 5 kDa PEG – 12 µmole – pH 6

a) Size

		Size (d.nm):	% Intensity:	St Dev (d.nm):
Z-Average (d.nm): 55.75	Peak 1:	219.8	97.3	576.4
PdI: 0.405	Peak 2:	12.57	2.7	2.213
Intercept: 0.941	Peak 3:	0.000	0.0	0.000
Result quality : Good				

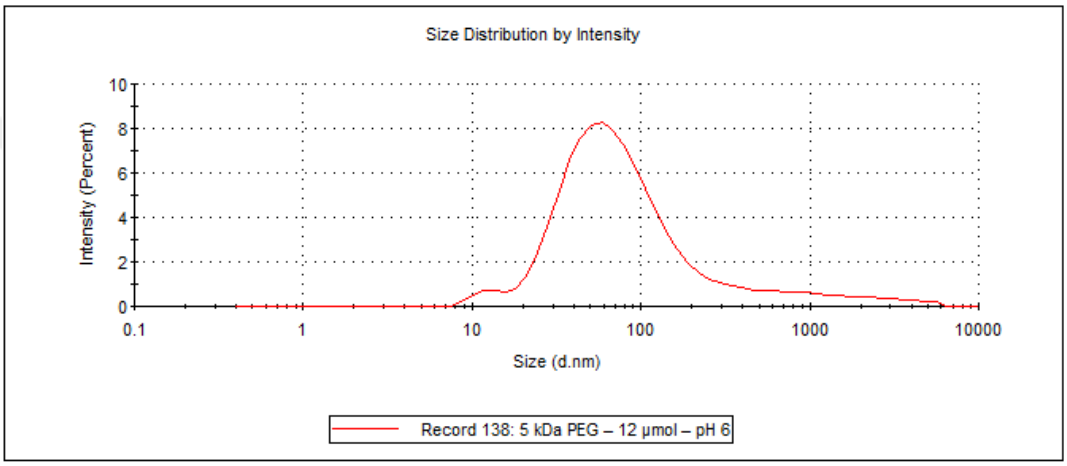

Figure A23. Size of 5 kDa PEG – 12 µmole – pH 6

b) Zeta Potential

		Mean (mV)	Area (%)	St Dev (mV)
Zeta Potential (mV): 13.2	Peak 1:	13.2	100.0	4.04
Zeta Deviation (mV): 3.86	Peak 2:	0.00	0.0	0.00
Conductivity (mS/cm): 1.25	Peak 3:	0.00	0.0	0.00
Result quality : Good				

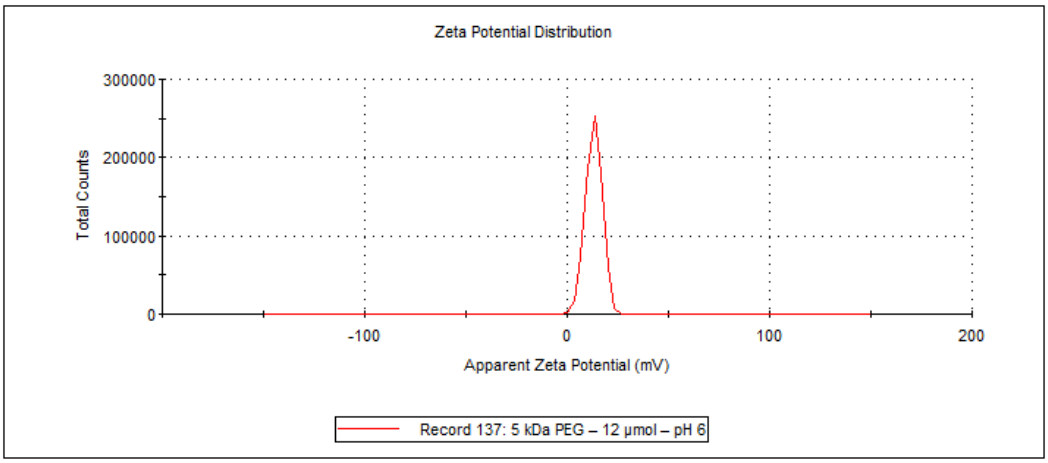

Figure A24. Zeta potential of 5 kDa PEG – 12 µmole – pH 6

13) 5 kDa PEG – 12 µmole – pH 7

a) Size

		Size (d.nm):	% Intensity:	St Dev (d.nm):
Z-Average (d.nm): 75.60	Peak 1:	89.86	98.2	42.21
PdI: 0.239	Peak 2:	4831	1.8	817.7
Intercept: 0.940	Peak 3:	0.000	0.0	0.000

Result quality : Good

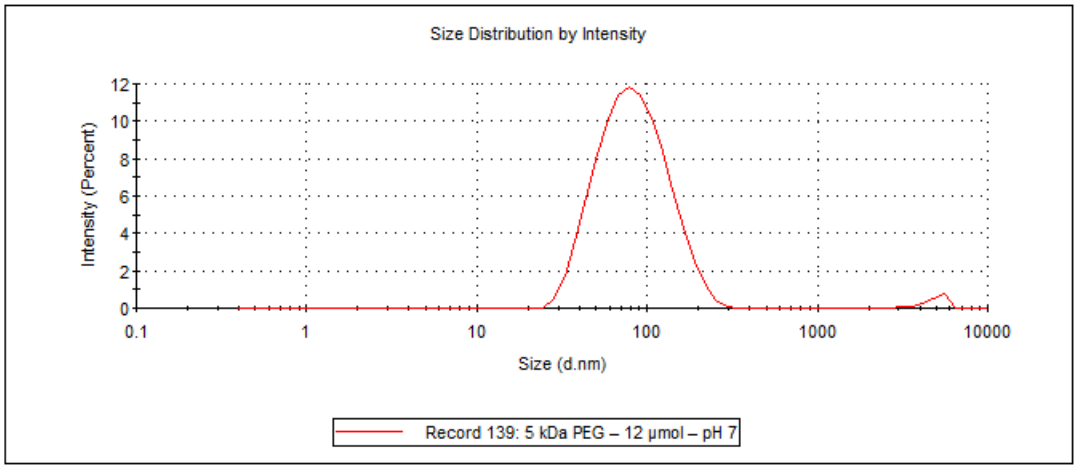

Figure A25. Size of 5 kDa PEG – 12 µmole – pH 7

b) Zeta Potential

		Mean (mV)	Area (%)	St Dev (mV)
Zeta Potential (mV): 4.75	Peak 1:	4.80	100.0	3.41
Zeta Deviation (mV): 3.16	Peak 2:	0.00	0.0	0.00
Conductivity (mS/cm): 1.40	Peak 3:	0.00	0.0	0.00

Result quality : Good

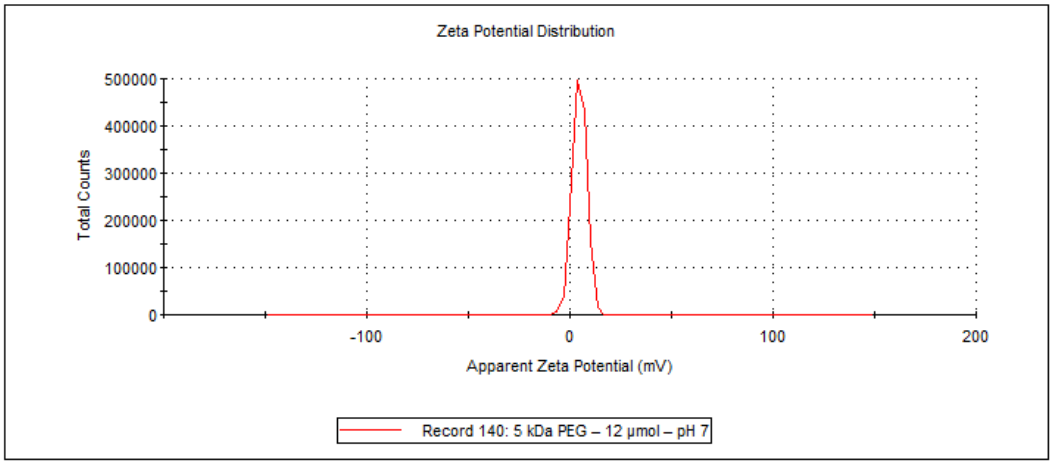

Figure A26. Zeta potential of 5 kDa PEG – 12 µmole – pH 7

14) 5 kDa PEG – 12 µmole – pH 7.4

a) Size

			Size (d.nm):	% Intensity:	St Dev (d.nm):
Z-Average (d.nm):	108.5	Peak 1:	136.6	98.4	65.48
PdI:	0.251	Peak 2:	4499	1.6	916.6
Intercept:	0.906	Peak 3:	0.000	0.0	0.000
Result quality :	Good				

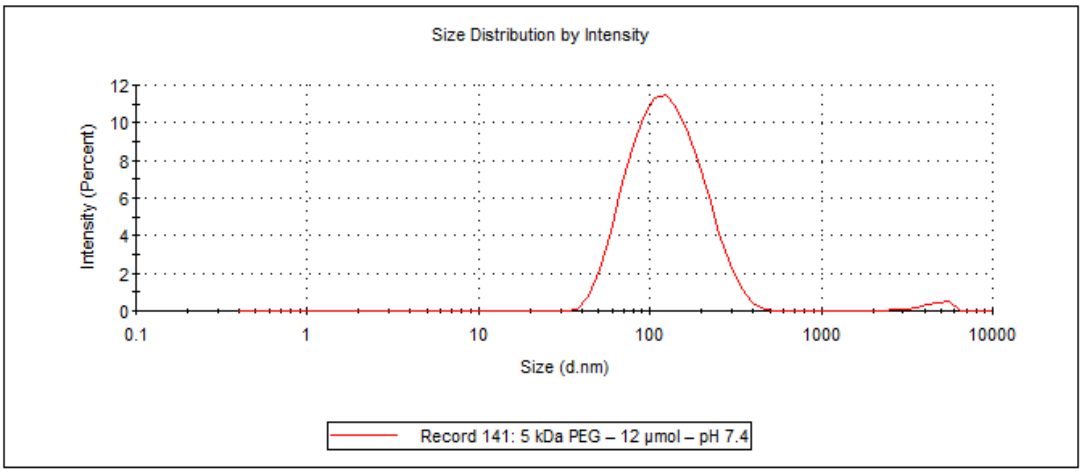

Figure A27. Size of 5 kDa PEG – 12 µmole – pH 7.**4**

b) Zeta Potential

			Mean (mV)	Area (%)	St Dev (mV)
Zeta Potential (mV):	2.61	Peak 1:	2.59	100.0	3.28
Zeta Deviation (mV):	3.11	Peak 2:	0.00	0.0	0.00
Conductivity (mS/cm):	1.47	Peak 3:	0.00	0.0	0.00
Result quality :	Good				

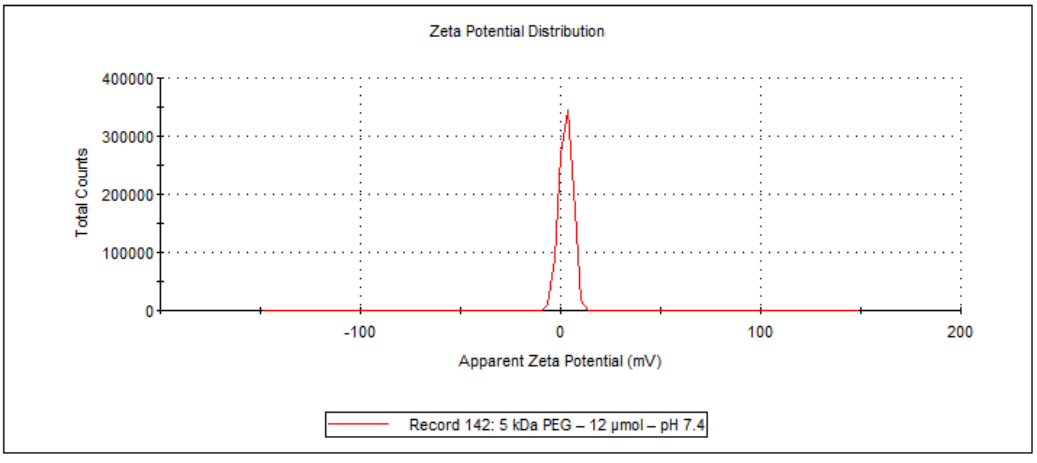

Figure A28. Zeta potential of 5 kDa PEG – 12 µmole – pH 7.4

15) 5 kDa PEG – 20 µmole – pH 6

a) Size

			Size (d.nm):	% Intensity:	St Dev (d.nm):
Z-Average (d.nm):	56.92	Peak 1:	82.59	95.9	65.22
PdI:	0.355	Peak 2:	3865	4.1	1250
Intercept:	0.934	Peak 3:	0.000	0.0	0.000
Result quality :	Good				

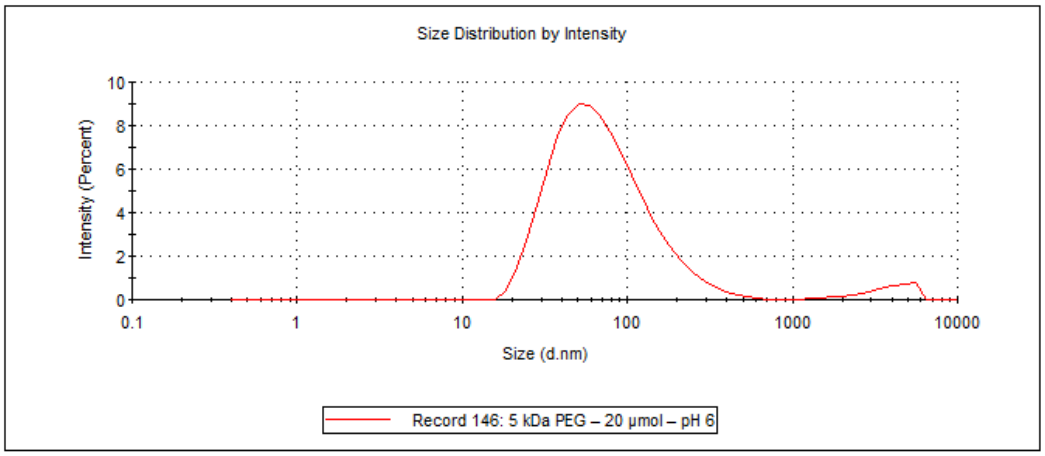

Figure A29. Size of 5 kDa PEG – 20 µmole – pH 6

b) Zeta Potential

			Mean (mV)	Area (%)	St Dev (mV)
Zeta Potential (mV):	9.44	Peak 1:	9.43	100.0	3.82
Zeta Deviation (mV):	3.52	Peak 2:	0.00	0.0	0.00
Conductivity (mS/cm):	1.37	Peak 3:	0.00	0.0	0.00
Result quality :	Good				

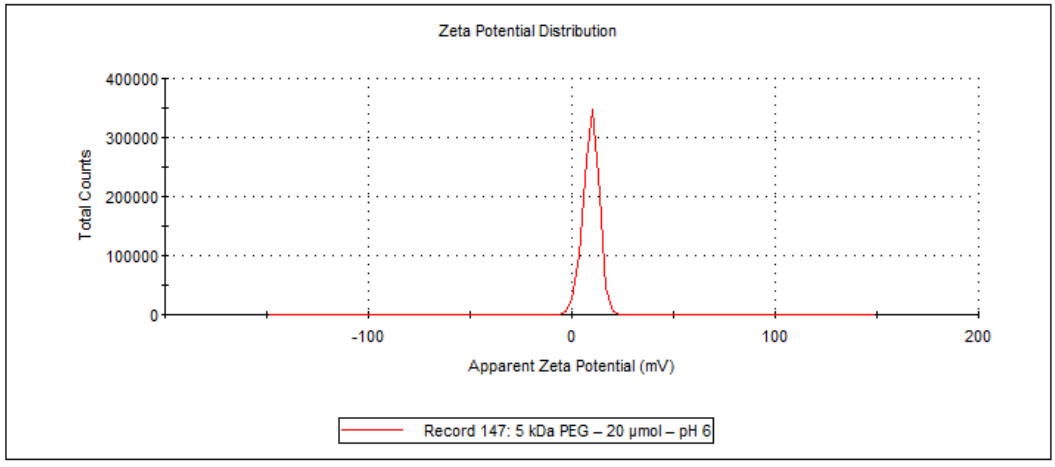

Figure A30. Zeta potential of 5 kDa PEG – 20 µmole – pH 6

16) 5 kDa PEG – 20 µmole – pH 7

a) Size

			Size (d.nm):	% Intensity:	St Dev (d.nm):
Z-Average (d.nm):	66.92	Peak 1:	84.40	95.0	44.71
PdI:	0.306	Peak 2:	3594	5.0	1318
Intercept:	0.948	Peak 3:	0.000	0.0	0.000
Result quality :	Good				

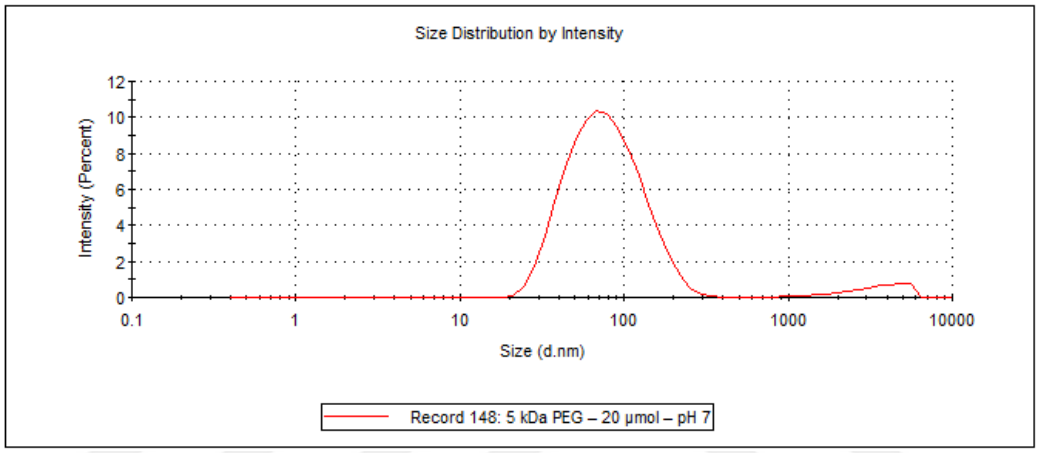

Figure A31. Size of 5 kDa PEG – 20 µmole – pH 7

b) Zeta Potential

			Mean (mV)	Area (%)	St Dev (mV)
Zeta Potential (mV):	4.18	Peak 1:	4.18	100.0	4.56
Zeta Deviation (mV):	4.22	Peak 2:	0.00	0.0	0.00
Conductivity (mS/cm):	1.63	Peak 3:	0.00	0.0	0.00
Result quality :	Good				

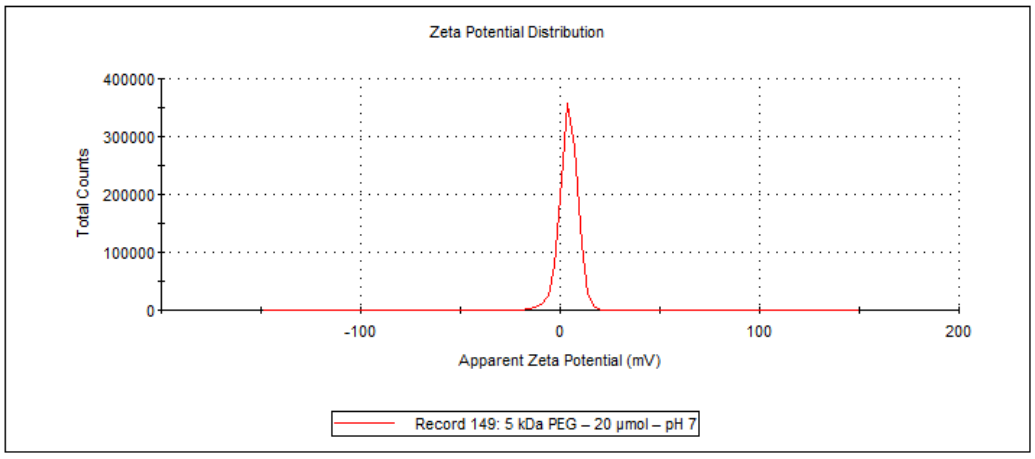

Figure A32. Zeta potential of 5 kDa PEG – 20 µmole – pH 7

17) 5 kDa PEG – 20 µmole – pH 7.4

a) Size

			Size (d.nm):	% Intensity:	St Dev (d.nm):
Z-Average (d.nm):	109.7	Peak 1:	142.8	100.0	63.84
PdI:	0.237	Peak 2:	0.000	0.0	0.000
Intercept:	0.890	Peak 3:	0.000	0.0	0.000
Result quality :	Good				

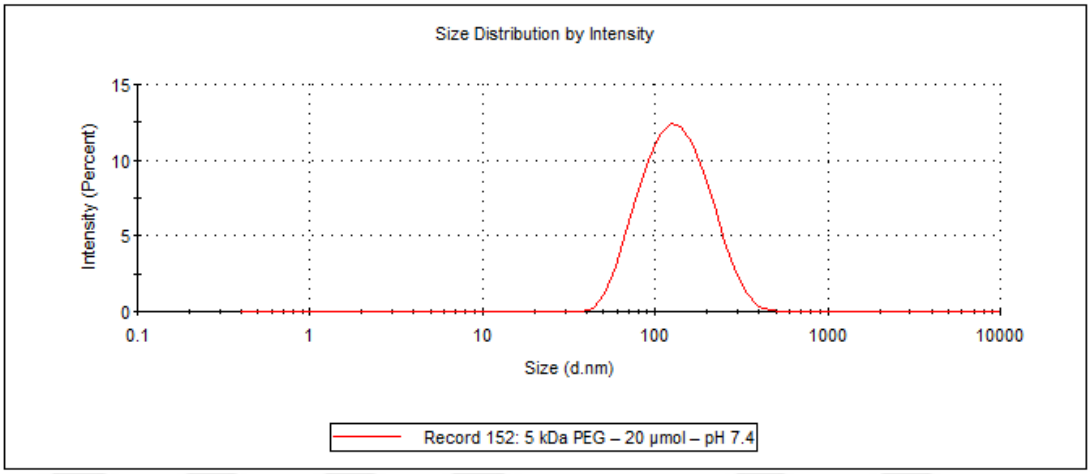

Figure A33. Size of 5 kDa PEG – 20 µmole – pH 7.4

b) Zeta Potential

			Mean (mV)	Area (%)	St Dev (mV)
Zeta Potential (mV):	2.29	Peak 1:	2.29	100.0	3.41
Zeta Deviation (mV):	3.13	Peak 2:	0.00	0.0	0.00
Conductivity (mS/cm):	1.71	Peak 3:	0.00	0.0	0.00
Result quality :	Good				

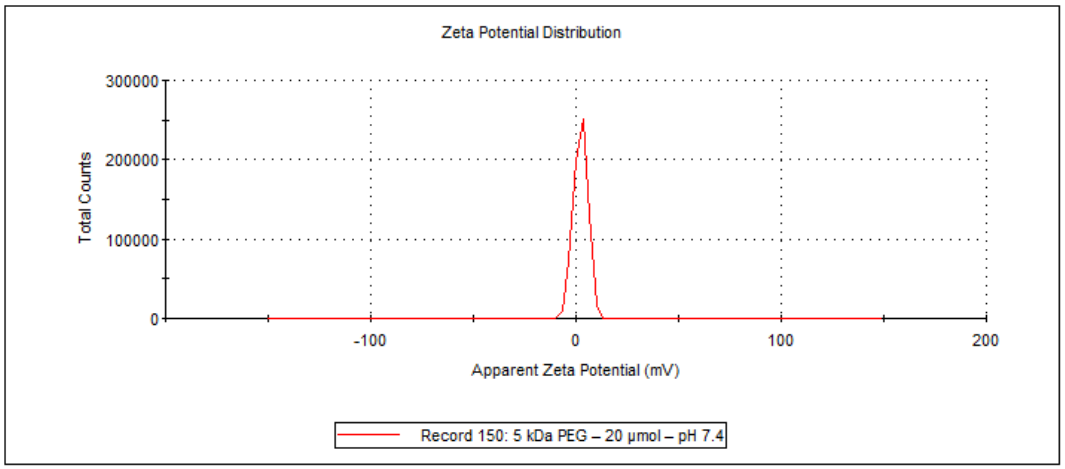

Figure A34. Zeta potential of 5 kDa PEG – 20 µmole – pH 7.4

18) 10 kDa PEG – 4 µmole – pH 6

a) Size

			Size (d.nm):	% Intensity:	St Dev (d.nm):
Z-Average (d.nm):	65.75	Peak 1:	82.57	97.5	43.51
PdI:	0.251	Peak 2:	4445	2.5	909.0
Intercept:	0.945	Peak 3:	0.000	0.0	0.000
Result quality :	Good				

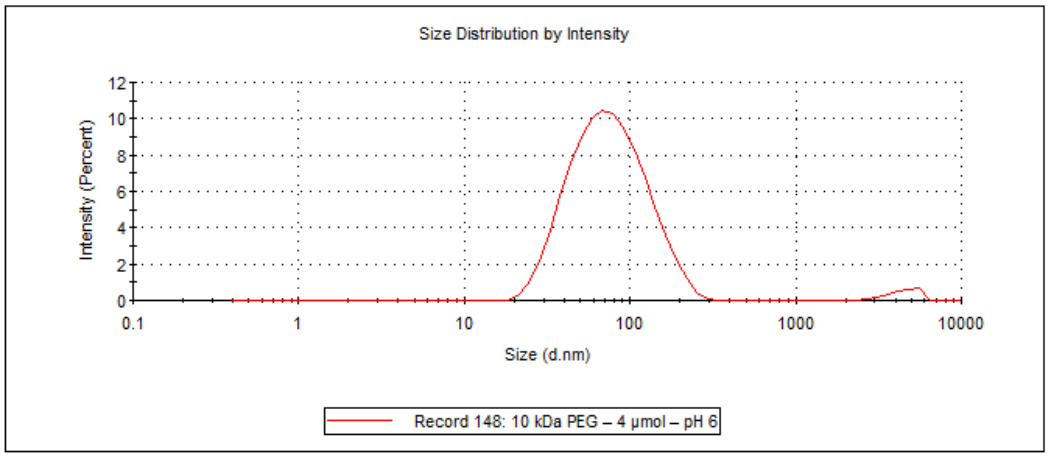

Figure A35. Size of 10 kDa PEG – 4 µmole – pH 6

b) Zeta Potential

			Mean (mV)	Area (%)	St Dev (mV)
Zeta Potential (mV):	15.5	Peak 1:	15.5	100.0	4.57
Zeta Deviation (mV):	4.38	Peak 2:	0.00	0.0	0.00
Conductivity (mS/cm):	1.17	Peak 3:	0.00	0.0	0.00
Result quality :	Good				

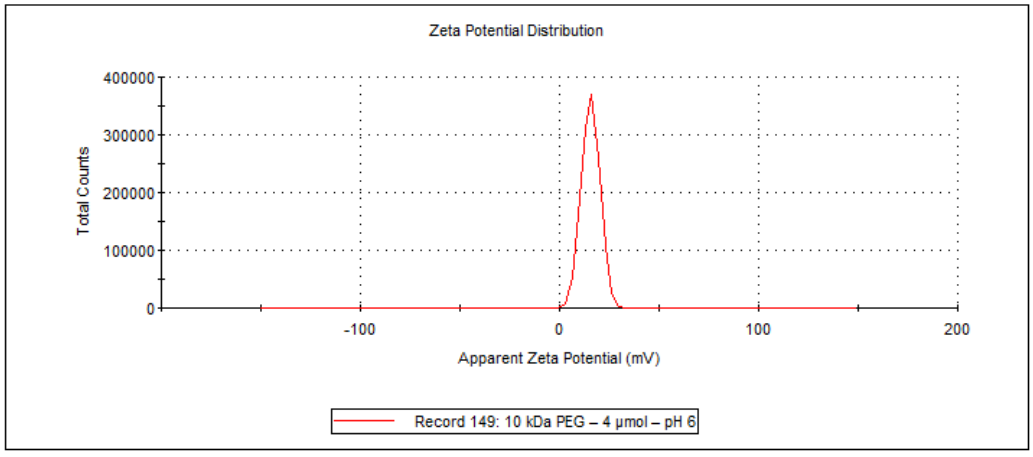

Figure A36. Zeta potential of 10 kDa PEG – 4 µmole – pH 6

19) 10 kDa PEG – 4 µmole – pH 7

a) Size

		Size (d.nm):	% Intensity:	St Dev (d.nm):
Z-Average (d.nm): 66.72	Peak 1:	81.62	100.0	36.84
PdI: 0.179	Peak 2:	0.000	0.0	0.000
Intercept: 0.941	Peak 3:	0.000	0.0	0.000

Result quality : Good

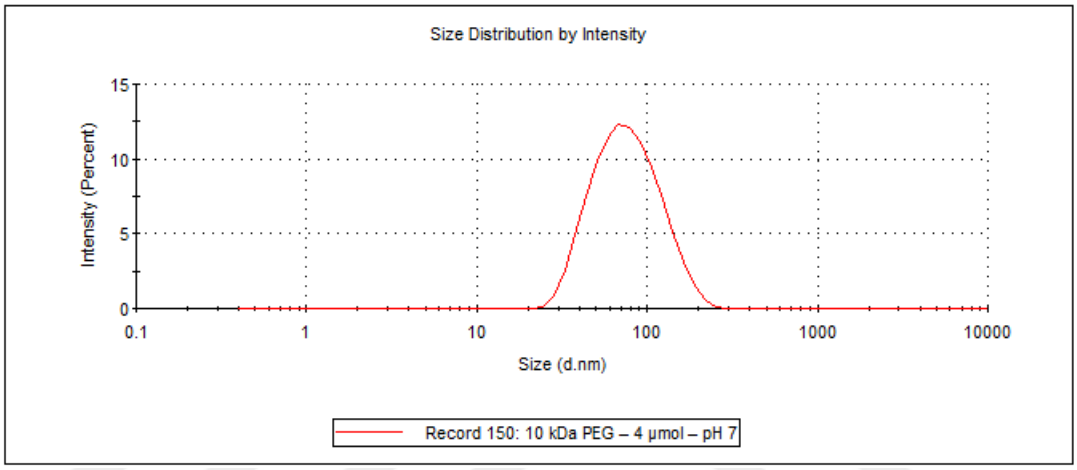

Figure A37. Size of 10 kDa PEG – 4 µmole – pH 7

b) Zeta Potential

		Mean (mV)	Area (%)	St Dev (mV)
Zeta Potential (mV): 5.05	Peak 1:	5.06	100.0	3.85
Zeta Deviation (mV): 3.50	Peak 2:	0.00	0.0	0.00
Conductivity (mS/cm): 1.33	Peak 3:	0.00	0.0	0.00

Result quality : Good

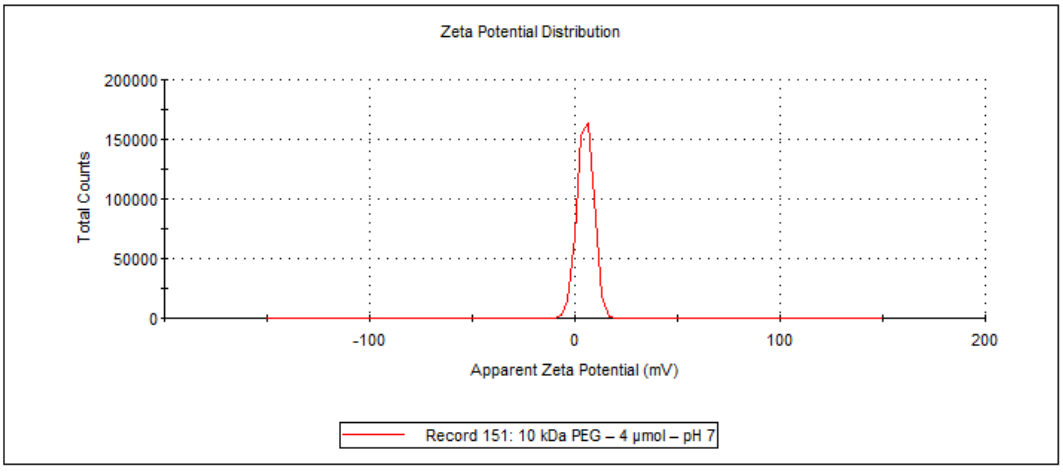

Figure A38. Zeta potential of 10 kDa PEG – 4 µmole – pH 7

20) 10 kDa PEG – 4 µmole – pH 7.4

a) Size

			Size (d.nm):	% Intensity:	St Dev (d.nm):
Z-Average (d.nm):	90.71	Peak 1:	116.4	100.0	49.26
PdI:	0.223	Peak 2:	0.000	0.0	0.000
Intercept:	0.933	Peak 3:	0.000	0.0	0.000
Result quality :	Good				

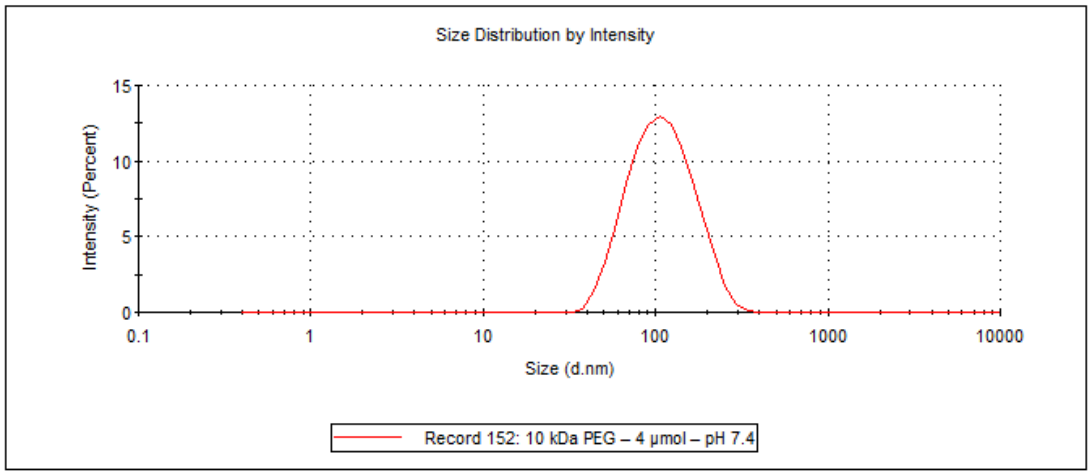

Figure A39. Size of 10 kDa PEG – 4 µmole – pH 7.4

b) Zeta Potential

			Mean (mV)	Area (%)	St Dev (mV)
Zeta Potential (mV):	3.16	Peak 1:	3.16	100.0	3.69
Zeta Deviation (mV):	3.45	Peak 2:	0.00	0.0	0.00
Conductivity (mS/cm):	1.43	Peak 3:	0.00	0.0	0.00
Result quality :	Good				

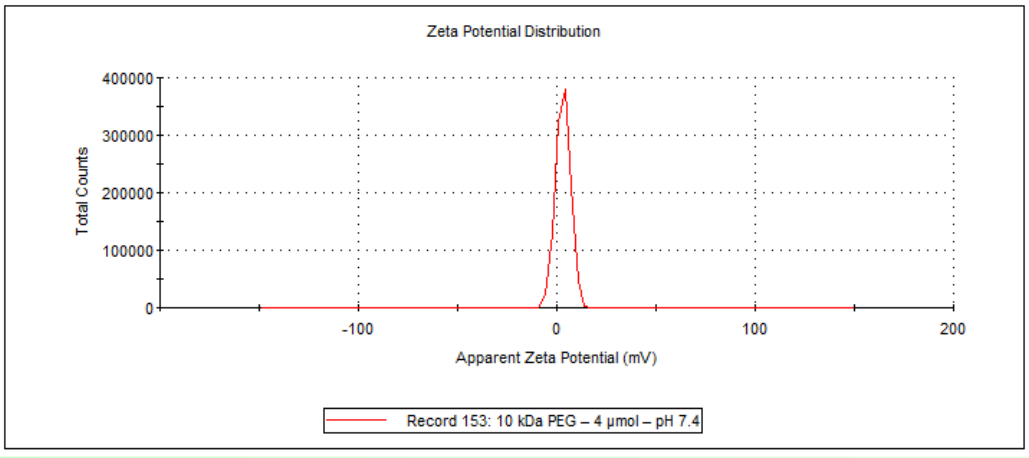

Figure A40. Zeta potential of 10 kDa PEG – 4 µmole – pH 7.4

21) 10 kDa PEG – 12 µmole – pH 6

a) Size

			Size (d.nm):	% Intensity:	St Dev (d.nm):
Z-Average (d.nm):	63.56	Peak 1:	80.49	97.8	40.23
PdI:	0.260	Peak 2:	4402	2.2	993.5
Intercept:	0.938	Peak 3:	0.000	0.0	0.000
Result quality :	Good				

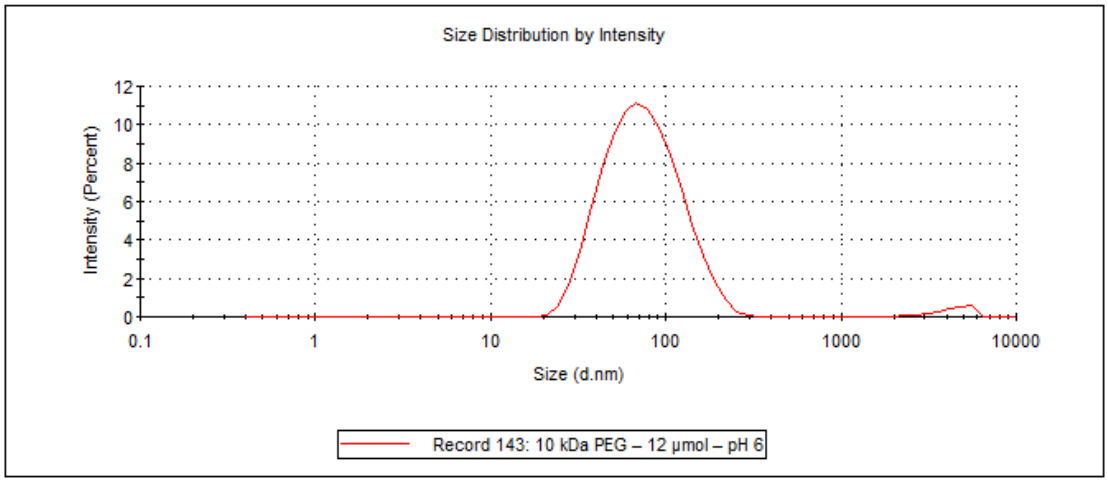

Figure A41. Size of 10 kDa PEG – 12 µmole – pH 6

b) Zeta Potential

			Mean (mV)	Area (%)	St Dev (mV)
Zeta Potential (mV):	9.57	Peak 1:	9.56	100.0	3.85
Zeta Deviation (mV):	3.56	Peak 2:	0.00	0.0	0.00
Conductivity (mS/cm):	1.15	Peak 3:	0.00	0.0	0.00
Result quality :	Good				

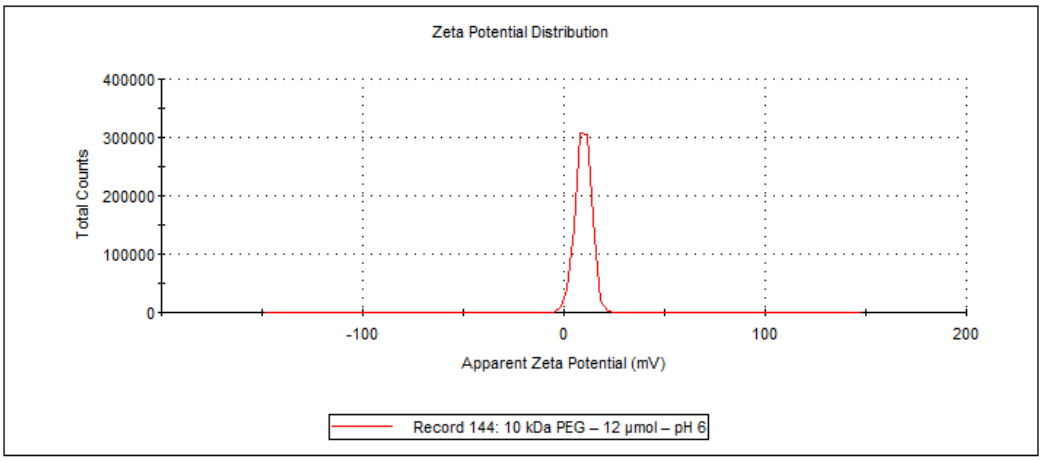

Figure A42. Zeta potential of 10 kDa PEG – 12 µmole – pH 6

22) 10 kDa PEG – 12 µmole – pH 7

a) Size

			Size (d.nm):	% Intensity:	St Dev (d.nm):
Z-Average (d.nm):	67.32	Peak 1:	82.44	96.4	39.92
PdI:	0.260	Peak 2:	4307	3.1	1033
Intercept:	0.944	Peak 3:	12.69	0.5	2.759
Result quality :	Good				

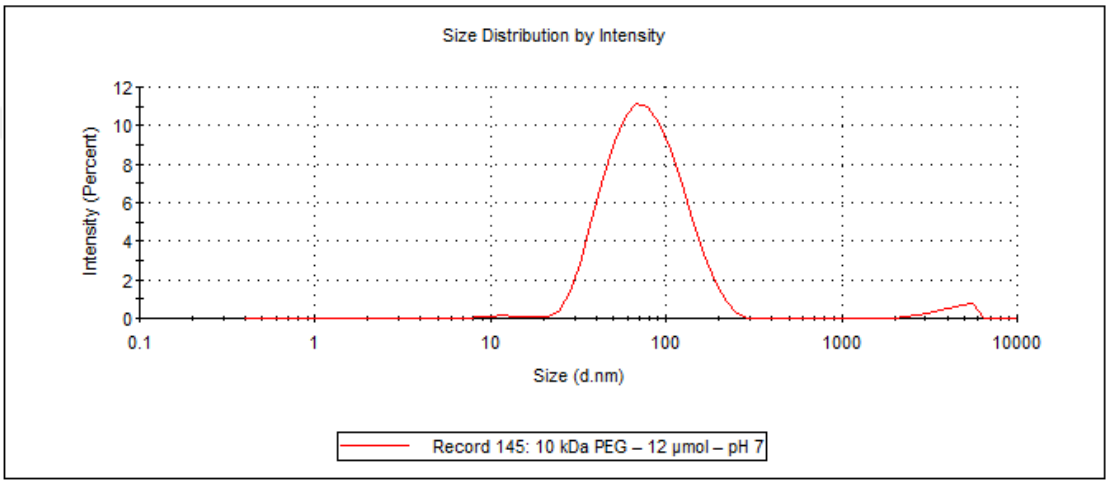

Figure A43. Size of 10 kDa PEG – 12 µmole – pH 7

b) Zeta Potential

			Mean (mV)	Area (%)	St Dev (mV)
Zeta Potential (mV):	3.65	Peak 1:	3.68	100.0	3.57
Zeta Deviation (mV):	3.35	Peak 2:	0.00	0.0	0.00
Conductivity (mS/cm):	1.24	Peak 3:	0.00	0.0	0.00
Result quality :	Good				

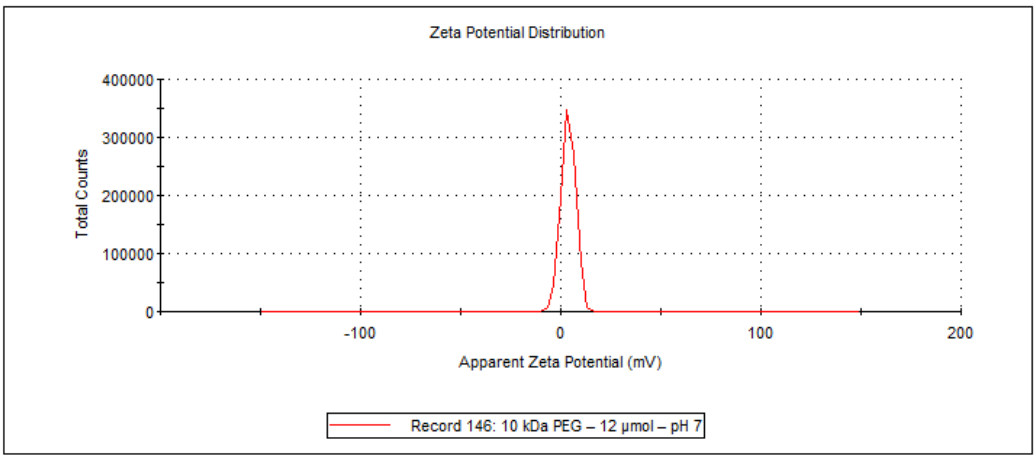

Figure A44. Zeta potential of 10 kDa PEG – 12 µmole – pH 7

23) 10 kDa PEG – 12 µmole – pH 7.4

a) Size

			Size (d.nm):	% Intensity:	St Dev (d.nm):
Z-Average (d.nm):	112.6	Peak 1:	155.9	99.6	80.07
PdI:	0.266	Peak 2:	23.27	0.4	3.844
Intercept:	0.945	Peak 3:	0.000	0.0	0.000
Result quality :	Good				

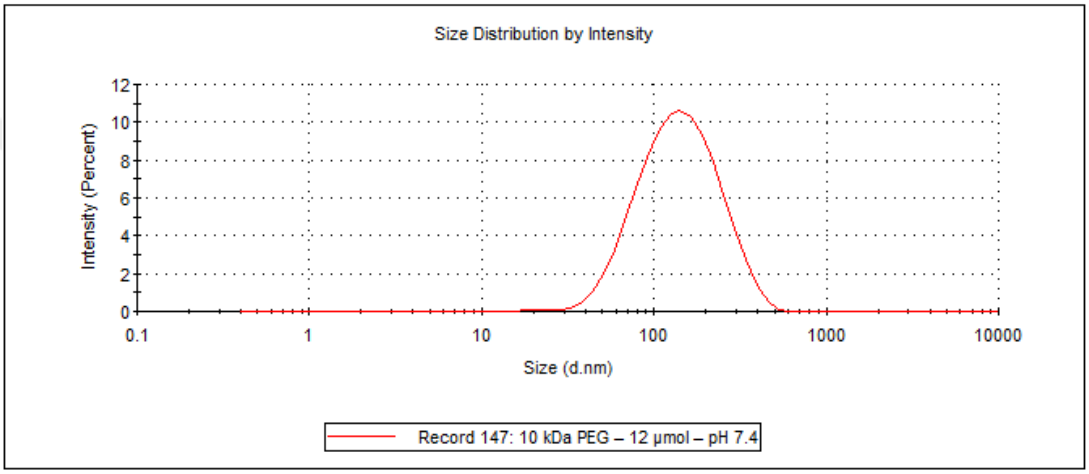

Figure A45. Size of 10 kDa PEG – 12 µmole – pH 7.4

b) Zeta Potential

			Mean (mV)	Area (%)	St Dev (mV)
Zeta Potential (mV):	2.47	Peak 1:	2.46	100.0	3.36
Zeta Deviation (mV):	3.05	Peak 2:	0.00	0.0	0.00
Conductivity (mS/cm):	1.32	Peak 3:	0.00	0.0	0.00
Result quality :	Good				

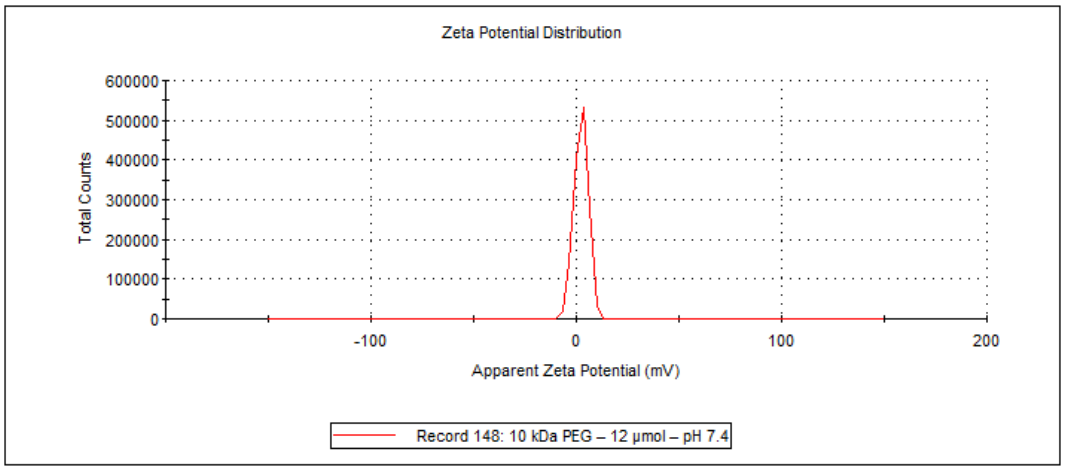

Figure A46. Zeta potential of 10 kDa PEG – 12 µmole – pH 7.4

24) 10 kDa PEG – 20 µmole – pH 6

a) Size

		Size (d.nm):	% Intensity:	St Dev (d.nm):
Z-Average (d.nm): 55.79	Peak 1:	70.17	97.3	33.68
PdI: 0.265	Peak 2:	4544	2.7	865.9
Intercept: 0.948	Peak 3:	0.000	0.0	0.000
Result quality : Good				

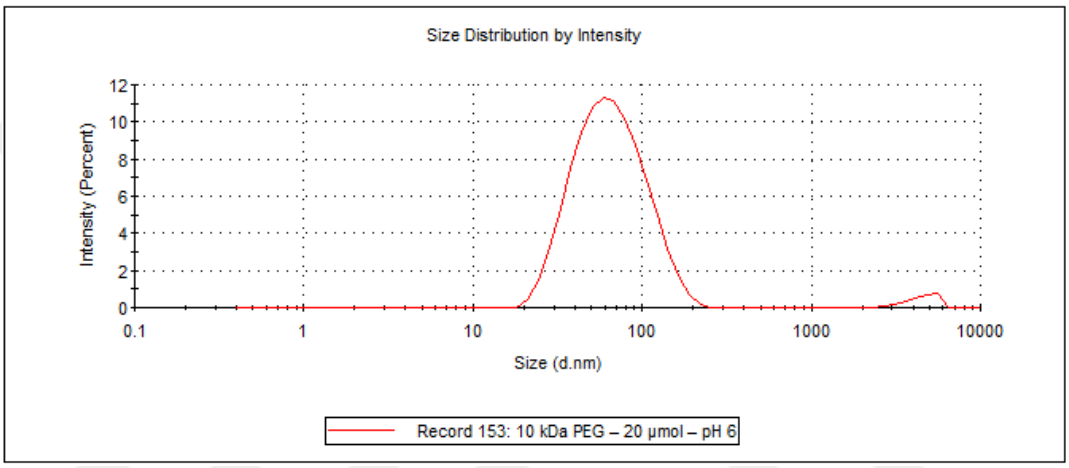

Figure A47. Size of 10 kDa PEG – 20 µmole – pH 6

b) Zeta Potential

		Mean (mV)	Area (%)	St Dev (mV)
Zeta Potential (mV): 3.28	Peak 1:	3.26	100.0	3.38
Zeta Deviation (mV): 3.04	Peak 2:	0.00	0.0	0.00
Conductivity (mS/cm): 1.28	Peak 3:	0.00	0.0	0.00
Result quality : Good				

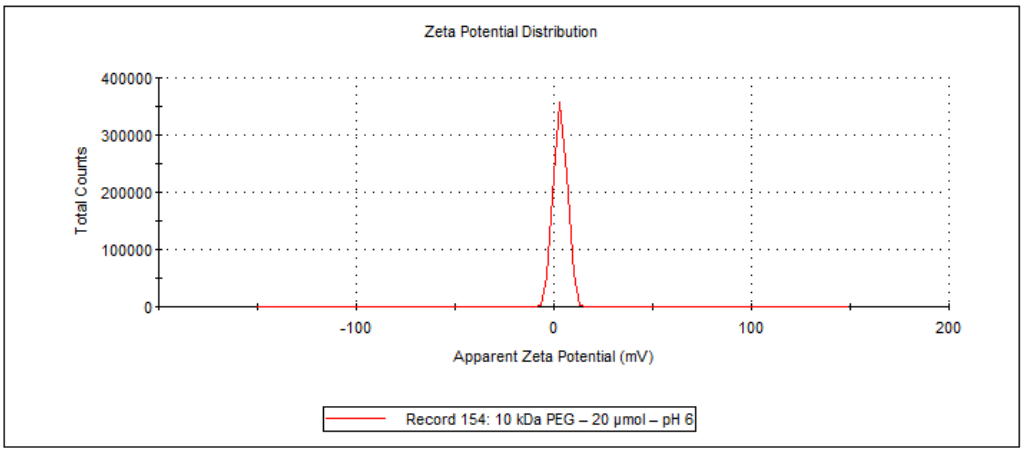

Figure A48. Zeta potential of 10 kDa PEG – 20 µmole – pH 6

25) 10 kDa PEG – 20 µmole – pH 7

a) Size

		Size (d.nm):	% Intensity:	St Dev (d.nm):
Z-Average (d.nm): 70.26	Peak 1:	95.15	98.6	47.85
PdI: 0.278	Peak 2:	4710	0.9	832.5
Intercept: 0.950	Peak 3:	16.94	0.5	2.857
Result quality : Good				

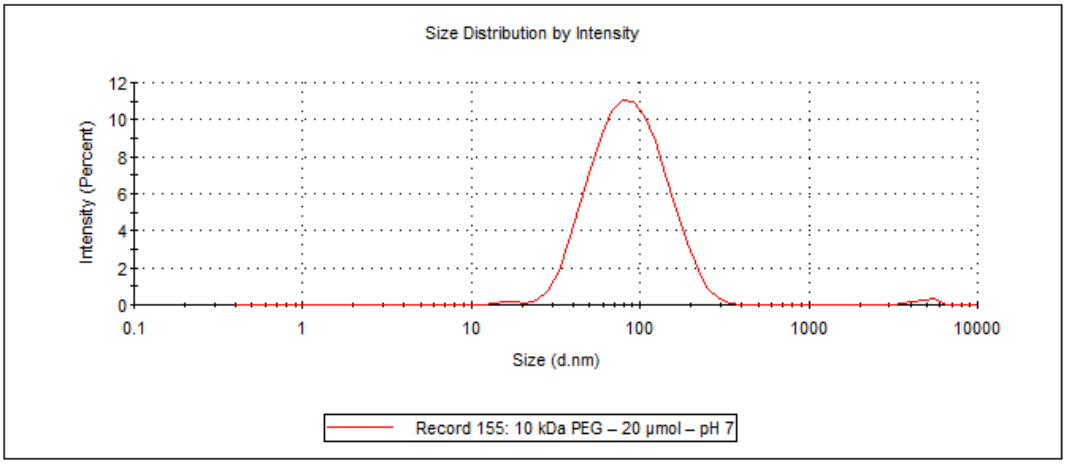

Figure A49. Size of 10 kDa PEG – 20 µmole – pH 7

b) Zeta Potential

		Mean (mV)	Area (%)	St Dev (mV)
Zeta Potential (mV): 2.36	Peak 1:	2.41	100.0	3.60
Zeta Deviation (mV): 3.33	Peak 2:	0.00	0.0	0.00
Conductivity (mS/cm): 1.35	Peak 3:	0.00	0.0	0.00
Result quality : Good				

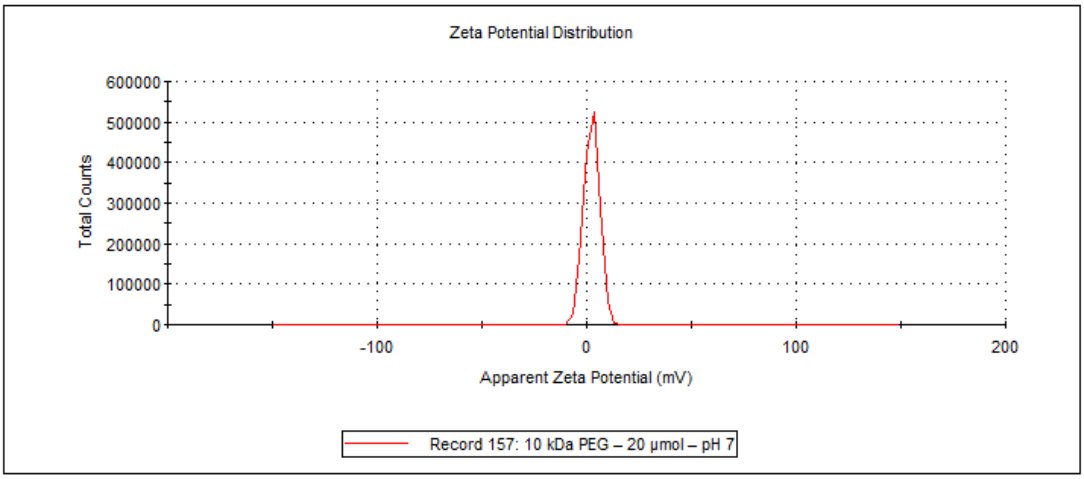

Figure A50. Zeta potential of 10 kDa PEG – 20 µmole – pH 7

26) 10 kDa PEG – 20 µmole – pH 7.4

a) Size

			Size (d.nm):	% Intensity:	St Dev (d.nm):
Z-Average (d.nm):	91.90	Peak 1:	132.5	98.4	74.85
PdI:	0.316	Peak 2:	4660	1.6	803.0
Intercept:	0.952	Peak 3:	0.000	0.0	0.000

Result quality : Refer to quality report

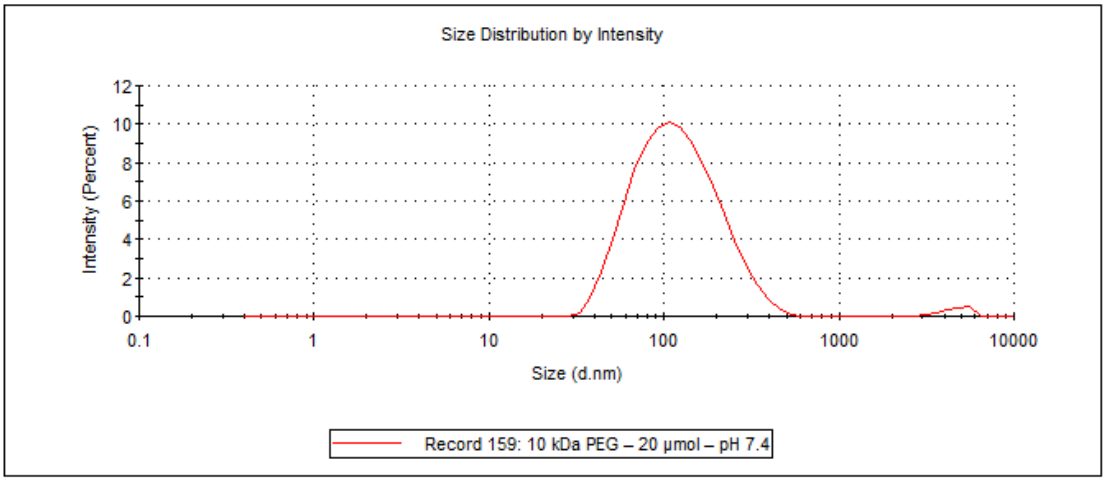

Figure A51. Size of 10 kDa PEG – 20 µmole – pH 7.4

b) Zeta Potential

			Mean (mV)	Area (%)	St Dev (mV)
Zeta Potential (mV):	2.23	Peak 1:	2.18	100.0	3.43
Zeta Deviation (mV):	3.14	Peak 2:	0.00	0.0	0.00
Conductivity (mS/cm):	1.44	Peak 3:	0.00	0.0	0.00

Result quality : Good

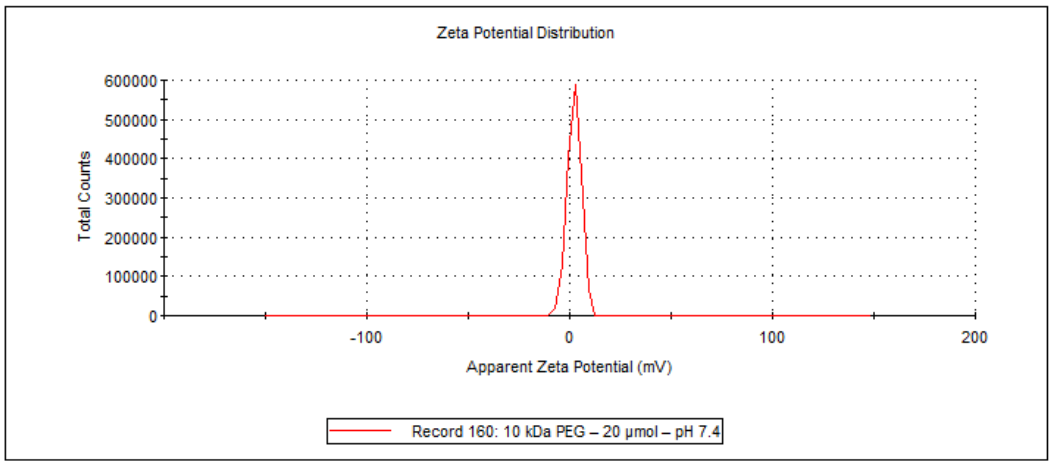

Figure A52. Zeta potential of 10 kDa PEG – 20 µmole – pH 7.4

RAW DLS RESULTS FOR TEST DATA.

27) 5 kDa PEG – 12 µmole – pH 6.5

a) Size

		Size (d.nm):	% Intensity:	St Dev (d.nm):
Z-Average (d.nm): 55.35	Peak 1:	64.27	91.0	34.49
PdI: 0.284	Peak 2:	901.1	5.9	502.2
Intercept: 0.914	Peak 3:	3450	3.1	1128
Result quality : Good				

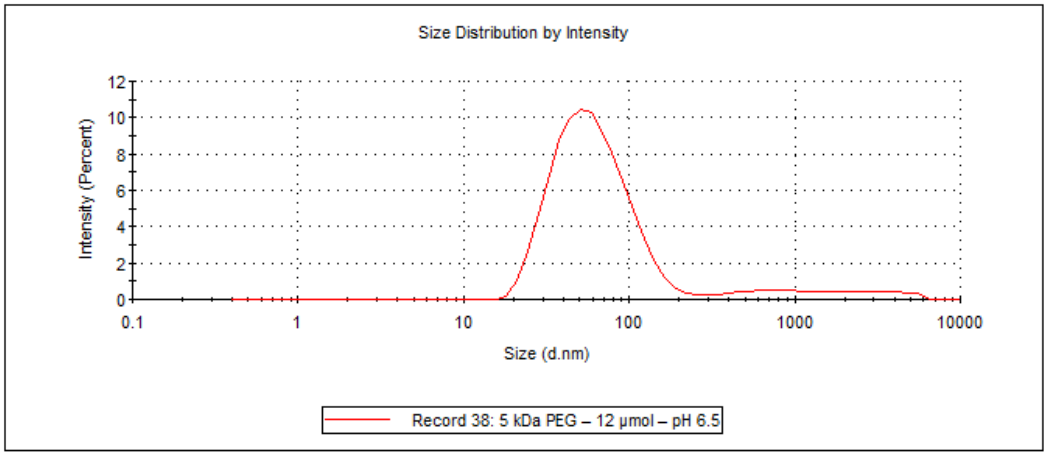

Figure A53. Size of 5 kDa PEG – 12 µmole – pH 6.5

b) Zeta Potential

		Mean (mV)	Area (%)	St Dev (mV)
Zeta Potential (mV): 6.87	Peak 1:	6.86	100.0	3.68
Zeta Deviation (mV): 3.39	Peak 2:	0.00	0.0	0.00
Conductivity (mS/cm): 1.34	Peak 3:	0.00	0.0	0.00
Result quality : Good				

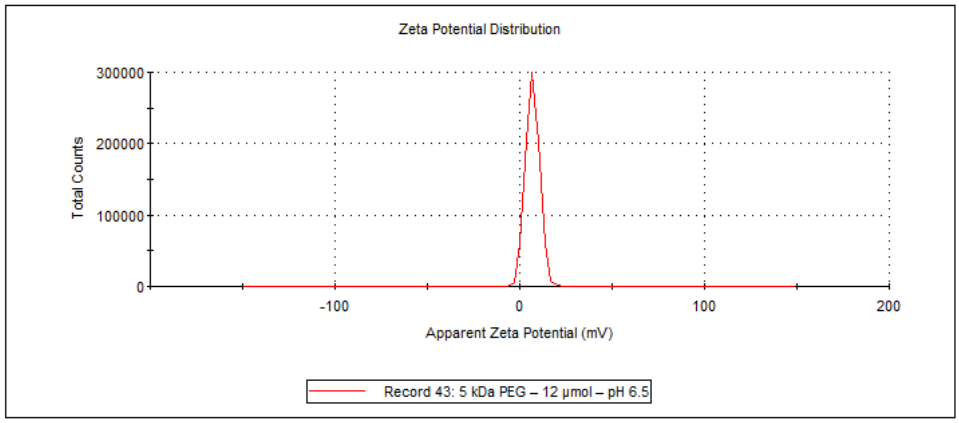

Figure A54. Zeta potential of 5 kDa PEG – 12 µmole – pH 6.5

28) 10 kDa PEG – 4 µmole – pH 6.3

a) Size

			Size (d.nm):	% Intensity:	St Dev (d.nm):
Z-Average (d.nm):	63.41	Peak 1:	76.38	97.0	40.49
PdI:	0.234	Peak 2:	4237	3.0	1011
Intercept:	0.943	Peak 3:	0.000	0.0	0.000
Result quality :	Good				

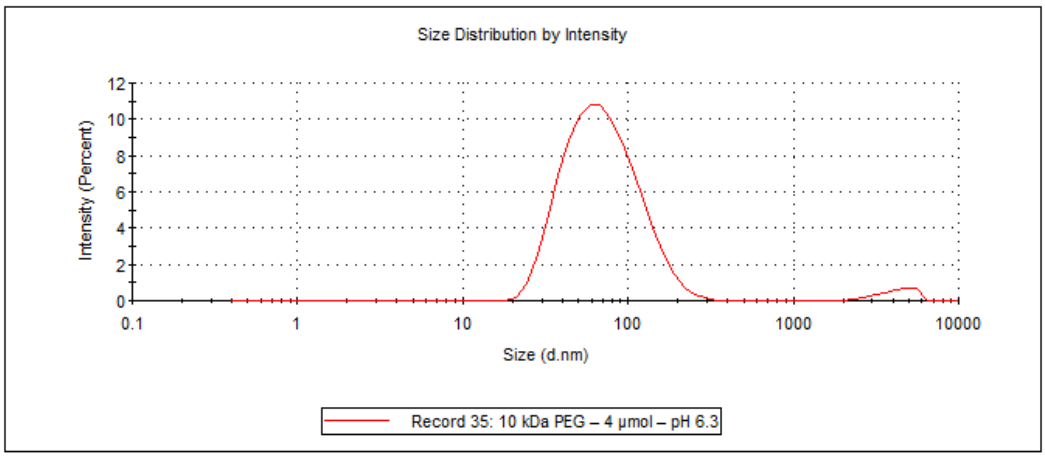

Figure A55. Size of 10 kDa PEG – 4 µmole – pH 6.3

b) Zeta Potential

			Mean (mV)	Area (%)	St Dev (mV)
Zeta Potential (mV):	9.50	Peak 1:	9.50	100.0	3.60
Zeta Deviation (mV):	3.33	Peak 2:	0.00	0.0	0.00
Conductivity (mS/cm):	1.34	Peak 3:	0.00	0.0	0.00
Result quality :	Good				

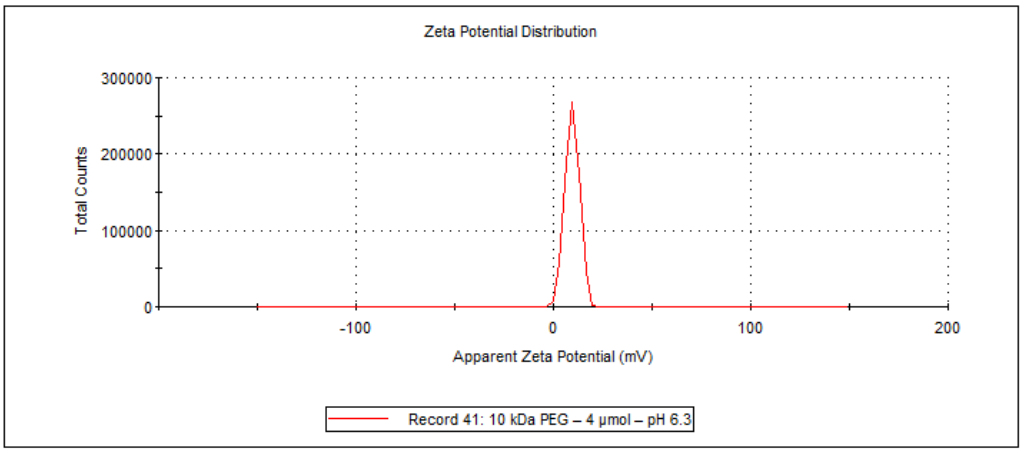

Figure A56. Zeta potential of 10 kDa PEG – 4 µmole – pH 6.3

29) 2 kDa PEG – 15 µmole – pH 6.4

a) Size

			Size (d.nm):	% Intensity:	St Dev (d.nm):
Z-Average (d.nm):	60.36	Peak 1:	69.01	95.8	33.84
PdI:	0.222	Peak 2:	3866	4.2	1146
Intercept:	0.950	Peak 3:	0.000	0.0	0.000
Result quality :	Good				

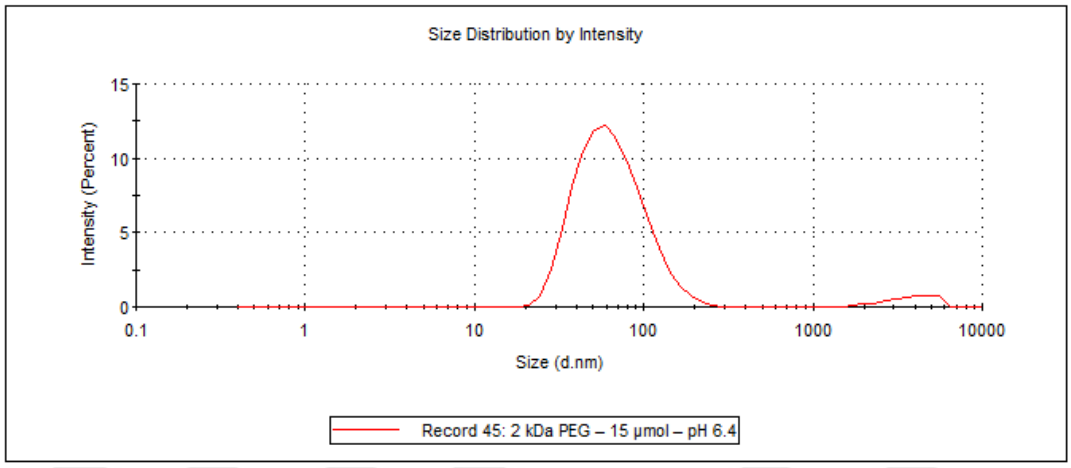

Figure A57. Size of 2 kDa PEG – 15 µmole – pH 6.4

b) Zeta Potential

			Mean (mV)	Area (%)	St Dev (mV)
Zeta Potential (mV):	8.68	Peak 1:	8.67	100.0	3.49
Zeta Deviation (mV):	3.29	Peak 2:	0.00	0.0	0.00
Conductivity (mS/cm):	1.23	Peak 3:	0.00	0.0	0.00
Result quality :	Good				

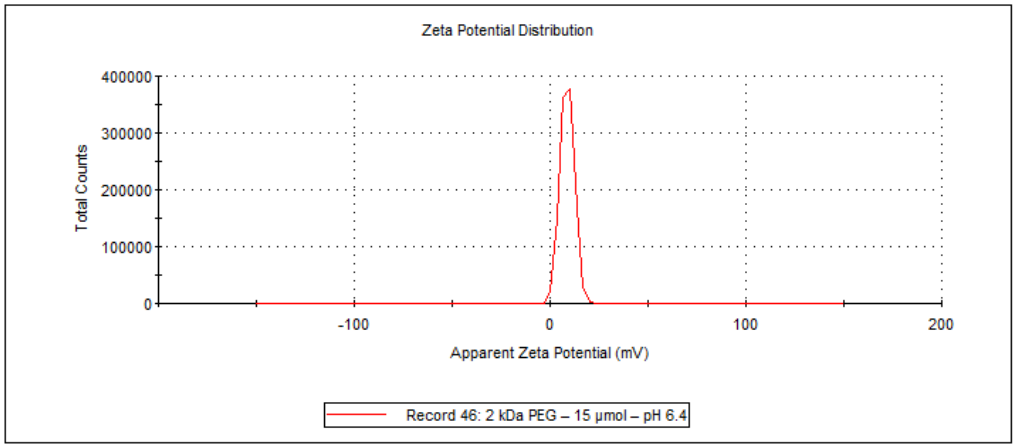

Figure A58. Zeta potential of 2 kDa PEG – 15 µmole – pH 6.4

30) 5 kDa PEG – 8 µmole – pH 7.2

a) Size

		Size (d.nm):	% Intensity:	St Dev (d.nm):
Z-Average (d.nm): 74.82	Peak 1:	88.81	98.6	41.10
PdI: 0.203	Peak 2:	4458	1.4	912.8
Intercept: 0.938	Peak 3:	0.000	0.0	0.000
Result quality : Good				

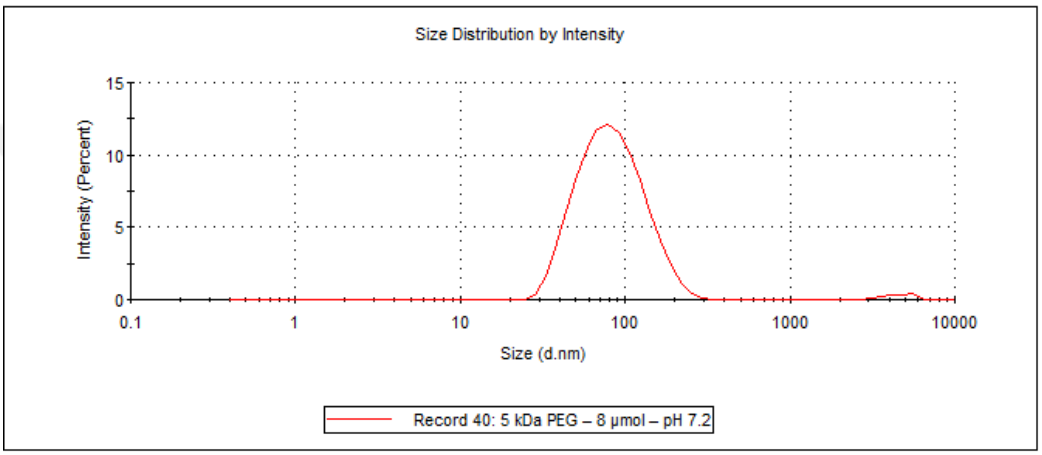

Figure A59. Size of 5 kDa PEG – 8 µmole – pH 7.2

b) Zeta Potential

		Mean (mV)	Area (%)	St Dev (mV)
Zeta Potential (mV): 5.08	Peak 1:	5.08	100.0	3.42
Zeta Deviation (mV): 3.34	Peak 2:	0.00	0.0	0.00
Conductivity (mS/cm): 1.51	Peak 3:	0.00	0.0	0.00
Result quality : Good				

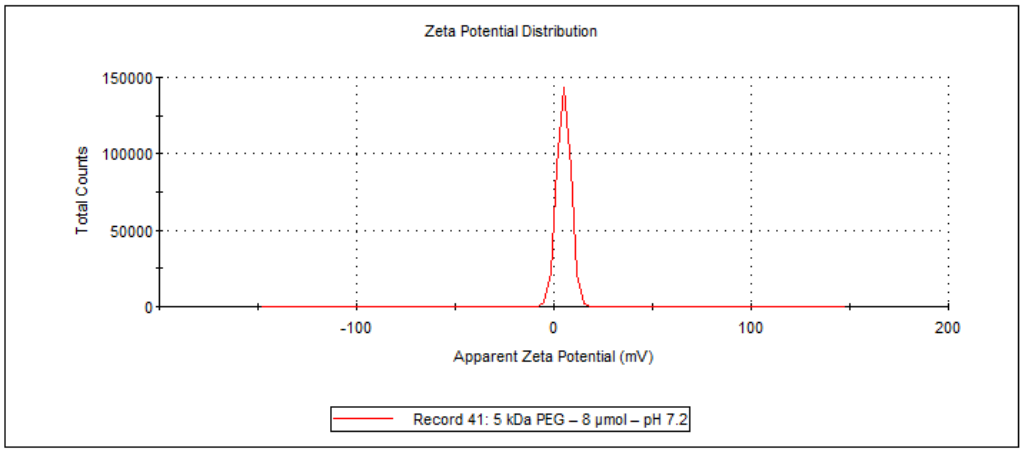

Figure A60. Zeta potential of 5 kDa PEG – 8 µmole – pH 7.2

31) 5 kDa PEG – 8 µmole – pH 6.5

a) Size

			Size (d.nm):	% Intensity:	St Dev (d.nm):
Z-Average (d.nm):	54.11	Peak 1:	65.21	99.5	31.43
PdI:	0.193	Peak 2:	4703	0.5	777.2
Intercept:	0.947	Peak 3:	0.000	0.0	0.000
Result quality :	Good				

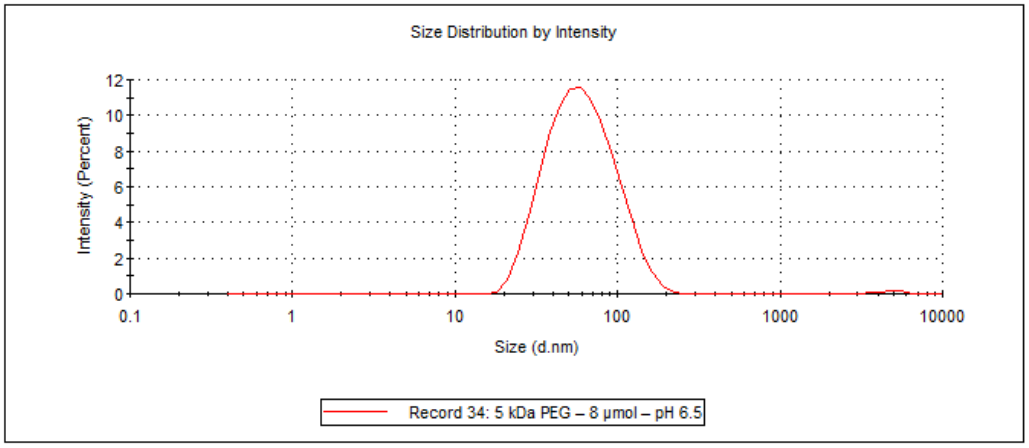

Figure A61. Size of 5 kDa PEG – 8 µmole – pH 6.5

b) Zeta Potential

			Mean (mV)	Area (%)	St Dev (mV)
Zeta Potential (mV):	7.67	Peak 1:	7.69	100.0	3.31
Zeta Deviation (mV):	3.07	Peak 2:	0.00	0.0	0.00
Conductivity (mS/cm):	1.41	Peak 3:	0.00	0.0	0.00
Result quality :	Good				

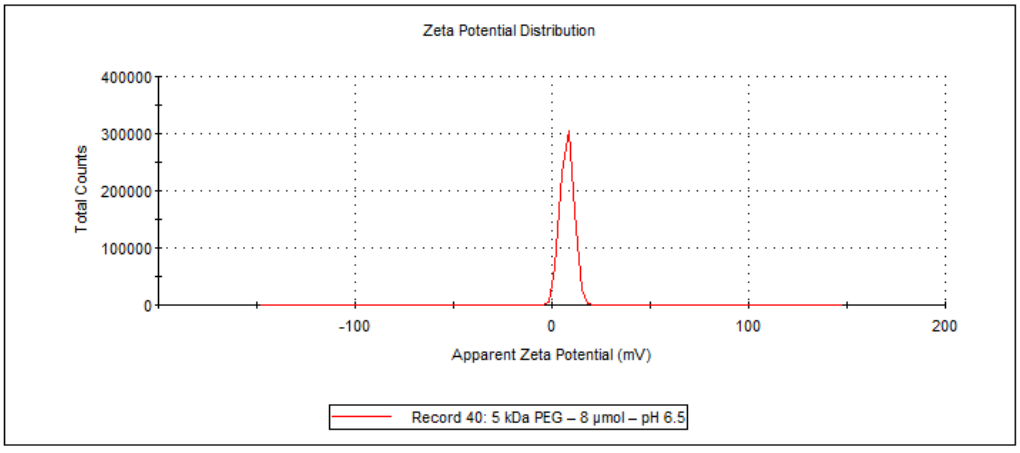

Figure A62. Zeta potential of 5 kDa PEG – 8 µmole – pH 6.5

ADDITIONAL DATA FOR CELL ATTACHMENT EXPERIMENTS

1) 2 kDa PEG – 12 µmole – pH 6.5

a) Zeta Potential

		Mean (mV)	Area (%)	St Dev (mV)
Zeta Potential (mV): 8.35	Peak 1:	8.32	100.0	4.89
Zeta Deviation (mV): 4.76	Peak 2:	0.00	0.0	0.00
Conductivity (mS/cm): 1.50	Peak 3:	0.00	0.0	0.00

Result quality : Good

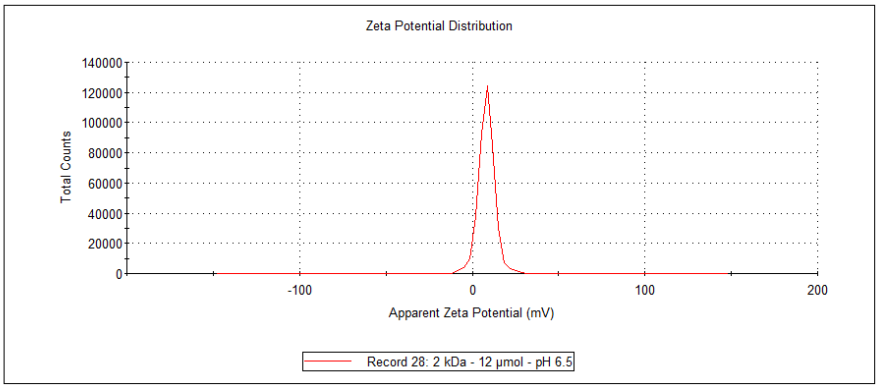

Figure A63. Zeta potential of 2 kDa PEG – 12 µmole – pH 6.5

2) 10 kDa PEG – 12 µmole – pH 6.5

b) Zeta Potential

		Mean (mV)	Area (%)	St Dev (mV)
Zeta Potential (mV): 4.94	Peak 1:	4.94	100.0	3.10
Zeta Deviation (mV): 2.89	Peak 2:	0.00	0.0	0.00
Conductivity (mS/cm): 1.40	Peak 3:	0.00	0.0	0.00

Result quality : Good

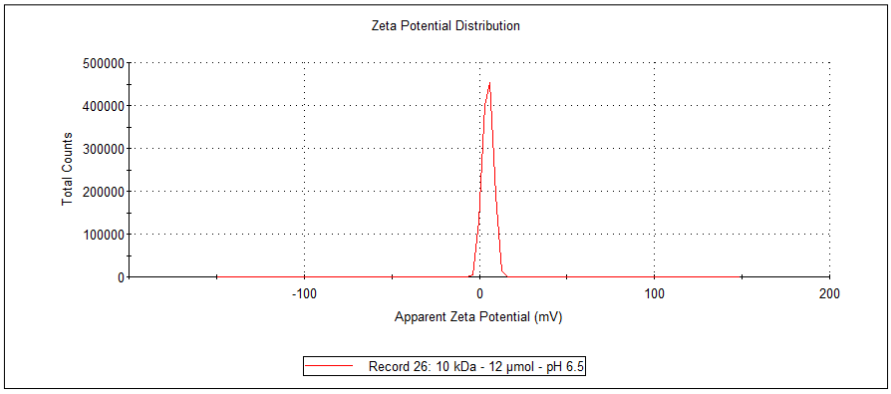

Figure A64. Zeta potential of 10 kDa PEG – 12 µmole – pH 6.5

APPENDIX B - MATLAB CODE USED FOR ANN

MATLAB CODE FOR SIZE

```
clc
clear
rng('default') % to initialize weights

x =
[4,2,6;4,2,7;4,5,6;4,5,7;4,5,7.400000000000000;4,10,6;4
,10,7;4,10,7.400000000000000;12,2,6;12,2,7;12,2,7.40000
000000000;12,5,6;12,5,7;12,5,7.400000000000000;12,10,6;
12,10,7;12,10,7.400000000000000;20,2,6;20,2,7;20,2,7.40
000000000000;20,5,6;20,5,7;20,5,7.400000000000000;20,10
,6;20,10,7;20,10,7.400000000000000;8,5,6.500000000000000
;8,5,7.200000000000000;4,10,6.300000000000000;15,2,6.400
00000000000;12,5,6.500000000000000]';
t =
[75.7100000000000;72.0900000000000;72.4000000000000;74
.8700000000000;153.130000000000;65.7500000000000;66.72
00000000000;90.7100000000000;72.7400000000000;75.01;10
8.600000000000;55.7500000000000;75.6000000000000;108.5
00000000000;63.5600000000000;67.3200000000000;112.6300
00000000;57.5000000000000;71.5500000000000;112.8000000
00000;56.9200000000000;66.9200000000000;109.7000000000
00;55.7900000000000;70.2600000000000,;91.900000000000;
54.1100000000000;74.8200000000000;63.4100000000000;60.
3600000000000;55.3500000000000]';

trainFcn = 'trainlm';  % Levenberg-Marquardt
backpropagation.

hiddenLayerSize =1;

net = fitnet(hiddenLayerSize,trainFcn);

net.input.processFcns =
{'removeconstantrows','mapminmax'};
net.output.processFcns =
{'removeconstantrows','mapminmax'};
net.divideFcn = 'divideind';
net.divideMode = 'sample';
net.divideParam.trainInd = 1:26;
```

```
 net.divideParam.testInd = 27:31;

net.performFcn = 'mse';  % Mean Squared Error

net.plotFcns =
{'plotperform','plottrainstate','ploterrhist', ...
    'plotregression', 'plotfit'};

[net,tr] = train(net,x,t);

y = net(x);
e = gsubtract(t,y);
performance = perform(net,t,y)

trainTargets = t .* tr.trainMask{1};
valTargets = t .* tr.valMask{1};
testTargets = t .* tr.testMask{1};
trainPerformance = perform(net,trainTargets,y)
valPerformance = perform(net,valTargets,y)
testPerformance = perform(net,testTargets,y)

if (false)
    % Generate MATLAB function for neural network for
application
    % deployment in MATLAB scripts or with MATLAB
Compiler and Builder
    % tools, or simply to examine the calculations
your trained neural
    % network performs.
    genFunction(net,'myNeuralNetworkFunction');
    y = myNeuralNetworkFunction(x);
end
if (false)
    % Generate a matrix-only MATLAB function for
neural network code
    % generation with MATLAB Coder tools.

genFunction(net,'myNeuralNetworkFunction','MatrixOnly'
,'yes');
    y = myNeuralNetworkFunction(x);
end
if (false)
```

```
    % Generate a Simulink diagram for simulation or
deployment with.
    % Simulink Coder tools.
    gensim(net);
end
MSEtst = tr.tperf(end)

MSEtrn=tr.perf(end)

% % t =
[75.7100000000000;72.0900000000000;72.4000000000000;74
.8700000000000;153.130000000000;65.7500000000000;66.72
00000000000;90.7100000000000;72.7400000000000;75.01;10
8.600000000000;55.7500000000000;75.6000000000000;108.5
00000000000;63.5600000000000;67.3200000000000;112.6300
00000000;57.5000000000000;71.5500000000000;112.8000000
00000;56.9200000000000;66.9200000000000;109.7000000000
00;55.7900000000000;70.2600000000000,;91.900000000000;
54.1100000000000;74.8200000000000;63.4100000000000;60.
3600000000000;55.3500000000000]';
tm=mean(t);
% %
y=[65.4144695853691,80.4436280148613,65.4107436903211,
72.2622123855668,144.320324839435,65.4086219163130,67.
1462401581453,98.5723773294997,65.4090573208705,68.225
5868219461,114.847170852233,65.4084168161396,66.632664
9179008,105.717536383855,65.4080520816094,65.720331119
9461,106.475334546088,65.4081269272825,65.932469297172
7,111.249497276261,65.4080168251884,65.8767015275378,1
05.783061339291,65.4079541280536,72.1079440571441,102.
285003786843,65.4668063176703,78.4710939706941,65.4151
764184771,65.4213235736235,65.4323482352134];
a1=0;
b1=0;
a2=0;
b2=0;
for i=27:31;
    a=((t(i)-y(i))^2);
    b=((t(i)-tm))^2;
    a1=a1+a;
    b1=b1+b;
end
```

```
for i=1:26;
    a2=((t(i)-y(i))^2);
    b2=((t(i)-tm))^2;
    a2=a2+a;
    b2=b2+b;
end

R2test=1-(a1/b1)
R2train=1-(a2/b2)
```

MATLAB CODE FOR ZETA POTENTIAL

```
clc
clear
rng('default') % to initialize weights


x =
[4,2,6;4,2,7;4,5,6;4,5,7;4,5,7.400000000000000;4,10,6;4
,10,7;4,10,7.400000000000000;12,2,6;12,2,7;12,2,7.40000
0000000000;12,5,6;12,5,7;12,5,7.400000000000000;12,10,6;
12,10,7;12,10,7.400000000000000;20,2,6;20,2,7;20,2,7.40
0000000000000;20,5,6;20,5,7;20,5,7.400000000000000;20,10
,6;20,10,7;20,10,7.400000000000000;8,5,6.500000000000000
;8,5,7.200000000000000;4,10,6.300000000000000;15,2,6.400
00000000000;12,5,6.500000000000000]';
t =
[19.800000000000000;7.070000000000000;18.300000000000000;6.
790000000000000;3.410000000000000;15.500000000000000;5.060
00000000000000;3.160000000000000;17.700000000000000;5.960000
00000000000;3.830000000000000;13.200000000000000;4.750000000
00000;2.610000000000000;9.570000000000000;3.650000000000000
00;2.470000000000000;11.500000000000000;4.990000000000000;
3.150000000000000;9.440000000000000;4.180000000000000;2.2
900000000000000;3.280000000000000;2.360000000000000;2.2300
0000000000000;7.670000000000000;5.080000000000000;9.5000000
0000000;8.680000000000000;6.870000000000000]';


trainFcn = 'traingda';


hiddenLayerSize =4;
```

```
net = fitnet(hiddenLayerSize,trainFcn);


net.input.processFcns =
{'removeconstantrows','mapminmax'};
net.output.processFcns =
{'removeconstantrows','mapminmax'};


net.divideFcn = 'divideind';
net.divideMode = 'sample';
net.divideParam.trainInd = 1:26;
net.divideParam.testInd = 27:31;

net.performFcn = 'mse';


net.plotFcns =
{'plotperform','plottrainstate','ploterrhist', ...
    'plotregression', 'plotfit'};


[net,tr] = train(net,x,t);

% Test the Network
y = net(x);
e = gsubtract(t,y);
performance = perform(net,t,y)

% Recalculate Training, Validation and Test
Performance
trainTargets = t .* tr.trainMask{1};
valTargets = t .* tr.valMask{1};
testTargets = t .* tr.testMask{1};
trainPerformance = perform(net,trainTargets,y)
valPerformance = perform(net,valTargets,y)
testPerformance = perform(net,testTargets,y)


if (false)
    % Generate MATLAB function for neural network for
application
    % deployment in MATLAB scripts or with MATLAB
Compiler and Builder
```

```
% tools, or simply to examine the calculations your
trained neural
    % network performs.
    genFunction(net,'myNeuralNetworkFunction');
    y = myNeuralNetworkFunction(x);
end
if (false)
    % Generate a matrix-only MATLAB function for
neural network code
    % generation with MATLAB Coder tools.

genFunction(net,'myNeuralNetworkFunction','MatrixOnly'
,'yes');
    y = myNeuralNetworkFunction(x);
end
if (false)
    % Generate a Simulink diagram for simulation or
deployment with.
    % Simulink Coder tools.
    gensim(net);
end
MSEtst = tr.tperf(end)
```

APPENDIX C – ARTIFICIAL NEURAL NETWORK OPTIMIZATION

Table C1. MSE and R-squared of test values for different backpropagation methods and number of hidden layers. Selected artificial neural networks were highlighted with yellow.

		Size		Zeta Potential	
	Number of Layers	MSE	R-squared	MSE	R-Squared
Levenberg–Marquardt	1	67.7103	0.7869	1.4146	0.4207
	2	165.8454	0.4781	2.4310	0.0045
	3	118.26800	0.6278	189.8441	-76.7435
	4	315.1706	0.0082	6.0040	-1.4587
	5	191.3920	0.3977	14.8534	-5.0827
Bayesian Regularization	1	87.1963	0.7256	1.5300	0.3734
	2	85.7353	0.7302	1.2314	0.4957
	3	94.7072	0.7020	5.8444	-1.3934
	4	156.6771	0.5070	5.2728	-1.1593
	5	156.6771	0.5070	5.5617	-1.2777
BFGS quasi-Newton backpropagation	1	73.3523	0.7692	1.4146	0.4207
	2	109.4239	0.6557	13.4744	-4.5179
	3	80.5224	0.7466	7551.9012	-3091.5954
	4	205.6124	0.3530	1.3999	0.4267
	5	283.2841	0.1085	2.2884	0.0629
Conjugate gradient backpropagation with Powell-Beale restarts	1	68.398	0.7848	1.4145	0.4208
	2	108.1286	0.6597	21.0071	-7.6026
	3	178.3078	0.4389	6.6065	-1.7055
	4	120.4419	0.6210	2.1446	0.1218
	5	360.9020	-0.1357	96.8988	-38.6812
Conjugate gradient backpropagation with Fletcher-Reeves updates	1	70.6825	0.7776	1.4141	0.4209
	2	111.2434	0.6499	15.6255	-5.3988
	3	143.4568	0.5486	13.1789	-4.3969
	4	1001.4138	-2.1513	1.2285	0.4969
	5	504.0172	-0.5861	69.5473	-27.4805
Gradient descent with adaptive learning rate	1	70.0324	0.7412	1.1229	0.3992
	2	245.9936	0.3358	0.8013	0.7688
	3	81.4300	0.7438	2.1638	0.1139
	4	216.0139	0.3202	0.2438	0.8987
	5	277.6521	0.1206	22.1147	-8.1408
Gradient descent with momentum and adaptive learning rate	1	69.5176	0.7696	1.4147	0.4207
	2	207.8586	0.3459	4.3325	-0.7742
	3	74.7955	0.7646	5.3098	-1.2959
	4	68.9689	0.7830	0.4812	0.8071
	5	477.7576	-0.5287	1.7578	0.2801
One-step secant backpropagation	1	68.7830	0.7835	1.4146	0.4207
	2	238.2613	0.2502	4.3689	-0.7891
	3	187.2926	0.4106	13.4514	-4.5085
	4	176.5785	0.4443	0.8160	0.6659
	5	1519.3452	-3.7812	12.2137	-4.0016
Scaled conjugate gradient backpropagation	1	68.6609	0.7839	1.4146	0.4207
	2	108.3061	0.6592	13.4745	-4.518
	3	180.9060	0.4307	13.2931	-4.4437
	4	284.6282	0.1043	0.8994	0.6317
	5	380.7509	-0.1982	23.8565	-8.7695